Measurement and Monte Carlo simulation of electron fields for modulated electron radiation therapy

by

Samantha A.M. Lloyd
B.Sc., Thompson Rivers University, 2009
M.Sc., University of Victoria, 2011

A Dissertation Submitted in Partial Fulfillment of the
Requirements for the Degree of

DOCTOR OF PHILOSOPHY

in the Department of Physics and Astronomy

Measurement and Monte Carlo simulation of electron fields for modulated electron radiation therapy

by

Samantha A.M. Lloyd
B.Sc., Thompson Rivers University, 2009
M.Sc., University of Victoria, 2011

Supervisory Committee

Dr. Isabelle M. Gagne, Co-supervisor
(Department of Physics and Astronomy)

Dr. Andrew Jirasek, Co-supervisor
(Department of Physics and Astronomy)

Dr. Sergei Zavgorodni, Member
(Department of Physics and Astronomy)

Dr. Poman So, Outside Member
(Department of Electrical and Computer Engineering)

Supervisory Committee

Dr. Isabelle M. Gagne, Co-supervisor
(Department of Physics and Astronomy)

Dr. Andrew Jirasek, Co-supervisor
(Department of Physics and Astronomy)

Dr. Sergei Zavgorodni, Member
(Department of Physics and Astronomy)

Dr. Poman So, Outside Member
(Department of Electrical and Computer Engineering)

ABSTRACT

This work establishes a framework for Monte Carlo simulations of complex, modulated electron fields produced by Varian's TrueBeam medical linear accelerator for investigations into modulated electron radiation therapy (MERT) and combined modulated photon and electron radiation therapy (MPERT). Both MERT and MPERT have shown potential for reduced low dose to normal tissue without compromising target coverage in the external beam radiation therapy of some breast, chest wall, head and neck, and scalp cancers. This reduction in low dose could translate into the reduction of immediate radiation side effects as well as long term morbidities and incidence of secondary cancers.

Monte Carlo dose calculations are widely accepted as the gold standard for complex radiation therapy dose modelling, and are used almost exclusively for modelling

the complex electron fields involved in MERT and MPERT. The introduction of Varian's newest linear accelerator, the TrueBeam, necessitated the development of new Monte Carlo models in order to further research into the potential role of MERT and MPERT in radiation therapy. This was complicated by the fact that the field-independent internal schematics of TrueBeam were kept proprietary, unlike in previous generations of Varian accelerators.

Two approaches are presented for performing Monte Carlo simulations of complex electron fields produced by TrueBeam. In the first approach, the dosimetric characteristics of electron fields produced by the TrueBeam were first compared with those produced by an older Varian accelerator, the Clinac 21EX. Differences in depth and profile characteristics of fields produced by the TrueBeam and those produced by the Clianc 21EX were found to be within 3%/3 mm. Given this information, complete accelerator models of the Clinac 21EX, based on its known internal geometry, were then successfully modified in order to simulate 12 and 20 MeV electron fields produced by the TrueBeam to within 2%/2 mm of measured depth and profile curves and to within 3.7% of measured relative output. While the 6 MeV TrueBeam model agreed with measured depth and profile data to within 3%/3 mm, the modified Clinac 21EX model was unable to reproduce trends in relative output as a function of field size with acceptable accuracy.

The second approach to modelling TrueBeam electron fields used phase-space source files provided by Varian that were scored below the field-independent portions of the accelerator head geometry. These phase-spaces were first validated for use in MERT and MPERT applications, in which simulations using the phase-space source files were shown to model depth dose curves that agreed with measurement within 2%/2 mm and profile curves that agreed with measurement within 3%/3 mm. Simulated changes in output as a function of field size fell within 2.7%, for the most part.

In order to inform the positioning of jaws in MLC-shaped electron field delivery, the change in output as a function of jaw position for fixed MLC-apertures was investigated using the phase-space source files. In order to achieve maximum output and minimize treatment time, a jaw setting between 5 and 10 cm beyond the MLC-field setting is recommended at 6 MeV, while 5 cm or closer is recommended for 12 and 20 MeV with the caveat that output is most sensitive to jaw position when the jaws are very close to the MLC-field periphery. Additionally, output was found to be highly sensitive to jaw model. A change in divergence of the jaw faces from a point on the source plane to a 3×3 mm^2 square in the source plane changed the shape of the output curve dramatically.

Finally, electron backscatter from the jaws into the monitor ionization chamber of the TrueBeam was measured and simulated to enable accurate absolute dose calculations. Two approaches were presented for measuring backscatter into the monitor ionization chamber without specialized electronics by turning off the dose and pulse forming network servos. Next, a technique was applied for simulating backscatter factors for the TrueBeam phase-space source models without the exact specifications of the monitor ionization chamber. By using measured backscatter factors, the forward dose component in a virtual chamber was determined and then used to calculate backscatter factors for arbitrary fields to within 0.21%. Backscatter from the jaws was found to contribute up to 2.6% of the overall monitor chamber signal. The measurement techniques employed were not sensitive enough to quantify backscatter from the MLC, however, Monte Carlo simulations predicted this contribution to be 0.3%, at most, verifying that this component can be neglected.

Contents

List of Tables

List of Figures

LIST OF ACRONYMS

AAPM American Association of Physicists in Medicine

CPU central processing unit

CSDA continuous slowing down approximation

CT computed tomography

DICOM digital imaging and communications in medicine

DNA deoxyribonucleic acid

EGS electron gamma shower

eMC electron Monte Carlo

FWHM full width at half maximum

IAEA International Atomic Energy Agency

IMRT intensity modulated radiation therapy

Linac linear accelerator

MERT modulated electron radiation therapy

MPERT mixed modulated photon and electron radiation therapy

MLC multileaf collimator

MRI magnetic resonance imaging

MU monitor unit

NIST National Institute of Standards and Technology

OD optical density

ODI optical distance indicator

PC personal computer

PET positron emission tomography

PFN pulse forming network

PRESTA parameter reduced electron step algorithm

PDD percent depth dose

RAM random-access memory

SLAC Stanford Linear Accelerator Center

SSD source to surface distance

TB TrueBeam

VIMC Vancouver Island Monte Carlo

VMAT volumetric modulated arc therapy

ACKNOWLEDGEMENTS

It would be impossible to acknowledge, individually, each colleague, mentor, friend and family member who has enabled the completion of this dissertation. To each of you, I can never adequately thank you for your support and patience.

To my supervisor, Isabelle Gagne, thank you for your wisdom, tenacity and perseverance. Your supervision and guidance were extraordinary, despite a busy clinical schedule and many, many detours in our road map. If there is a story told in this work, it is your doing.

To my supervisory committee, Andrew Jirasek, Sergei Zavgorodni and Poman So, thank you for keeping me focused on the big picture, guiding me through the tall grass and reading every iteration of the articles and dissertation that landed on your desk.

To Magdalena Bazalova-Carter, who might as well have been a member of the supervisory committee, thank you for reminding me of the collaborative nature of science, and for your eagerness to assist with any problem, big or small, even if it was just initializing imagers late at night.

I would have been stuck in the mud without the Monte Carlo expertise of Karl Bush, Reid Townson, Anna Rodrigues and Daren Sawkey. Without Mark Baker, there wouldn't have been a project.

To each of the physicists at the BC Cancer Agency, thank you for the quick chats, the GSM questions that stumped me, and the environment of excellence and fun that you establish in the physics department. To each of the dosimetrists, therapists and technicians, thank you for keeping my work grounded in reality. To each of the students and graduates in the Department of Physics and Astronomy at the University of Victoria, thank you for inspiring me in the moments I felt defeated.

To my parents, sister, and extended family, who have never stopped supporting me and have never questioned my academic capacity, especially when I did, thank you for putting up with my exhaustion - I promise not to be too obnoxious for too long. To my friends, I promise to always be exactly as obnoxious as you'll let me.

To Stephen Gray, Evan Maynard, Samantha Harder and Beth Chisholm, you know what you did, and I will be forever grateful.

To the trees and animals in the wild, thanks for waiting. It's time for some adventures.

Chapter 1

Introduction

In Canada, 45% of men and 42% of women will develop cancer at some point in their lifetime [81] and approximately half of these individuals will receive radiation therapy as part of their curative or palliative treatment [54]. The suite of radiation delivery mechanisms is broad, ranging from external fields of radiation, to radioisotopes placed within the affected tissue, with countless techniques for planning, targeting and treatment verification. There are some dosimetric and biological advantages to performing external beam therapies with heavy particles such as protons, neutrons or other exotic ions [54], but due to their relatively low cost and proven efficacy, photon and electron fields are the most widely used external beam treatment modalities, making medical electron accelerators the workhorse of most radiation oncology departments [104]. Medical electron linear accelerators use accelerated electrons to produce therapeutic fields of photons or scattered electrons and, historically, photons have been the modality of choice for conformally irradiating targets at depth while electrons have been reserved for superficial treatments using simple delivery techniques [61].

With advances in the planning and delivery of highly complex and modulated photon fields, the use of complex electron fields and the integration of photon and electron fields in a single treatment has garnered increased research attention. While this was once inhibited by the challenges of accurate and expedient electron field simulations, advances in computational hardware and simulation techniques have made these simulations achievable at clinically relevant timescales. This thesis reviews the motivation for and implementation of the Monte Carlo accelerator models required to perform accurate simulations of complex electron radiation therapy fields.

1.1 Radiation therapy

Ionizing radiation has been utilized therapeutically since the announcement of its discovery in 1896 [67]. In the 120 years that have followed, physicians, physicists, biologist and chemists have characterized the harmful and therapeutic properties of radiation, including the transfer of energy, chemical changes and biological pathways that lead to cell death or mutation.

As ionizing radiation passes through matter it interacts with the orbital electrons and nuclei of atoms in its path, producing ions and free electrons that cause subsequent cascading ionizations as they slow and deposit their energy. If these ionizations occur in close proximity to the nucleus of a cell, they may cause chemical reactions that ultimately result in DNA strand breaks. If these breaks can be repaired by the cell's repair mechanisms, the cell may go on to divide, however, if the cell cannot repair the DNA break, or if the repair results in an incorrect DNA sequence, the cell may be unable to divide successfully or at all, resulting in cell death or senescence [54].

The aim of radiation therapy is to selectively kill cancer cells through radiation damage, while sparing as much of a patient's healthy, normal tissue as possible, and also minimizing the risk of radiation induced secondary cancers in the patient's lifetime. To that end, the techniques used to deliver prescribed radiation doses while shielding and sparing normal tissue are ever advancing; developments in image-guidance, motion management and computer aided planning mean that contemporary radiation therapy is more targeted, conformal and accurately delivered than ever before.

External beam photon therapy is well utilized because of its ease of production, manipulation and simulation, in addition to its low cost relative to other modalities. Specifically, photon beams between 6 and 25 MV are used extensively to treat deep-seated tumours. In contrast, clinical electron fields are less penetrating than photons and are used most often for shallow diseases of the skin, post-mastectomy chest-wall, lymphatics and in head and neck cancers [61]. The advantage of electron fields lies in the finite range of charged particles in matter, beyond which, normal tissue such as the heart or lungs may be spared.

Despite the increasing sophistication and degrees of freedom allowed by contemporary medical linear accelerators, and the high quality of CT (computed tomography), MRI (magnetic resonance imaging) and PET (positron emission tomography) for treatment planning imaging, advanced applications for electrons, such as arcs [34] and multi-field conformal treatments [87], have seen limited implementation. Until recently, the greatest impeding factor had been that most commercially available treatment planning software packages were without the tools to accurately model electron therapy [46]. As a result, the vast majority of electron treatments are delivered as single, static, unmodulated fields [61] collimated with standard or custom shaped cutouts or shields made of Cerrobend or lead placed on or near the skin [46].

With improving access to more accurate planning tools, however, utilization of more complex modes of electron field delivery is an active area of research [44, 89]. Analogous to complex photon techniques such as intensity modulated radiation therapy (IMRT) [15] and volumetric modulated arc therapy (VMAT) [83], modulated electron radiation therapy (MERT) utilizes irregularly shaped and intensity modulated fields of electrons to achieve highly conformal dose deposition around a target volume with rapid dose fall off outside that volume. Modulated photon and electron radiation therapy (MPERT) utilizes shape and intensity modulated fields of both modalities to achieve the same end. The strategies employed in MERT and MPERT are described in greater detail below.

1.1.1 Modulated electron radiation therapy

Modulated electron radiation therapy and modulated photon and electron radiation therapy have been shown, through phantom [38] and retrospective planning studies, to reduce dose delivered to healthy tissue and/or to improve target dose uniformity for some breast [4, 44, 74, 113], post-mastectomy chest wall [37, 96], head and neck [43, 95] and scalp treatments [52] compared to conventional electron therapies, and photon-IMRT.

Alexander et al. [4] investigated the role of MERT for boost of post lumpectomy tumour bed in breast and found that MERT outperformed VMAT and conventional electron fields for target coverage and integral dose to normal tissue, while achieving equivalent lung sparing compared to VMAT. Henzen et al. [43], Xiong et al. [113] and Gauer et al [37] investigated MERT for whole breast and chest wall treatments, and found MERT to be superior to conventional photon tangents in terms of reduced dose to lung and normal tissue. Xiong et al. showed MERT to achieve better dose homogeneity while Henzen et al. found MERT homogeneity to be worse. Henzen et al. also investigated MERT for head and neck sites, as did Salguero et al. [95]. Both studies found MERT to achieve better dose-sparing than IMRT.

These studies presented varied approaches to MERT planning and delivery. Ge and Faddegon [38] and Xiong et al. [113] each forward planned an electron field and optimized photon fields based on the fixed electron dose contribution while, additionally, Xiong et al. allowed for adjustable weighting of the electron contribution as part of the photon optimization. Gauer et al. [37] and Salguero et al. [96] optimized multiple fields of static electron fields shaped with an add-on electron MLC and a photon MLC, respectively. Alexander et al. [4] used a few-leaf add-on electron collimator at a single angle while Henzen et al. [44] used a photon MLC at multiple angles to generate plans that achieved intensity modulation by delivering multiple apertures at each gantry angle.

Despite variations in the number of apertures, configuration of fields and type of collimation used in these techniques, Monte Carlo calculations were used to simulate the resulting dose distributions in every case [56, 78, 100]. Accurate treatment planning and simulation tools are essential for the development of any new treatment technique, and the increasing accessibility of fast Monte Carlo dose calculation systems has made these and further studies possible. As well, although MERT and MPERT have seen limited clinical application, in-house planning and delivery systems have been designed and validated in efforts toward broader clinical utility [3, 29].

1.2 Radiation therapy treatment planning

Treatment planning in radiation therapy encompasses the positioning and immobilization of the patient, localization of the target volume in relation to the patient's geometry, selection and arrangement of fields and devices for treatment, simulation of the resulting dose deposition and verification of the treatment plan [32]. The accuracy and reliability of a treatment planning process directly impacts the efficacy of the delivered cancer therapy.

In a typical clinic workflow, prior to beginning treatment, the patient has a planning appointment during which he or she is positioned in the orientation he or she will assume during treatment, and a planning CT image set is acquired. CT pixel data is stored in Hounsfield units which correspond to the mass attenuation in that pixel relative to water [17].

The CT image set is imported into treatment planning software where Hounsfield Units are mapped to mass density. Within the treatment planning software, the target volume and organs at risk can be identified and contoured so that fields of appropriate energy, shape and orientation can be selected and configured to maximize target coverage while minimizing dose to normal tissue, in particular, the organs at risk.

A screenshot of the Varian Eclipse (Varian Medical Systems, Palo Alto, CA) treatment planning environment is shown in Figure 1.1 for a breast treatment. Structures that delineate the target volume and organs at risk are overlaid on the CT data in axial, coronal and sagittal views, as is the dose resulting from the two tangential fields illustrated on either side of the breast. Dose is displayed as lines of equivalent dose, or isodose lines, which represent some proportion of the prescribed dose.

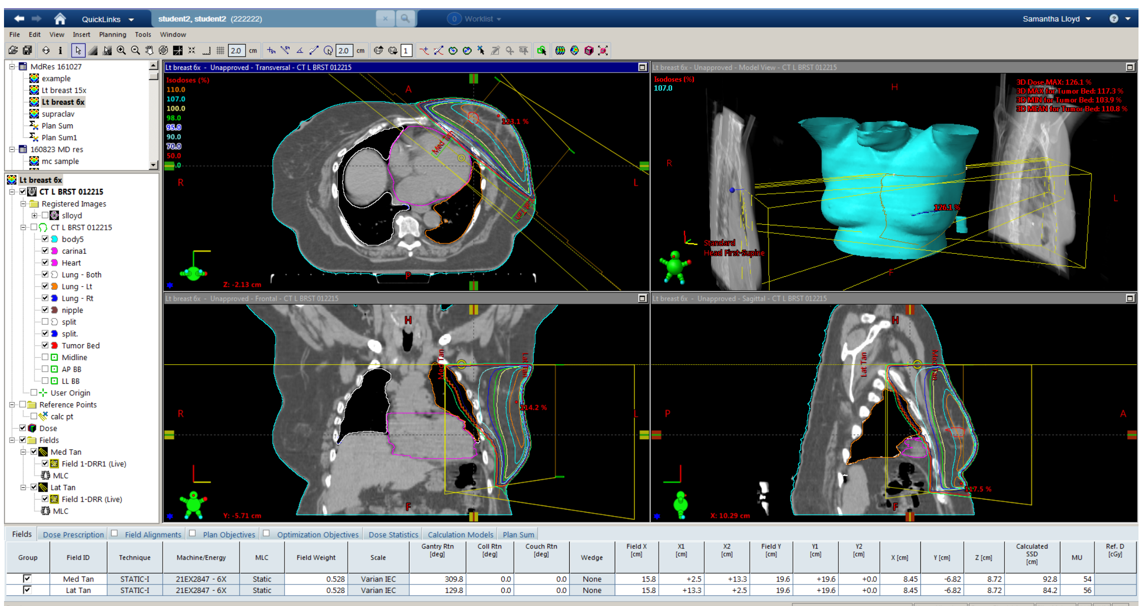

Figure 1.1: Screenshot of Varian's Eclipse treatment planning software. Anatomical contours, external treatment fields and resulting dose are superimposed on the planning CT image set.

Part of the field selection and arrangement process involves evaluating the dose distribution that would result from some interim configuration of fields. This is accomplished using a dose calculation algorithm. Commercial treatment planning systems employ a variety of dose calculation strategies, including pencil beam convolution, convolution/superposition, and Monte Carlo. While analytic approaches can be used to model photon treatments with sufficient accuracy [16, 35], Monte Carlo techniques are largely employed for the simulation of electrons. Varian's Eclipse treatment planning software uses electron Monte Carlo (eMC) [114] based on the Macro

Monte Carlo code [78] while VMC++ [57] is implemented in the Oncentra Masterplan treatment planning software (Nucletron B.V., Veenendaal, The Netherlands) [97]. Phillip's Pinnacle treatment planning software (Philips Radiation Oncology Systems, Madison, WI) uses an electron Monte Carlo algorithm [33] based on the Dose Planning Method (DPM) Monte Carlo code [100] in addition to a three-dimensional pencil beam algorithm [101].

An essential aspect of every dose calculation process is translating between dose deposited in tissue, and Monitor Units (MU) delivered by the linear accelerator. Monitor Units are a measure of energy fluence through the monitor ionization chamber within the linear accelerator and for a given machine, 100 MU corresponds to a calibration dose defined at some location and depth in water. By defining the relationship between MU and absorbed dose under some set of reference conditions, a treatment planning system can assign MU for a given field to achieve some target dose. The calculation of MU must account for all factors that would impact the relationship between MU and absorbed dose, including, but not limited to, source to surface distance, beam modifiers and collimator scatter [40].

1.2.1 Monte Carlo for treatment simulation

In radiation physics, Monte Carlo methods use random number generators and the probability density functions that describe physical processes to explicitly model the individual events and interactions that take place during particle transport and energy transfer. While some analytic solutions have been presented for the simulation of complex electron treatments [21], Monte Carlo solutions are attractive due to their improved accuracy [117] as well as their increasing accessibility [46] and improving computing speeds [105].

A number of commercial Monte Carlo packages are available for radiation therapy particle transport. Macro Monte Carlo [78], DPM [100] and VMC++ [57], were mentioned in the preceding text. General particle physics Monte Carlo packages GEANT4 [1] and PENELOPE [11] have also been used for radiation therapy simulations [30]. The EGSnrc Monte Carlo particle transport code [56] is a Canadian National Research Council (NRC) adaptation of the EGS (electron gamma shower) particle transport package originally developed at SLAC for general particle physics simulations [31]. The EGSnrc user packages, BEAMnrc and DOXYZnrc, are designed to model the radiation sources and geometries encountered in radiation oncology physics, and are freely available from the NRC website for non-commercial use. EGSnrc has been extensively benchmarked [5, 6, 30, 58] and is used widely throughout the medical physics community [46].

BEAMnrc and DOSXYZnrc are used throughout this work for Monte Carlo simulations of electron fields produced by Varian linear accelerators. The software was run on its own, as well as through the web-based user interface developed at the BC Cancer Agency's Vancouver Island Centre: Vancouver Island Monte Carlo (VIMC) [115].

1.3 Objective/Scope

The objective of the work presented in this dissertation is to establish an accurate Monte Carlo dose calculation framework for the simulation of electron fields produced by Varian's newest linear accelerator, the TrueBeam. Six TrueBeam accelerators were installed at the BC Cancer Agency's Vancouver Island Centre at the beginning of this project, and in contrast to previous generations of Varian linear accelerators, the internal specifications required for accurate Monte Carlo modelling of the TrueBeam were kept proprietary. Phase-space source files, which can be used as the input for Monte Carlo calculations in lieu of modelling a full accelerator, were not published until well into the progression of this research. As a result, the objectives of this work are two fold:

1. To evaluate the feasibility of modifying a complete Monte Carlo model of an older Varian linear accelerator to simulate the dosimetric output of the TrueBeam, and then to evaluate the performance of these modified models against measurement of electron field configurations encountered in MERT.

2. To benchmark the TrueBeam electron phase-space source files, generated by Varian, against measurement of electron field configurations involved in MERT, and to implement the necessary backscatter corrections required to enable accurate absolute dose calculations of TrueBeam electron fields.

In Chapter 4, measured characteristics of electron fields generated by the TrueBeam linear accelerator are compared to an older Varian accelerator, the Clinac 21EX. Data is compared for conventional fields delivered at 100 cm source to surface distance (SSD) with standard electron applicators and cut-outs, as well as for MERT fields shaped using the multi-leaf collimator (MLC) and delivered at 70 cm SSD. In Chapter 5, an existing Monte Carlo model of the Clinac 21EX used to simulate photon fields [16, 115] is used to simulate electron fields based on the known schematics of the accelerator. (The photon models have been benchmarked against measurement and are used clinically to perform patient-specific dose verification simulations.) This is followed by the modification of these models to simulate fields that are dosimetrically equivalent to those produced by the TrueBeam, and benchmarking of both machine models against measurement. Chapters 4 and 5 address the first objective.

In Chapter 6, the phase-space source files provided by Varian for electron field simulations are benchmarked against measurement for MERT configurations involving MLC field shaping and short, 70 cm SSD delivery. In Chapter 7 backscatter into the monitor ionization chamber of the linear accelerator as a function of field size is investigated, along with its impact on dose output. Two techniques for measuring electron backscatter into the monitor chamber without specialized electronics are described. A method for correcting Monte Carlo simulations for this effect without explicitly simulating the forward dose through the monitor chamber is described, establishing the necessary framework for accurate calculations of absolute dose. Chapters 6 and 7 address the second objective.

Chapter 2 establishes the necessary theoretical background for this work while Chapter 3 describes the general methodologies employed. Chapter 8 will summarize the results and impact of this dissertation. Part of Chapter 5 has been published on arXive [71], while Chapters 4, 6 and 7 have been published as articles in refereed journals [69, 70, 72].

Chapter 2

Background

This chapter provides the background theory required to describe and discuss the methods and results presented in Chapters 3 through 7. The interactions that lead to energy transfer and deposition due to ionizing radiation are presented first, followed by a description of the radiation dosimetry tools used to perform measurements in this work. The general design of a linear accelerator is described, followed by a discussion of the specific features of Varian's Clinac 21EX and TrueBeam models. This chapter concludes with a description of Monte Carlo methods for particle transport in radiation oncology physics, and specifically, the EGSnrc transport code and user packages, BEAMnrc and DOSXYZnrc.

2.1 Radiation therapy physics

The deposition of dose due to ionizing radiation is the result of innumerable photon and electron interactions within an irradiated material. Monte Carlo methods model each of these interactions explicitly or in a condensed form to determine the ultimate deposition of energy throughout. In the energy range employed in linear accelerator based radiation oncology physics, photons interact with bound electrons to produce other photons or free electrons (photoelectric and Compton) or with the nucleus to produce electron-positron pairs. Electrons may interact with bound electrons to produce more free electrons, or they may interact with the nucleus to create bremsstrahlung photons. Each of these interactions is described in detail below.

2.1.1 Photon interactions

Rayleigh (Coherent) scattering

Rayleigh scattering, or coherent scattering, occurs when an incident photon causes all of the electrons in an atom to vibrate momentarily, and then scatter the photon at some angle with the same incident wavelength [53]. The process is modelled as a redirection of the photon without any energy loss. The cross sections for Rayleigh scattering drop off quickly beyond 100 keV in low Z materials [53]. As will be mentioned in Chapter 3, Rayleigh scattering is not explicitly modelled in the simulations performed in this work.

Photoelectric effect

The photoelectric effect describes an interaction between an incident photon and a bound, inner shell electron during which all of the photon's energy is transferred to the electron and the electron is ejected from the atom. The energy of the resulting free electron is the energy of the incident photon, $h\nu$, less the binding energy of the shell from which the electron has been ejected. The vacancy in the inner shell will be filled by an outer shell electron which gives off a characteristic photon of energy determined by the difference in binding energies between the inner and outer atomic shells.

Ejected electrons are emitted sideways, but become more forward directed as energy increases, although they may never be emitted at 0° [10]. While the energy transferred to the atom in a photoelectric interaction is negligible, the atom does take on a non-negligible momentum following the interaction [10, 99].

Photoelectric effect is most probable when $h\nu$ is just greater than the binding energy of a particular atomic shell, and its cross section varies approximately as $1/(h\nu)^3$ [53]. Provided that the incident photon has energy greater than the binding energy of the K-shell, about 80% of all photoelectric interactions occur in the K-shell. The photoelectric effect is most prominent in photon energy ranges used for diagnostic imaging, generally below 1 MeV. The photoelectric cross section is greater for higher Z materials, varying approximately as Z^3 [61]. Photoelectric attenuation cross section curves for water and tungsten are shown in Figure 2.1. Data comes from the NIST XCOM Photon Cross Sections Database [12], based on data from Scofield [98].

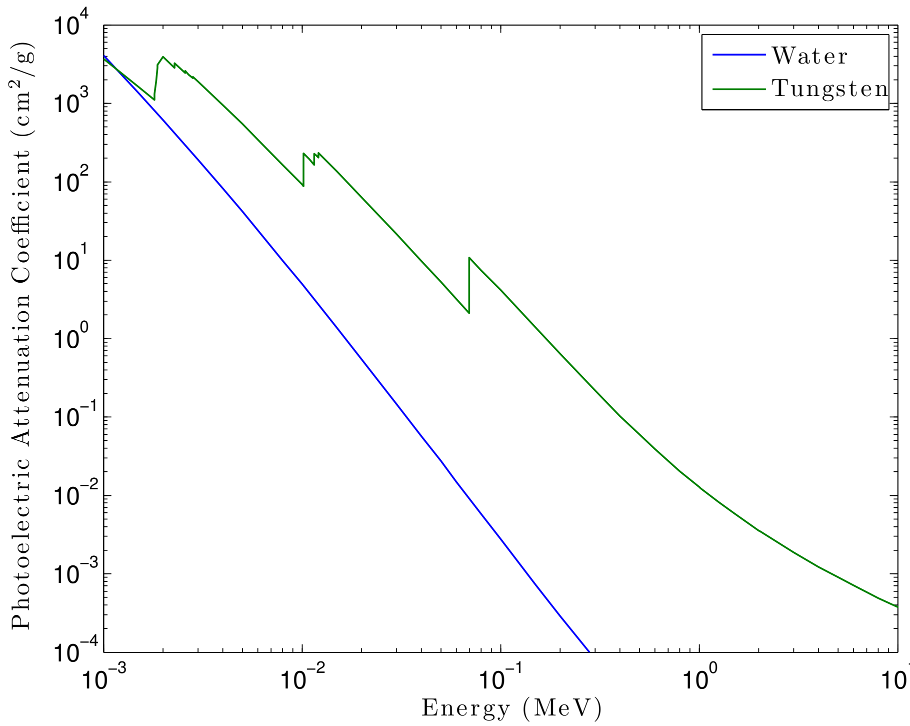

Figure 2.1: Photoelectric attenuation cross sections for water and tungsten. Data is from the NIST XCOM Photon Cross Sections Database [12].

Compton scattering

Compton scattering occurs when an incident electron interacts with an outer shell atomic electron, often approximated as a free electron as its binding energy is negligibly low compared to the energy of the incident photon [61]. Part of the photon's energy, $h\nu$, is transferred to the electron which recoils at some angle, θ, while the photon continues on with the remainder of its initial energy, $h\nu'$, at some scattered angle, ϕ. By conservation of energy and momentum, the energy of the free electron, E, can be related to its recoil angle as follows [10]:

$$E = h\nu - h\nu', \tag{2.1}$$

where

$$h\nu' = \frac{h\nu}{1 + (h\nu/m_0c^2)(1 - \cos\phi)}, \tag{2.2}$$

$$\cot\theta = \left(1 + \frac{h\nu}{m_0c^2}\right)\tan\left(\frac{\phi}{2}\right), \tag{2.3}$$

and $m_0c^2 = 0.511$ MeV. The electron's kinetic energy is zero when it is scattered at right angles to the photon's initial trajectory, but maximum when the electron has the photon's initial trajectory following the collision [53].

The differential cross-section for Compton scattering is given by the Klein-Nishina equation, the general form of which is

$$\frac{d_e\sigma}{d\Omega} = \frac{r_0^2}{2}\frac{(1+\cos^2\theta)}{[1+\alpha(1-\cos)]^2}\left\{1 + \frac{\alpha^2(1-\cos\theta)^2}{[1+\alpha(1-\cos\theta)](1+\cos^2\theta)}\right\} \tag{2.4}$$

where $\alpha = h\nu/m_0c^2$, and $r_0 = 2.818 \times 10^{-13}$ cm is the classical electron radius [99]. Compton interactions are dominant at photon energies between 100 keV and 10 MeV and are nearly independent of atomic number [53], however, the Compton cross-section decreases with increasing energy. Compton scattering attenuation cross section curves for water and tungsten are shown in Figure 2.2. Data comes from the NIST XCOM Photon Cross Sections Database [12], based on data from Hubble [50] which combines Klein-Nishina with additional nonrelativisitc functions.

Pair and triplet production

A photon with energy greater than 1.022 MeV may interact with the Coulomb field of an atomic nucleus to become an electron positron pair [10]. In this interaction, the nucleus recoils with some momentum, but the energy transferred to the atom is so small that it is neglected and the energy of the incident photon less the rest mass of the electron positron pair (1.022 MeV) is divided between the electron and the positron [53], though not necessarily equally. The average energy of the electron and positron, $\bar{E}$, is given by [10]

$$\bar{E} = \frac{h\nu - 1.022\text{MeV}}{2}, \tag{2.5}$$

while the average angle of departure, $\bar{\theta}$, of the electron and positron relative to the photon's initial trajectory is given by [10]

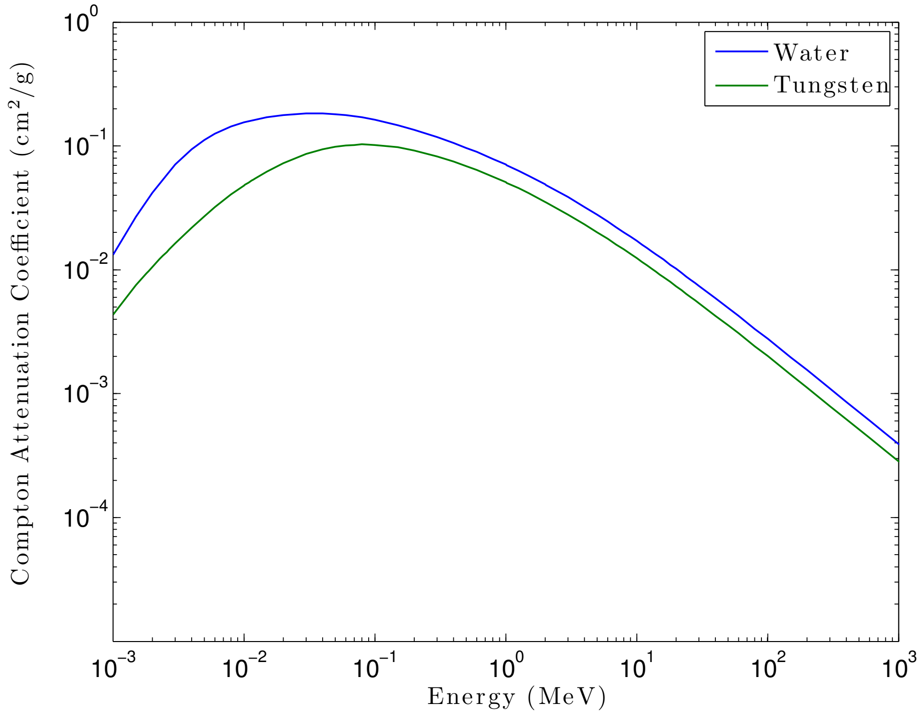

Figure 2.2: Compton scattering attenuation cross sections for water and tungsten. Data is from the NIST XCOM Photon Cross Sections Database [12].

$$\bar{\theta} \cong \frac{m_0 c^2}{\bar{E}}. \tag{2.6}$$

Both charged particles will carry on depositing energy as described in the next section, however, when the positron reaches its rest energy, it will annihilate with a free electron to produce two photons, each with energy 0.511 MeV, emitted at approximately 180° [61]. If the positron has energy greater than 1.022 MeV, the annihilation photons will have some initial momentum and their angular separation will be less than 180°.

If the incident photon has energy greater than 2.044 MeV, it may interact with the Coulomb field of an orbital electron in a process called triplet production, in which the orbital electron is also ejected [99]. Triplet production is less common than pair production.

Pair production cross sections increase rapidly with energy above the 1.022 MeV threshold and it becomes important in radiation therapy for photons above 5 MeV [53]. Pair production increases as Z^2 per atom and as Z per electron [61]. Attenuation cross section curves for pair production, not including triplet production, for water and tungsten are shown in Figure 2.3. Data comes from the NIST XCOM Photon Cross Sections Database [12], based on tables from Leroux and Thinh [68].

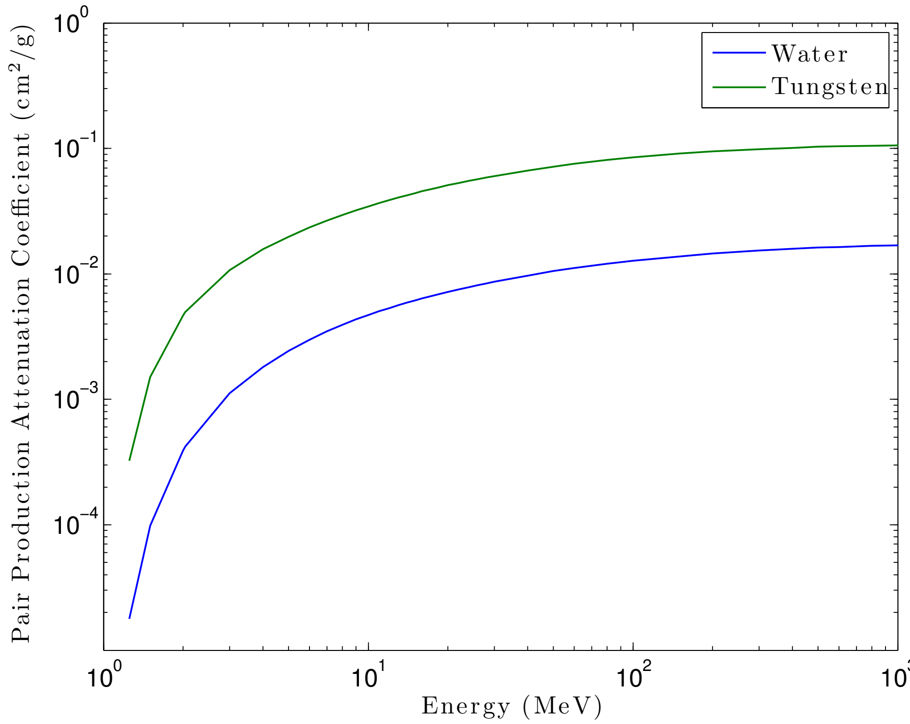

Figure 2.3: Pair production attenuation cross sections for water and tungsten. These cross sections do not account for triplet production. Data is from the NIST XCOM Photon Cross Sections Database [12].

2.1.2 Electron interactions

Electrons traveling through matter undergo many elastic and inelastic interactions with the electric fields of atomic electrons or with atomic nuclei. Due to their charge, unlike photons, electrons are likely to interact with nearly every atom they encounter along their trajectory [10].

In the case of elastic collisions, kinetic energy is not lost, but may be redistributed among the particles that result from the collision and the incident electron may be redirected [61]. Inelastic interactions are either collisional or radiative. When an incident electron interacts with the electric field of atomic electrons, the atom may become ionized. Small transfers of energy to the atom as a whole, on the order of a few eV, are most common and ultimately associated with the ejection of a valence electron. In some cases, however, the incident electron will interact with a single atomic electron, ionizing the atom and transferring some kinetic energy to the ejected electron so that it may carry on and cause additional ionizations. This ejected electron is called a delta ray [10]. By convention, the electron that emerges with the greatest energy is considered to be the incident electron, so the maximum possible energy transfer is half the initial kinetic energy [53]. As in photon interactions, if an inner shell electron is ejected, an outer shell electron may fill the hole by ejection of a characteristic photon.

Radiative collisions occur when the incident electron interacts inelastically with the nucleus of the atom, slowing significantly and giving up kinetic energy in the form of photons called bremsstrahlung, or, breaking radiation [10]. This is the mechanism behind x-ray production for both diagnostic imaging and linear accelerator produced photon fields.

Energy loss by collisional interactions is more likely at low Z, while radiative energy loss is proportional to Z^2 and increases with increasing energy [61].

2.2 Radiation dosimetry

2.2.1 Ionization chambers

Ionization chambers are the most common device used for radiation therapy dosimetry and are preferred for measurements of absolute dose [7]. Very generally, an electric field is applied across a small gas cavity in order to collect the ions produced in the gas when exposed to radiation. The amount of charge collected can be measured by an electrometer and related to the dose deposited in the cavity or in the surrounding material in real time [10].

Two types of ionization chambers were used in this work. The Markus parallel plate ionization chamber and CC13 compact cylindrical ionization chamber are described below.

Markus parallel plate ionization chamber

Parallel plate chambers are constructed of thin foils on either side of an air cavity, and oriented orthogonally to the direction of the beam. These chambers are advantageous because they do not require corrections for the effective point of measurement or for the dose gradient within the active volume as is the case for cylindrical chambers [7].

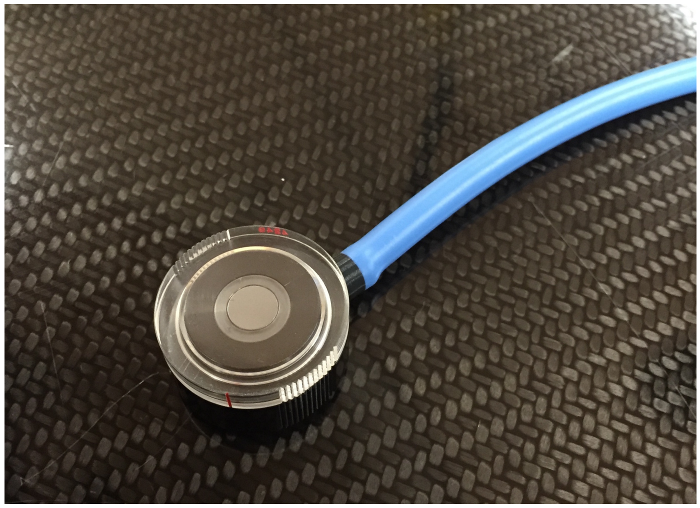

Figure 2.4: PTW Markus parallel plate ionization chamber. Photo credit: Evan Maynard.

The PTW Markus Chamber (PTW-Freiburg, Freiburg, Germany), depicted in Figure 2.4, has a cylindrical, air-filled active region approximately 0.53 cm in diameter and is 0.2 cm thick. The Markus used in this work was cross-calibrated against another Markus chamber which was, in turn, cross-calibrated against the clinic's secondary reference ionization chamber. The secondary reference was calibrated by the National Research Council of Canada standards lab. Although absolute dose was not utilized in this work, this series of cross-calibration allows for conversion from collected charge to absolute dose as outlined in the AAPM Task Group 51 Report (TG-51) [7].

CC13 cylindrical ionization chamber

Cylindrical ionization chambers are the most common design of chamber [10]. A central collecting electrode is surrounded by a cylindrical gas chamber with conducting walls and a bias voltage is applied across the walls and collector. A guard electrode, held at the same potential as the collector, defines the end of the active region where the collecting electrode connects to the cable and reduces leakage signal [61].

The IBA CC13 compact cylindrical ionization chamber (IBA Dosimetry, formerly Scanditronix/Wellhofer, Schwarzenbruck, Germany) has an air-filled active volume of 0.13 cm^3 and an inner radius of 0.3 cm. This chamber is waterproof and was used as the reference detector for diode measurements of profile and depth measurements in water described in Chapter 3.

2.2.2 Scanning electron field diodes

Diode detectors are small and sensitive, and so are well suited for depth and profile scanning dosimetry [62]. The energy required to create an electron-hole pair in silicon is about one tenth of that required to create a unit charge in gas, and so diode detectors are much more sensitive to ionization radiation than ionization chambers [10]. Because the ratio of stopping powers for silicon and water are essentially constant for electron energies between 5 and 25 MeV, diodes can be used for relative dose measurements without corrections for depth. Long-term use can result in dose-rate dependence due to radiation-induced damage to the semiconductor's crystal lattice, however, so the accuracy of diode measurements should be periodically benchmarked against ionization chamber measurements [62].

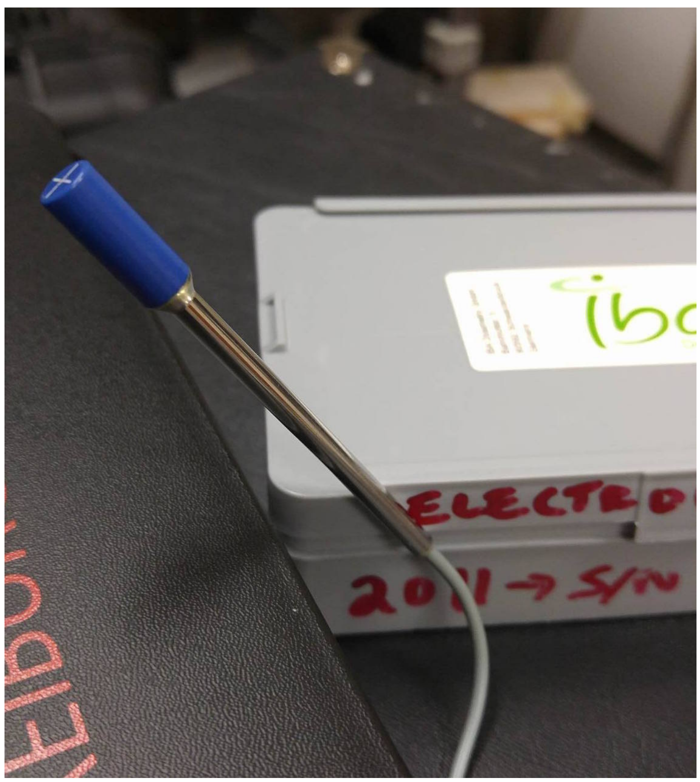

Figure 2.5: IBA EFD^{3G} scanning electron field diode. Photo credit: Stephen Gray.

Two scanning electron field diode detectors were used in this work. The IBA EFD^{3G} scanning electron field diode has an active region measuring 2.0 mm in diameter and 0.060 mm in thickness. This diode was used to acquire relative profile and depth dose curves for applicator and MLC-shaped fields on the TrueBeam, and for MLC-shaped fields on the Clinac 21EX. A Scanditronix diode (Scanditronix/Wellhofer, Schwarzenbruck, Germany) of the same construction [80] was used to acquire relative profile and depth dose curves for applicator-shaped fields on the Clinac 21EX during the machine's commissioning. Scanditronix/Wellhofer became IBA in 2007, and the IBA diode is simply a newer diode of the same model.

2.2.3 Radio-chromic film

Radiochromic film undergoes polymerization when exposed to radiation resulting in permanent colouration. In contrast to radiographic film, the radiochromic process does not require physical, chemical or thermal processing, and some commercial products have been shown, qualitatively, to be insensitive to visible and ultraviolet light [79], making it easier to use in radiation therapy dosimetry. An example of an irradiated film is shown in Figure 2.6

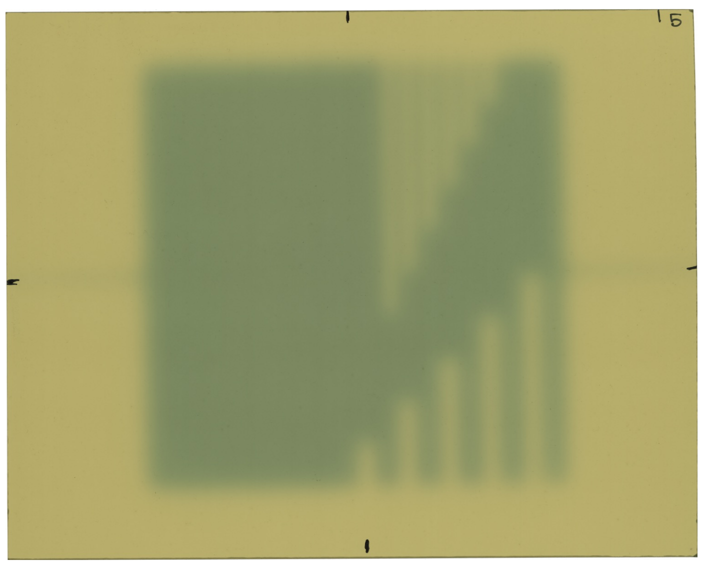

Figure 2.6: Example of an irradiated radio-chromic film. Notches on the film sides indicate the linear accelerator light-field crosshairs.

Gafchromic® EBT2 and EBT3 film (Ashland Inc., Covington, KY) are used in this work to measure electron fields in the plane orthogonal to the beam axis. Both EBT2 and EBT3 film have been found to be suitable for electron dosimetry in studies by Arjomandy et al.[9] and Chan et al.[18], respectively. Reinhardt et al.[86] compared the performance of the films and concluded that EBT2 and EBT3 have similar dosimetric performances with the elimination of side orientation dependencies and the reduction of Newtons ring scanning artifacts through the inclusion of a matte film surface in the case of EBT3 [26].

2.2.4 Solid Water

Solid Water (Gammex Inc., Middleton, WI) is the brand name for an epoxy resin-based water-equivalent plastic designed for radiation therapy dosimetry [24]. Water-equivalent plastics are sometimes preferred over water-based measurements for set-up convenience, however, plastic-to-water attenuation and density corrections must be considered [102]. The aim in the development of Solid Water was to eliminate the need for these corrections, however, characterization of Solid Water for electron fields with energies between 6 MeV and 22 MeV showed that measurements in Solid Water underestimated the peak dose rate by 1.5% at energies less than 10 MeV, and by less than 1% at energies above 10 MeV [103]. Because Solid Water is used for measurements of relative dose changes in this work, plastic-to-water corrections are not applied.

2.3 Medical linear accelerators

For over fifty years, medical linear accelerators have been used in external beam radiation therapy to treat and palliate cancers. Although the design and capability of these machines have advanced considerably, the core components that make up medical linear accelerators have not changed [53]. Electrons produced in an electron gun are accelerated along an accelerating structure to a desired energy, typically between 4 MeV and 25 MeV [55], and through a bending magnet which is used both to redirect the beam along the treatment axis, as well as to narrow the energy range of the electrons. From here, electrons are either incident upon a high-Z material target in order to produce a field of bremsstrahlung photons, or scattered on an arrangement of scattering foils to produce a broadened electron field. After passing through a circular primary collimator, the resulting photon or electron field passes through an ionization chamber used to monitor the machine's output before additional collimators and beam modifiers are used at multiple planes to achieve a beam of the desired shape and intensity. A view of the internal geometry of a Varian Clinac, including each of the components described above, is shown in Figure 2.7.

The exact implementation of beam modifiers is manufacturer dependent, but can generally be categorized into secondary collimators and tertiary devices. Generally,

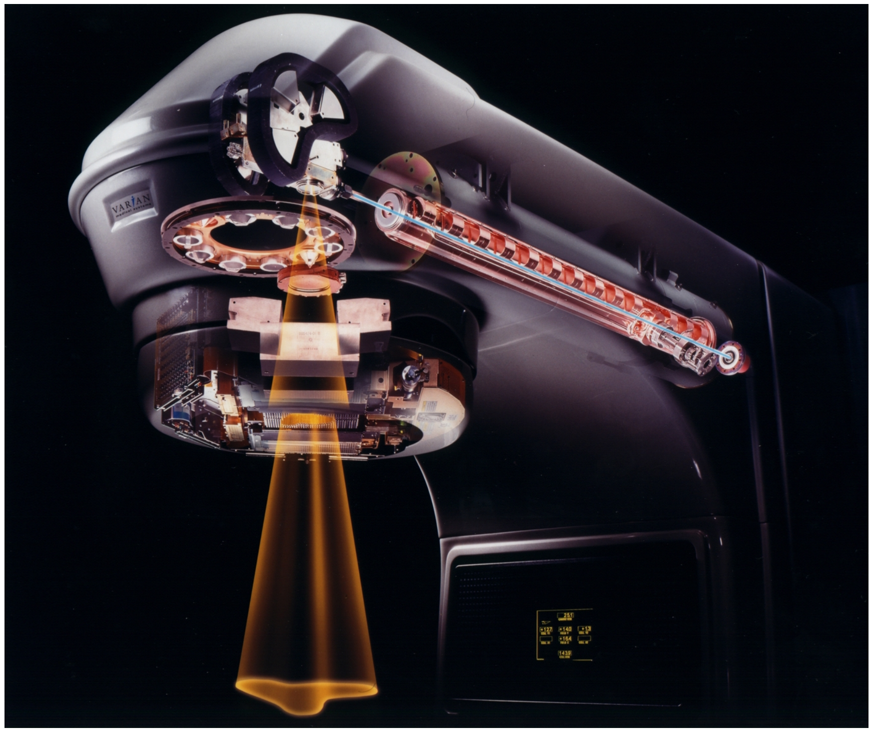

Figure 2.7: Internal view of a Varian Clinac linear accelerator. Image courtesy of Varian Medical Systems Inc.

the secondary collimating jaws are pairs of orthogonally oriented blocks of tungsten that can be used to create arbitrary rectangular fields, while the multi-leaf collimator (MLC), with independently moving, computer controlled leaves of thick, high-density material, can be used to create arbitrary field shapes that conform to a target volume [61]. For Elekta and Siemens accelerators, the MLC replaces one of the jaw pairs, while for Varian machines, which are used in this work, the MLC is a tertiary collimating device included below the secondary collimating jaws [40]. The Varian MLC system will be described in greater detail in Section 2.3.2.

The electron gun, accelerating structure and beam forming devices of a linear accelerator are mounted to a rotating gantry that can deliver radiation fields from any angle in a 360° arc around a fixed location in space called the isocenter. For many accelerators, the isocenter is defined nominally as the point 100 cm from the "source" or photon target. Fields can be delivered from static angles, or while the gantry is rotating. The collimating structures within the accelerator head may also rotate through 360° around the central beam axis to achieve optimal beam conformality around a target.

A number of concepts specific to medical linear accelerator physics are referenced throughout this work, including *beam matching*, *crossline* and *inline* profile directions, *Service mode*, field size and the optical distance indicator (*ODI*). These terms are defined here:

Beam matching is a process by which the measured dosimetric characteristics of two machines are compared and the machines are tuned to match as closely as possible so that a treatment planned for one machine can be delivered on the other without having to re-plan or reevaluate the resulting dose distribution [48].

Crossline and inline: Dose profiles are described as being either in the inline direction, along the same direction as the waveguide, or in the crossline direction, perpendicular to the waveguide. When the collimator is set to 0°, crossline profiles are in the direction of MLC leaf motion and inline profiles are perpendicular to the direction MLC leaf motion.

Service mode: Varian accelerators can be operated in various modes, including Treatment and Service mode. Treatment mode is the only environment that is licensed for treating humans or animals, and an extensive system of interlocks is in place to reduce the risk of mistreatment. For example, in Treatment mode, an electron field will not "beam on" unless there is an electron applicator in place and the photon MLC is retracted. In contrast, in Service mode, the interlocks that would normally prevent bream delivery can be (carefully) overridden and the machine will "beam on." Most of the measured data presented in this work were acquired while running the Clinac 21EX or TrueBeam in Service mode.

Field size: Jaw and MLC positions are defined by the shape of the field they define at isocenter, 100 cm from the photon target. When the field *size*, *aperture* or *setting* is defined as $A \times B$ cm^2, this refers to the X-jaws positioned symmetrically on either side of the central axis, projecting to an A cm field width in the crossline direction, and the Y-jaws positioned symmetrically on either side of the central axis, projecting to a B cm field width in the inline direction.

Optical Distance Indicator (ODI): The linear accelerator head projects a light field along the beam axis that is collimated by the jaws and MLC to assist with patient or phantom setup. The field light has crosshairs that represent the radiation field central axis, and an optical distance indicator (ODI) can be projected in conjunction with the light field and crosshair to determine the SSD. An example of this is shown in Figure 2.8. Alternatively, a physical pointer system can be mounted to the accelerator head to determine the SSD. While the pointer system is generally considered to be more accurate, the ODI system can be turned on and off more conveniently than the front pointers can be mounted.

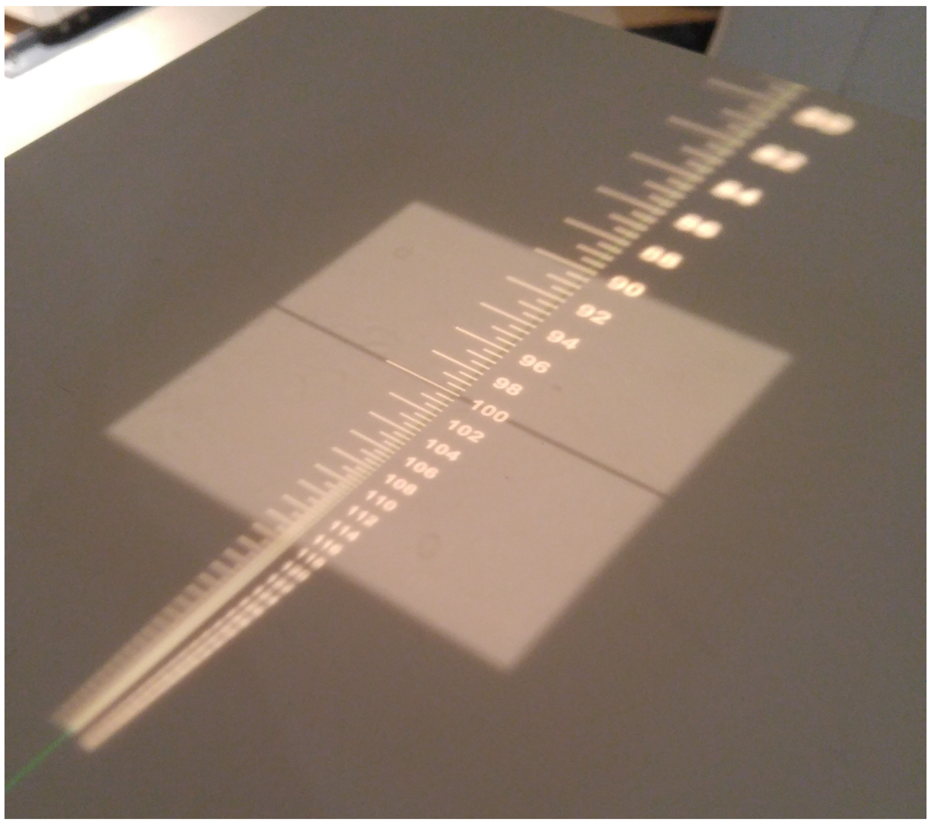

Figure 2.8: Optical distance indicator (ODI) projected on a 10×10 cm^2 light field on Solid Water. The ODI is aligned to the field-light cross hair indicating 100 cm SSD.

Varian's Clinac 21EX and TrueBeam accelerators are used throughout this work. A general description of their internal specifications is provided below, along with a qualitative summary of the known changes implemented in the redesign of the TrueBeam.

2.3.1 Geometry of a Varian linear accelerator

A schematic representation of the head geometry of a Varian Clinac series and TrueBeam linear accelerator is shown in Figure 2.9. In photon mode, the tungsten target is in place and a flattening filter is located below the primary collimator. In the electron configuration, the target is removed and an energy-specific dual layer scattering foil is located below the primary collimator in the place of the flattening filter. The scattering foils are rotated in and out of the field on a carousel. For the remainder of this thesis, we will only consider accelerators operating in electron mode.

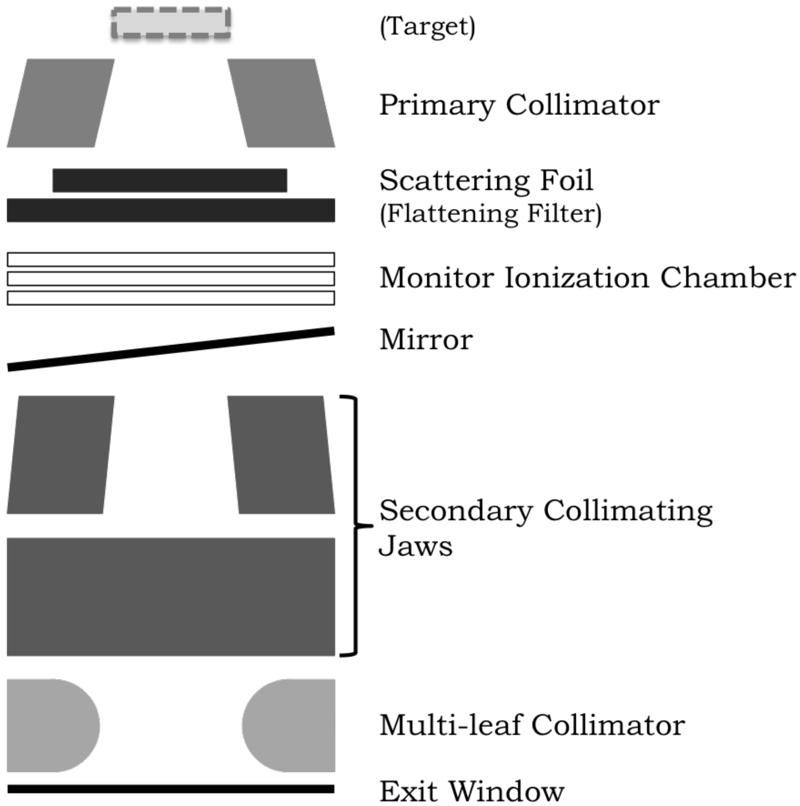

Figure 2.9: Schematic representation of a Varian linear accelerator head. Items listed in brackets and objected outlined in dashed lines are present only during photon beam production.

Because everything above the secondary collimating jaws is fixed, regardless of field size or gantry orientation, everything above the jaws can be referred to as “patient-” or “field-independent” geometry, while the secondary collimating jaws and MLC comprise the “patient-” or “field-dependent” geometry.

For the Clinac series accelerators, including the Clinac 21EX, a Monte Carlo data package describing both the field-dependent and field-independent portions of the accelerator head was made available under privacy agreement (2008 Varian Medical SystemsMonte Carlo Data Package). For the TrueBeam, Varian has published a Monte Carlo data package describing the field-dependent portions of the accelerator

(TrueBeam Monte Carlo Data Package), while the field-independent portions of the accelerator head remain proprietary. The MLC and electron applicators described in the respective Monte Carlo data packages are identical, and although the exact changes made to the field-independent portions of the TrueBeam are uncertain, some of the changes are known qualitatively. The bending magnet, carousel and scattering foils have been redesigned, the primary collimator is thicker than in previous generations of Varian accelerators and an anti-backscatter foil has been added to the exit of the monitor ionization chamber [19, 13, 41]. During the completion of this work, a technician from Varian disclosed that the anti-backscatter foil is only in place during the production of photon fields. The impact of this will be discussed further in Chapter 7.

2.3.2 Characteristics of an electron field

Classically, fields of electrons between 6 and 20 MeV have been used to treat superficial lesions no deeper than 5 cm from the skin surface such as skin and lip tumours, post-mastectomy chest wall, lymphatic nodes and cancers of the head and neck [61]. Conventionally, a flat and symmetric field profile is required to achieve uniform dose delivery in the target volume. The Report of AAPM Task Group 25 recommends that, in a reference plane corresponding to a depth of 95% dose along the PDD beyond d_{max}, the dose within 2 cm of the geometric beam edge for a field 10×10 cm^2 or greater should not vary more than $\pm 5\%$ and, ideally, fall within $\pm 3\%$. Additionally, the crossline and inline profiles should not differ more than 2% when comparing any two points equidistant from the central axis. To mitigate the impact of scatter in air, electron fields are typically shaped close to the skin surface, either using electron applicator and cutout systems or by placing lead shielding directly on the skin [62]. This has the effect of producing sharper penumbras for rapid dose fall-off at the field edges.

In contrast, the flatness and symmetry of an electron field used in MERT are not as important as long as they are accurately modelled. In principle, the treatment planning optimization process should account for non-uniformities in the shape of the dose in its determination of the best field arrangements and modulation for a particular plan. Sharp penumbras are still advantageous, however, and in MERT planning studies this has been achieved by moving collimators closer to the patient through the use of tertiary electron MLCs, or by moving the patient closer to the collimators with a short SSD.

Tertiary electron MLCs have been designed to collimate the field close to the patient surface by mounting to the existing electron applicators [108], or by using a retractable system that can be positioned at 63 cm or 100 cm source-to-collimator distances [47] (analogous to SSD). Another group used a retractable photon MLC placed between 71.6 cm and 81.6 cm source-to-collimator distances [82].

Investigations by Klein et al. [64] and du Plessis et al. [27] characterized the penumbras of electron fields shaped by the photon MLC inherent on Trilogy (Varian) and Primus (Siemens) accelerators at SSDs between 60 cm and 100 cm SSD. The Varian MLC, positioned about 47 cm from the source, was shown to produce acceptable field definition up to 85 cm from the source while the Siemens MLC, positioned about 40 cm from the source, was shown to produce acceptable field definition up to 70 cm. In both cases, penumbra broadening was reduced by reducing the SSD.

Electron fields are shaped with applicators and with the MLC in this work. A description of the applicator and MLC systems used on the Clinac 21EX and TrueBeam accelerators are described below.

Applicators and cutouts

Figure 2.10 depicts a 10×10 cm^2 applicator and cutout mounted to the TrueBeam. Each applicator has three shaping blocks along its length positioned about 65 cm, 79 cm and 95 cm from the source and are between 1.3 and 2.0 cm thick. The blocks are made of zinc alloy and their inside faces follow some divergence along the beam axis. The block furthest from the source (closest to isocenter), is designed to receive a Cerrobend insert responsible for defining the final shape of the beam. Cerrobend cutouts may define standard circular or rectangular fields, or may be fabricated to match the projected outline of a target volume. The applicators used on the Varian Clinac 21EX and TrueBeam linear accelerators come in 6×6, 10×6, 10×10, 15×15, 20×20 and 25×25 cm^2 field sizes, projected to isocenter, with inserts available for 3×3, 4×4 and 5×5 cm^2 square fields, also projected to isocenter.

Although the applicators on the Clinac 21EX and TrueBeam are identical, each machine uses jaw positions specific to the applicator-energy combination being used. While some applicator-energy combinations are the same for both machines, this is not the case for every combination. Jaw positions for each machine-applicator-energy combination are summarized in Figure 4.1 (Chapter 4).

Figure 2.10: Photo of a 10×10 cm^2 electron applicator and cone mounted on the TrueBeam.

Multi-leaf collimators

Both the Clinac 21EX and TrueBeam linear accelerator use the Millennium 120-leaf multi-leaf collimator. This MLC design has 40 central leaf pairs and 20 outer leaf pairs whose widths project to 0.5 and 1.0 cm at isocenter, respectively. The tungsten leaves are about 6.5 cm thick along the beam axis and their edges follow the divergence of the beam while their ends are rounded. The leaves are oriented to move in the crossline direction when the collimator rotation is set to 0°. The MLC is located inside the linear accelerator head, about 47 cm from the source.

In normal operation of both the Clinac 21EX and the TrueBeam, there is a safety interlock that prevents electron fields from being delivered without an applicator mounted and the MLC retracted. In order to deliver the opposite configuration (no applicators using MLC shaping), both accelerators were operated in Service Mode where interlocks for the MLC and applicators could be overridden.

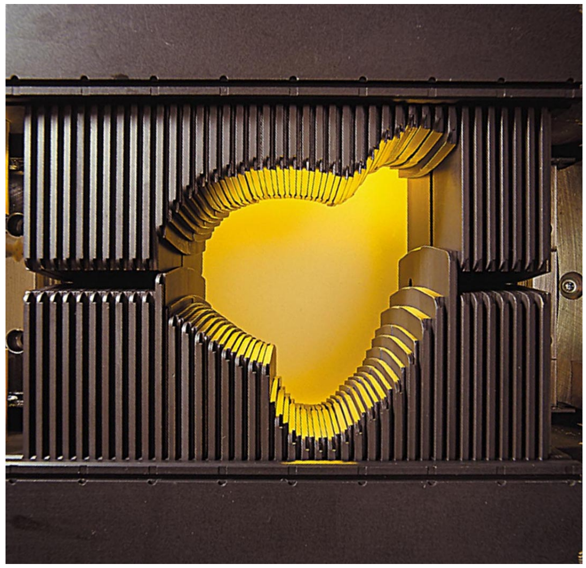

Figure 2.11: Photo of the Varian Millennium-120 multi-leaf collimator taken looking toward the source. Image courtesy of Varian Medical Systems Inc.

2.3.3 Linear accelerator output and backscatter

The monitor ionization chamber, or monitor chamber, is used to measure the output of a linear accelerator and display this output on the control console as monitor units (MU). While monitor units have no universal quantitative definition, they are used to define the output of a specific machine. For example, in most clinics, 1 MU is the signal produced in the monitor chamber that corresponds to the delivery of 1 cGy of dose to isocenter under reference conditions.

The monitor chamber is also used to track the rate at which dose is delivered in units of MU per minute. Variable dose rate is useful in radiation therapy in a number of capacities. High dose rates are desirable when fields have a high degree of modulation and a large number of monitor units are required to deliver the prescription dose, while there is some evidence that low dose rates may reduce acute radiation side effects in some treatment techniques [14, 39].

Ideally, a monitor chamber would measure only the forward directed radiation and the output of the machine would correspond one-to-one with the monitor unit reading. The proximity of the secondary collimating jaws downstream of the monitor chamber, however, means that there is some backscatter from the top surface of the jaws as they move into the radiation field which contributes to the monitor chamber reading. The AAPM Task Group Report 74 [118] defines the output backscatter factor, S_{b}, as

$$S_{\mathrm{b}} = \frac{(1 + b(A_{\mathrm{ref}}))}{(1 + b(A))}, \tag{2.7}$$

where $b = MU_{\mathrm{b}}/MU_0$ is the ratio of monitor units due to backscattered (MU_{b}) and forward directed signal (MU_0) for a reference field, A_{ref}, and for a field of interest, A. Zavgorodni et al. [116] used the fact that the forward signal is independent of field size to present a more intuitive definition of S_{b},

$$S_{\mathrm{b}} = \frac{(MU_0 + MU_{\mathrm{b}})_{\mathrm{ref}}}{(MU_0 + MU_{\mathrm{b}})_{\mathrm{field}}} = \frac{MU_{\mathrm{ref}}}{MU_{\mathrm{field}}}. \tag{2.8}$$

This formalism assumes MU_0 to be fixed, and that changes in MU_b will be reflected in the total cumulative monitor unit reading for a fixed delivery time, or in the time to deliver a fixed number of monitor units. In normal operation of Varian accelerators, dose and a pulse forming network (PFN) servos maintain a nearly constant dose rate and fixed delivery time, therefore, if MU_b increases, MU_0 decreases and the overall monitor unit reading and time to deliver are unchanged. In order to apply equation 2.8, the accelerator must be operated with the dose and PFN servos turned off, in which case, the time to deliver a fixed number of monitor units may vary and the monitor unit reading for some time interval is directly proportional to the dose rate. By extension,

$$S_{\mathrm{b}} = \frac{MU'_{\mathrm{ref}}}{MU'_{\mathrm{field}}}, \tag{2.9}$$

where MU' is the dose rate measured by the monitor chamber in units of MU/min. Equation 2.9 is used to calculate values of S_{b} based dose rates measured using the delivery timing and dose rate sampling techniques described in Chapter 7.

2.4 Monte Carlo methods

Monte Carlo methods for simulating particle transport in radiation oncology physics use pseudo-random number generators, attenuation coefficients and differential cross-sectional data to simulate the path-lengths, interactions and energy transfers of individual particles [92, 99]. While deterministic or analytical approaches employ macroscopic models for particle transport theory, Monte Carlo techniques directly access the fundamental microscopic properties of the transport mechanism to solve the macroscopic system [99]. In radiation oncology physics, Monte Carlo dose calculations are considered to be the gold standard because they are the only simulation tool available that explicitly model the underlying physics of particle transport in matter, which have been well understood for decades [20].

Monte Carlo methods have a long history in radiation oncology physics, not only for the simulation of dose deposition within a patient or phantom, but for the simulation of stopping-power ratios used in electron dosimetry, and for modelling the response of ionization chambers [93], both essential components of the gold standard beam calibration techniques adopted by much of medical physics community [7, 76, 102].

The statistical uncertainty of a Monte Carlo solution diminishes as $1/\sqrt{N}$ where N is the number of samples [99]. In the case of particle transport, we consider histories, where a history describes the path and interactions of a primary particle, as well as the paths and interactions of all resulting "daughter" particles. Schematically, this is presented in Figure 2.12 where photons are presented as solid, black lines and electrons are presented as green, dashed lines.

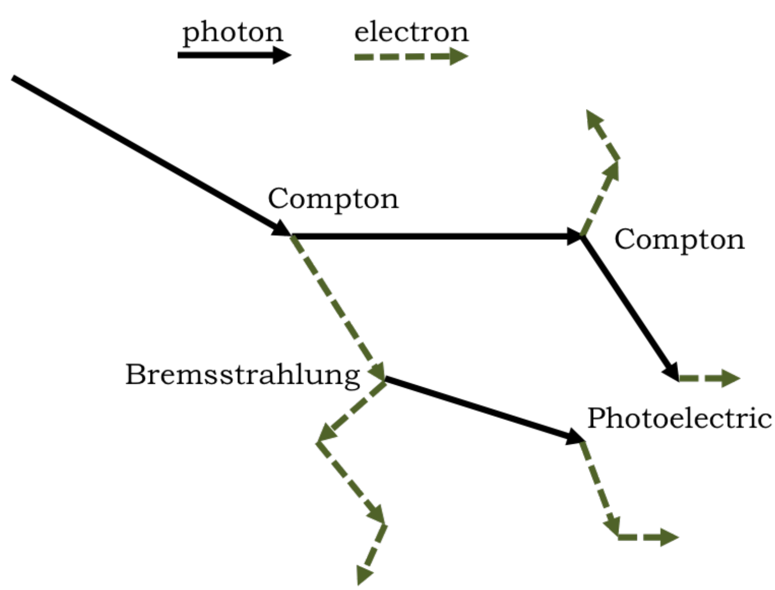

Figure 2.12: Example of a Monte Carlo particle history beginning with a primary photon.

2.4.1 Variance reduction and approximations

In the absence of efficiency driven approximations, Monte Carlo simulations demonstrate superior accuracy compared to most analytical methods [20, 92, 107]. The time consuming nature of the Monte Carlo method motivates efficient computation, however, and variance reduction techniques are employed to shorten calculation times. By strict definition, variance reduction will not change the result of an infinitely long Monte Carlo simulation [99]. Particle splitting is an example of variance reduction that will be described here. Range rejection, condensed histories and continuous slowing down approximation (CSDA) are approximations that improve the efficiency of particle transport simulations and will also be described.

Particle splitting

Particle splitting meets the criteria of a variance reduction technique as defined above [99] because in the limit of infinite histories, Monte Carlo simulations run with or without particle splitting will reach the same solution. Particle splitting can be applied to both photon and electron interactions, but is commonly presented in the context of bremsstrahlung photon production. Suppose a single electron interaction in a material produces a single bremsstrahlung photon. By employing particle splitting, the weight of that single photon can be divided and assigned to some number of photons that can, in turn, be simulated independently. This speeds up the production of bremsstrahlung photons, particularly in the case of bremsstrahlung production in a linear accelerator target, by saving the time required to transport additional electrons that will likely be absorbed in the target.

Range rejection

In range rejection, the maximum range of a particle, defined by its energy and the medium, is compared with the distance to the nearest boundary. If the particle range is less than this distance, the transport simulation stops and the particle's remaining energy is deposited locally. Because range rejection requires the definition of a maximum range, this approximation only applies to charged particles [99]. This can be very useful in simulating accelerator head geometries where electrons are likely to be absorbed in a high-Z material.

The approximation in this approach lies in neglecting the production of bremsstrahlung photons along the remainder of the charged particle track which could, potentially, carry energy out of the region [56]. By setting a threshold energy above which range rejection will not be performed, the impact of this approximation can be minimized.

Condensed histories and continuous slowing down approximation

Particle transport is modelled in Monte Carlo simulations by explicitly tracking the sequential interactions and energy transfers of individual particles along their trajectories in histories. Given that an individual electron may undergo hundreds of thousands of interactions, creating additional electrons that will undergo additional interactions, it is impractical to model each of these interactions individually [58]. Instead, condensed histories are used to simulate large numbers of transport and interaction processes in a single step, resulting in some change in energy and direction at the end of a specified step size [59].

Condensed history techniques are either class I or class II. In class I techniques, all energy loss is modelled on a predetermined grid. In class II techniques, "catastrophic interactions" that involve energy transfers above some threshold energy in the production of bremsstrahlung radiation or delta rays are modelled explicitly while interactions that do no exceed this threshold are modelled by a continuous slowing down approxmiation (CSDA) [58]. In a CSDA model, the range, R, of a particle's path is calculated as a function of stopping power in the medium integrated over the energy range of the particle as

$$R_{CSDA} = \int_{E_f}^{E_0} \frac{dE}{S_{tot}(E)}, \tag{2.10}$$

where E_0 is the initial energy of the electron, E_f is 0 or the cut-off energy of the electron where it is assumed the remainder of its energy is deposited locally and S_{tot} is the total stopping power in the medium due to collisional and radiative interactions [106].

2.4.2 Monte Carlo packages for radiation therapy

In Chapter 1, some Monte Carlo packages were described that are available commercially with purchase of a software license. There are also a number of Monte Carlo systems freely available for use in radiation oncology physics research. The most common packages [8, 30] are based on the Geant4 [1], PENELOPE [11] and EGSnrc [56] transport codes. Articles have been published comparing the performances of

EGSnrc, Geant4 and PENELOPE for simulation of electron scatter [30] and energy deposition [8], showing each algorithm to have its own strengths and weaknesses.

The advantage of EGSnrc lies in its user codes, BEAMnrc [94] and DOSXYZnrc [111], which include pre-coded and easily customizable geometries common to radiation therapy applications. Recently, the PENELOPE-based package, PRIMO, has been made freely available for medical physics research use [90]. PRIMO is easy to install and has a straight-forward graphical user interface making it attractive for users with limited experience using a command line environment, however, it is hard-coded to model specific Varian and Elekta accelerators and so does not provide the flexibility to modify accelerator geometries as in the BEAMnrc and DOSXYZnrc packages.

EGSnrc and its user codes are used throughout this work for Monte Carlo simulations of electron fields generated by Varian Clinac 21EX and TrueBeam linear accelerators, and are described in greater detail below.

EGSnrc: BEAMnrc and DOSXYZnrc

The EGSnrc transport code was adapted for radiation therapy physics applications by the Canadian National Research Council based on the EGS transport code developed at Stanford [31] for particle physics research. EGSnrc uses class II condensed history [58] and the PEGS4 material data generation system [56]. It is the underlying transport code that governs calculations performed in the BEAMnrc and DOSXYZnrc user codes, and transport parameters including cross-sectional data and variance reduction techniques employed are specified in the input files of the user codes.

BEAMnrc was developed in order to model radiation therapy sources [94]. The package contains a number of primary source models including point sources, scanning sources and allows for phase-space sources. Phase-space source files are a record of particles that pass through a particular simulation plane, including positional, trajectory and energy information. Phase-spaces can be useful for speeding up radiation therapy simulations, for example, by allowing a user to simulate the field-independent portion of the accelerator geometry once and record the results in a phase-space that can be used as the source for subsequent simulations of the field-dependent accelerator components.

One of BEAMnrc's strengths is in its component modules which take on typical geometries used in radiation therapy field generation including flattening filters, scattering foils and MLCs. The particular component modules used and their order in the accelerator geometry are defined when an accelerator model is compiled, but the exact dimensions and positioning of each module is defined in the BEAMnrc input file each time a simulation is run (the position of each module must respect the module ordering specified when the model was compiled and modules may not overlap).

The user code DOSXYZnrc is used to model phantom or patient geometry and calculate dose distributions on a rectangular grid following simulation of the radiotherapy sources modelled in BEAMnrc [111]. The grid is a matrix of three-dimensional volume elements, called voxels, into which energy may be deposited during the simulation. DOSXYZnrc may use the program `ctcreate` to convert CT image data into a phantom file (.egsphant) that contains boundary, material assignment and density information for each voxel. Alternatively, the dimensions and material assignments of a rectangular prism may be specified directly in the DOSXYZnrc input file (.egsinp). At the conclusion of the simulation, dose is reported in a 3-D dose file (.3ddose) that specifies the boundaries, calculated dose and associated uncertainty in each voxel.

BEAMnrc and DOSXYZnrc are used throughout this work for Monte Carlo dose calculations. Their use will be described in greater detail in the following chapter (Section 3.2).

Chapter 3

Methods & Materials

Many of the same measurement and simulation techniques are used throughout Chapters 4 – 7. In order to avoid repetition, they are presented here in detail and will be referenced in later chapters. Measurements of output, profile and depth dose scanning as well as film processing are presented. Use of the Monte Carlo transport code, EGSnrc [56], and its user packages, BEAMnrc [94] and DOSXYZnrc [111] as part of the Vancouver Island Monte Carlo system [115] and from the command line are described. Finally, a summary of gamma-index analysis and its implementation in this work is summarized.

3.1 Measurements

3.1.1 Outputs

Relative output measurements were performed throughout this work using a Markus ionization chamber in Solid Water. Measurements were performed at various depths with a minimum of 10 cm backscatter material in place. Figure 3.1 shows the Markus chamber setup in Solid Water before placing additional layers of Solid Water on top for buildup.

The Markus chamber was aligned along the central beam axis using the light field crosshairs and vertically positioned using the ODI described in Chapter 3. Dose uncertainty resulting from up to a 2 mm error in vertical positioning of the Solid Water surface was estimated using the technique outlined by Khan and Sewchand [60] to be less than 0.65%, although monthly tracking of the ODI's precision suggested it to be better than 2 mm, even at 70 cm SSD. Dose error associated with a 1 mm mis-

Figure 3.1: Markus ionization chamber in Solid Water for output measurements. Various thicknesses of Solid Water were stacked on top of this set up prior to measurement. Photo credit: Evan Maynard.

alignment of the detector orthogonal to the beam axis was less than 0.3%. Summed in quadrature, uncertainty associated with setup was 0.72%.

Signal from the Markus chamber was read out using a PTW Unidos E Universal Dosemeter (PTW-Freiburg, Freiburg, Germany) with a -300 V bias voltage. The detector and electrometer were "warmed up" prior to data acquisition by delivering 200 MU before commencing measurements.

3.1.2 Depth and profile scans

During the clinical commissioning of the Clinac 21EX and TrueBeam linear accelerators, an electron field diode was used to acquire depth and profile scans of applicator and cutout shaped electron fields in water at 100 cm SSD. This data was acquired by the clinical physicists responsible for commissioning and copies were obtained for comparison. Additional profile and depth scans of MLC shaped electron fields delivered in water at 70 cm SSD were performed specifically for this work.

All of the scanning diode data were acquired in a large water tank ($48 \times 48 \times 41$ cm^3) shown in Figure 3.2. A set of robotic tracks is mounted onto the tank to move

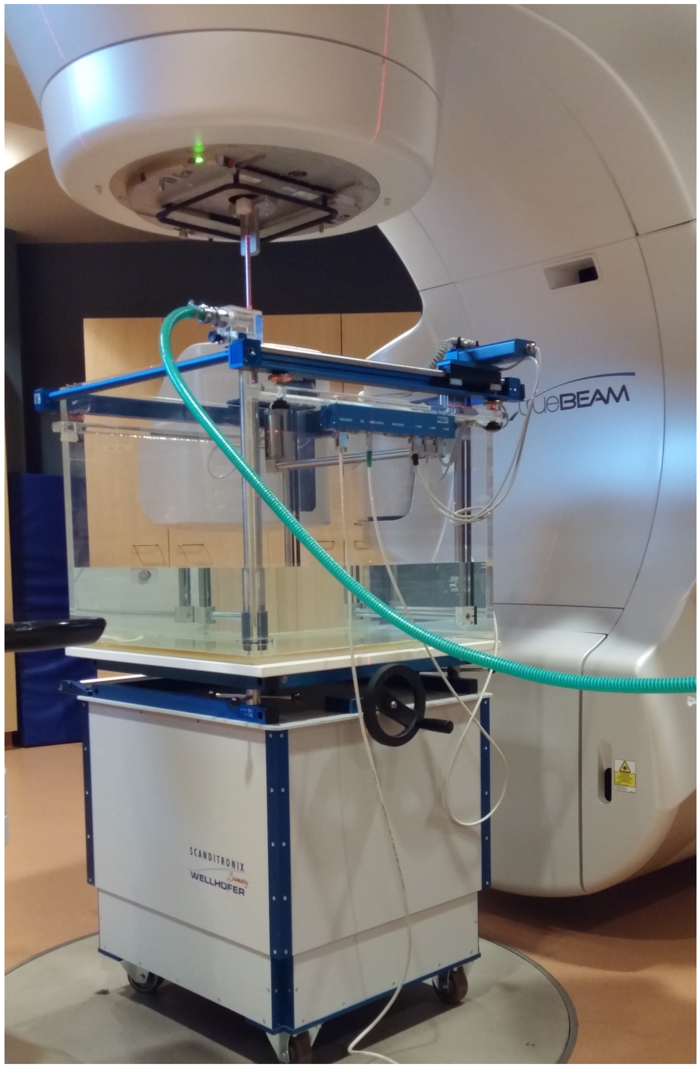

Figure 3.2: Large $48 \times 48 \times 41$ cm^3 water tank used to perform relative measurements of profile and depth dose curves.

the detector along profile and depth curves during acquisition. Level positioning of the detector is ensured by moving it throughout its range of lateral motion along the water surface to verify that its position relative to the surface does not change. To set the vertical position of the detector, the diode was raised from below the water's surface until the apparent gap between the detector and its reflection on the surface of the water was eliminated. A cross hair on the top surface of the detector was aligned with the field light cross hair for lateral positioning. A reference detector was placed in a fixed position near the field edge to correct for noise in the output of the machine.

Primary and reference detector signals were read out using a PC running the software OmniPro-Accept (IBA Dosimetry, Schwarzenbruck, Germany) which was also used to control the scanning motion of the diode along the robotic tracks. OmniPro-Accept corrects the primary signal using the reference, plots the relative data and can be used further processing and analysis. All depth and profile scans were smoothed using a 5 mm sliding window and profiles were centered about the central axis.

After processing, data was exported for analysis in MATLAB (MathWorks, Natick, MA). MATLAB scripts were written to determine the depths of 90%, 80%, 50% and 20% dose (d_{90}, d_{80}, d_{50} and d_{20}), the full width at half maximum (FWHM), 80%-20% penumbra width (width of penumbra measured between 80% and 20% doses on the profile shoulder), flatness (the variation over the mean within 80% of the FWHM) and photon contamination, D_x (the dose beyond the electron range due to photons). Results from the MATLAB scripts were checked against the values determined by OmniPro-Accept to verify accuracy. Depth and width parameters were reproducible within 0.1 cm while photon contamination was reproducible within 0.1% and flatness was reproducible within 1%. The benchmarked scripts were then used to determine depth and width parameters for both measured and Monte Carlo simulated data.

OmniPro-Accept does not report measurement uncertainties, so the noise in each of the signals was used to approximate the overall uncertainty in dose as 1.1%. The uncertainty in depth and width parameters calculated based on this data was estimated by determining the range in depth or width associated with a 1.1% shift in the curve up or down. This is shown schematically in Figure 3.3. Setup uncertainty was estimated to be within 0.05 cm laterally and 0.1 cm vertically. Uncertainty is greater vertically to account for water evaporation during scanning. For the most part, uncertainty in position metrics was found to be within 0.1 cm except measures of penumbra which are within 0.2 cm. Uncertainty in flatness is within 2%.

The Scanditronix diode was used to acquire commissioning data for the Clinac 21EX, while the IBA diode was used for all other measurements. As part of the machine commissioning process, each diode was cross-calibrated against a Markus chamber to establish suitablity for acquiring commissioning data. Signal from the Scanditronix diode was corrected using another Scanditronix diode as the reference while the signal from the IBA diode was corrected using a CC13 ionization chamber reference.

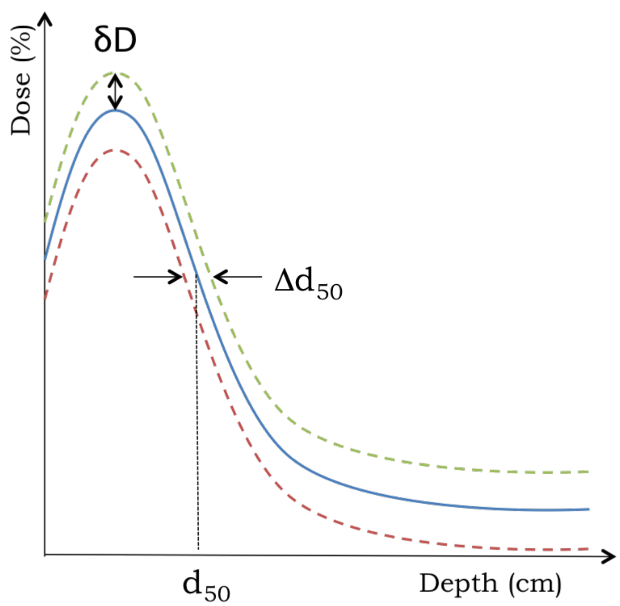

Figure 3.3: Estimation of uncertainty in depth associated with diode signal noise. Magnitudes are exaggerated for the purpose of demonstration.

3.1.3 Film

Film measurements were performed using Gafchromic® EBT2 (Clinac 21EX) and EBT3 (TrueBeam) radiochromic film. Measurements were performed with film placed between slabs of Solid Water positioned orthogonal to the beam axis. Irradiated films were scanned on an Epson Expression 10000XL scanner (Seiko Epson Corporation, Suwa, Japan) in transmission mode at 150 dpi and processed using MATLAB according to the procedure outlined by Garcia and Azorin [36]. Using the red channel from each scan, images were corrected for scanner and film non-uniformities by subtracting a scan of an un-irradiated film. Irradiated and un-irradiated films were registered by manually matching the edges of the film in MATLAB. The resulting images were smoothed using a 2D median filter ($\sim 4 \times 4$ mm) and converted to optical density (OD).

Conversion from OD to dose was done using energy-specific calibration curves created for each batch of film. These calibration curves were constructed by irradiating small pieces of film to known doses between 0 and 300 cGy in 50 cGy increments and fitting their responses to a second order polynomial. Examples of these calibration curves are shown in Figure 3.4. Note the reduced energy dependence demonstrated by EBT3 calibration curves compared to EBT2 calibration curves.

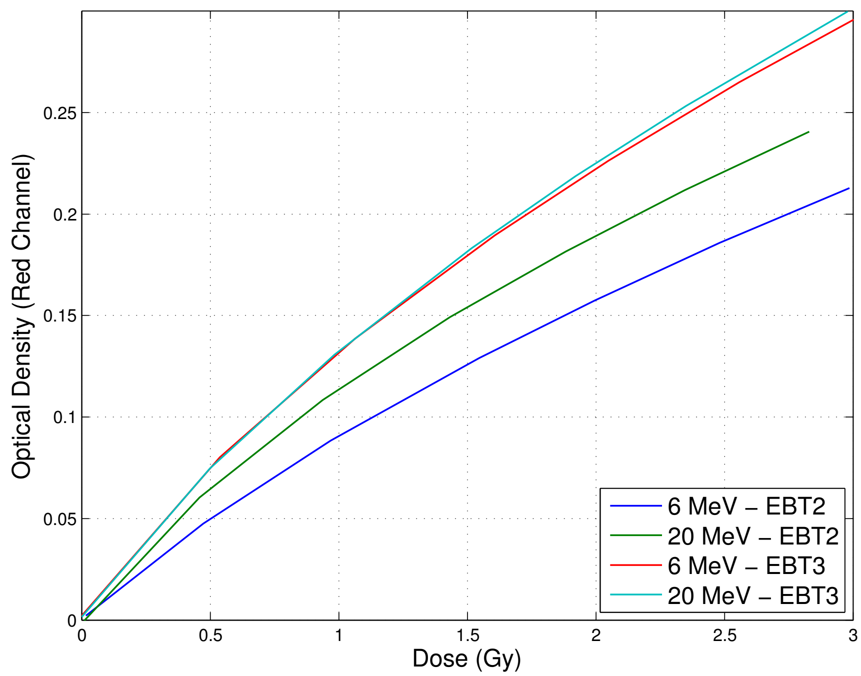

Figure 3.4: Representative optical density (OD) to dose calibration curves for EBT2 and EBT3 radiochromic film.

To assess the measurement uncertainty associated with processing, the same film was scanned and processed three times, and the standard deviation between each pixel value was determined. To assess the measurement uncertainty associated with set up and delivery, four different films irradiated with the same field and energy were scanned and processed, and the standard deviation between each pixel value was evaluated. These standard deviations were added in quadrature to determine the final measurement uncertainty.

3.2 Monte Carlo dose calculations using BEAMnrc and DOSXYZnrc

The EGSnrc [56] user codes, BEAMnrc [94] and DOSXYZnrc [111], are used throughout this work for Monte Carlo simulation of electron fields, and are described in Section 2.4. These codes were run both on the command line and through the Vancouver Island Monte Carlo (VIMC) interface [115]. The details of each approach are summarized later on.

Table 3.1 summarizes the particle transport parameters used for the simulations presented in Chapter 5 (Complete Accelerators) and in Chapters 6 and 7 (Phase-space Simulations). The specifics of the parameter sets used for each set of simulations will be described in further detail in the appropriate chapters, however, the transport parameters are discussed briefly here.

Table 3.1: EGSnrc Monte Carlo transport parameters used in this work.

Transport Parameter	Complete Accelerators	Phase-space Simulations
SMAX (cm)	5	10^{10}
ESTEPE (%)	0.25	
Boundary Crossing Algorithm	PRESTA-I	EXACT
Skin Depth for BCA (mean free paths)	0	
Electron-step Algorithm	PRESTA-II	
Spin Effects	On	
Brem Angular Sampling	Simple	
Brem Cross Sections	BH	
Bound Comp Scattering	Off	
Pair Angular Sampling	Simple	
Pair Cross Sections	BH	
Photoelectron Angular Sampling	Off	
Rayleigh Scattering	Off	
Atomic Relaxations	Off	
Electron Impact Ionization	Off	

`PRESTA-II` is the default condensed history electron transport algorithm in EGSnrc [59], and was used for this work. The `PRESTA-I` algorithm, originally used in EGS4 and available as a transport option in EGSnrc, was known to suffer from truncation errors in the limit of large condensed history step size [59], underestimation of lateral deflections [56], and production of singularities caused by forced multiple scattering events at boundaries in which the the particle was scattered parallel to the boundary [58]. These issues have been addressed in `PRESTA-II` [56].

The `EXACT` boundary crossing algorithm transports electrons in single scattering mode when they are within the `Skin Depth` from a boundary [94]. In contrast, with `PRESTA-I` boundary crossing, once the electron is within `Skin Depth` from a boundary, lateral correlations, which account for lateral deflections in electron transport, are turned off and a multiple scattering event is forced [58]. The parameter `SMAX`, which defines the maximum electron step length in centimetres, is set to 5 cm for `PRESTA-I` boundary crossing and to 10^{10} cm for `EXACT` boundary crossing, as recommended by the BEAMnrc manual [94]. `ESTEPE` defines the maximum fractional energy loss, and has a recommended value of 0.25.

For the most part, default or recommended transport parameters [94] were used throughout this work. The boundary crossing algorithm, `PRESTA-I`, used for the complete accelerator models was inherited from the complete photon accelerator models that the Chapter 5 electron models were based on. Bethe-Heitler (`BH`) bremsstrahlung and pair production cross sections are used [25], and only the first terms of the Koch and Motz [66] and Motz [77] equations are used for angular sampling in bremsstrahlung and pair production interactions, respectively.

Additional simulation parameters will be provided in the chapters in which they are described. The hardware and software specifics of running BEAMnrc and DOSXYZnrc are discussed below.

3.2.1 Vancouver Island Monte Carlo

The Vancouver Island Monte Carlo system (VIMC) at the BC Cancer Agency's Vancouver Island Centre is well characterized by Townson [105] and Zavgorodni [115]. The system is made up of integrated servers, software and a web interface called WebMC that allows users to perform Monte Carlo simulations without specialized training in the use of BEAMnrc or DOSXYZnrc.

The front end of the VIMC system is a Mac Pro with four 2.8 GHz processors and 4 GB RAM. The computational cluster is made up of three nodes, each with four 2.1 GHz 64-core processors, 192 GB RAM and a 7200 RPM hard drive. For efficiency, most of the simulations performed using VIMC were split into 64 subfields which were run in parallel and summed upon completion.

Typically, users will create dose delivery plan using Varian's treatment planning software, Eclipse, and export it in DICOM standard medical imaging format to be uploaded to VIMC through the WebMC browser interface. This data includes a CT image set, structure contours associated with the CT, specifications for the radiation delivery such as field shapes and arrangements, and the resulting dose distribution. This data is stored on a front end node and made available to the three cluster nodes used to perform simulations.

Once a plan has been uploaded to VIMC, a user may initiate a simulation based on the data provided. The user may select the accelerator model that will be used as well as the resolution of the three-dimensional grid on which the simulation is to be performed. The volume in which dose is to be deposited may be specified based on CT image data using `ctcreate`, or the dimensions of a rectangular prism may be specified and materials assigned within the DOSXYZnrc input file directly. WebMC creates the .egsinp files required to initiate BEAMnrc and DOSXYZnrc simulations based on the user's specifications and those provided in the plan data. It then launches the BEAMnrc simulation, followed by the DOSXYZnrc simulation using the results of the BEAMnrc simulation as input. When the DOSXYZnrc simulation has completed, WebMC performs post-processing to turn the .3ddose output file into a DICOM formatted dose file that can be imported back into the Eclipse treatment planning software for evaluation.

For most users, the accelerator models already established in the webMC platform are sufficient for their intended calculations. To create new accelerator models, WebMC provides an infrastructure by which to copy an existing accelerator using new .module and .egsinp files which specify the component modules that will be used in the new accelerator model. While the specifications of each component module may be modified following the creation of a new accelerator model, the component modules used and their arrangement in the model are fixed.

When this research began, only photon models were available for use in WebMC. These models were copied and modified in order to simulate electron fields. The exact modifications will be discussed in Chapter 5, however, the process of modifying parameters in the accelerator model is not currently a feature in the WebMC interface, and so .egsinp files were accessed from the file directory during the submission process and modified for the purposes of model tuning.

3.2.2 Command line

For simulations of backscatter described in Chapter 7, BEAMnrc was run alone from the command line on the front end of the VIMC computational infrastructure. Accelerators were specified and complied as outlined by Rogers [94] and simulations were performed individually with no parallel processes.

3.3 Gamma analysis

Measurements and simulations of dose in radiation therapy are sensitive to positioning uncertainty and often contain regions of high dose gradients. When comparing dose arrays, a pixel-by-pixel or voxel-by-voxel dose difference comparison has limited value. The gamma comparison [73] combines dose difference with a distance to agreement parameter to quantify the agreement of two dose arrays within positional uncertainty for a single value.

Suppose a measured dose array, $[D_m(r_m)]$, is being compared to a calculated dose array, $[D_c(r_c)]$. We can specify that the arrays agree if, at each data point in the calculated set, there is a data point in the measured set at the same location, or within some distance to agreement, Δd, that falls within some dose difference, ΔD, of the calculated dose. If we are considering a $1 \times n$ array, the dose $[D_m(r_m)]$ can be compared against the array $[D_c(r_c)]$ such that

$$\Gamma(r_m, r_c) = \sqrt{\left(\frac{|r_c - r_m|}{\Delta d}\right)^2 + \left(\frac{D_c(r_c) - D_m(r_m)}{\Delta D}\right)^2}, \tag{3.1}$$

and

$$\gamma(r_m) = \min\{\Gamma(r_m, r_c)\}\forall\{r_c\} \tag{3.2}$$

where γ is the gamma-index.

If the gamma-index is less than 1 for a given point, that point falls within the gamma criteria, $\{\Delta D, \Delta d\}$, in comparison to the reference array, $[D_c(r_c)]$. If the gamma-index is greater than 1, then the the data point does not fall within the gamma criteria. The overall agreement of the arrays can be reported as a percentage of points with passing gamma indices given the specified criteria. This analysis is extended to two and three dimensions in the paper by Low et al. [73].

In this work, a 1D gamma function was written in MATLAB to compare measured and simulated profile and depth dose curves, and is used throughout Chapters 4 through 6.

Chapter 4

Results & Discussion I: Dosimetric comparisons of electron fields generated by the TrueBeam and the Clinac 21EX

Accurate Monte Carlo simulations of clinical electron fields require accurate models of the linear accelerators used to produce them. Ideally, a complete model of the accelerator's internal geometry would be used to perform simulations of complex electron fields pertinent to MERT and MPERT research. Simulating the true geometry of the linear accelerator provides the greatest freedom to investigate the specific transport and interaction mechanics involved in beam production. Varian has kept the field-independent geometry of the TrueBeam proprietary so explicit simulation of radiation production based on exact machine schematics is impossible. In contrast, schematics are available for the field-dependent and field-independent head component of Varian's Clinac, Trilogy and Novalis accelerators. If the beam properties of the TrueBeam are not significantly different compared to these machines, it may be possible to modify an existing Monte Carlo model of a Clinac 21EX accelerator to simulate beams produced by the TrueBeam.

A number of articles have been published characterizing the dosimetric properties of the TrueBeam. Chang et al. [19], Beyer [13], and Glide-Hurst et al. [41] performed comparisons of select photon and electron fields from unmatched TrueBeam units; in the Beyer and Glide-Hurst et al.[41] studies, the units were installed in different centers. All three studies found their respective machines to be in excellent agreement with one another, Beyer citing percent depth dose (PDD), profile, and output measurements to be reproducible between machines within 2%. Overall, the TrueBeam was found to be dosimetrically consistent from one machine to the next.

Additionally, Beyer compared TrueBeam photon fields with those produced by Varian Trilogy and Clinac 2100 accelerators to evaluate the possibility of beam-matching. They showed output factors to agree within 2%, PDDs to agree within 1%, and profiles to agree within 2% and 1 mm, for the most part, between the three machines. Slight differences in profile and penumbra width were attributed to changes in the material and design of the flattening filter and other linear accelerator head components that contribute to scatter, as well as to changes in the bending magnet impacting the incident electron source width. This was also cited as the cause of differences in the profile shoulder shape at distances greater than 20 cm from the central axis. In general, TrueBeam photon fields were found to be within 2%/2 mm of those produced by older Varian units, with differences occurring for small fields and very large fields.

The purpose of this chapter is to present a dosimetric comparison of electron fields generated by the TrueBeam and the Clinac 21EX, and to determine if the beams are sufficiently similar (i.e. within 3%/3 mm) to warrant modification of a complete Clinac 21EX accelerator model in order to simulate electron fields that are dosimetrically equivalent to those produced by the TrueBeam, within 3%/3 mm. Normally, for clinical work, dose calculations should agree with measurement within 2% or 2 mm [88], however, the aim of this work is to develop a model that will be used for proof-of-principle work in a MERT/MPERT optimization and treatment planning research system, so 3%/3 mm agreement is sufficient.

This is the first dosimetric comparison of TrueBeam electron fields with those from an older Varian machine. Specifically, this study investigates fields ranging in size from 5×5 to 25×25 cm^2 and in energies from 6 MeV to 20 MeV, shaped using electron applicators at 100 cm SSD, and by the MLC without applicators at short SSD as would be employed in MERT. Given that the Clinac 21EX head geometry is shared by Varian's iX, Trilogy, and Novalis TX accelerators, it is expected that this comparison can be extended to the latter machines.

4.1 Applicator-defined fields

4.1.1 Methods

Commissioning data for the Clinac 21EX and TrueBeam accelerators were acquired following the installation of each machine, in 2000 for the Clinac 21EX and in 2012 for the TrueBeam. Subsets of the commissioning data from each machine included depth and profile scans taken at 100 cm SSD with 6×6, 10×10, 20×20 and 25×25 cm^2 electron applicators, using 6, 9, 12, 16 and 20 MeV electrons. Default jaw settings were used for each of the applicator sizes as programmed for each machine and are summarized in Table 4.1. Measurements of the Clinac 21EX beam data were performed using Scanditronix diodes as the primary and reference detectors and processed using OmniPro-Accept v6.6 (Scanditronix/Wellhofer, Schwarzenbruck, Germany). TrueBeam measurements were performed using the EFD^{3G} scanning electron field diode with a CC13 ionization chamber reference, and processed using OmniPro-Accept v7.4 (IBA Dosimetry, Schwarzenbruck, Germany). Diode and ionization chamber specifications are provided in Section 2.2.

Table 4.1: Default jaw settings, in cm^2, for electron applicator fields as programmed for the Clinac 21EX and TrueBeam linear accelerators. Jaw settings are symmetric and the same for X- and Y-jaws.

	Applicator Size (cm^2)							
Energy	6×6		10×10		20×20		25×25	
(MeV)	21 EX	TB	21 EX	TB	21 EX	TB	21 EX	TB
6	20	20	20	22	25	27	30	32
9	20	20	20	20	25	25	30	30
12	11	11	14	15	25	25	30	30
16	11	11	14	15	23	23	28	28
20	11	11	14	14	22	22	27	27

Both sets of measurements were performed in a large water tank ($48 \times 48 \times 41$ cm^3) with profile measurements taken at nominal values of d_{max} and d_{50}, the depths of maximum and 50% dose, respectively. Nominal values of d_{max} and d_{50} for both sets of commissioning data are specified in Table 4.2. The exact values of these depths are not known *a priori* and so the values used during commissioning may be based on prior commissioning data sets or initial depth scans. Because these machines were installed more than ten years apart, the team of physicists responsible for performing these measurements was not constant.

Table 4.2: Nominal values of d_{max} and d_{50} for commissioning measurements of applicator shaped profiles for the Clinac 21EX and TrueBeam linear accelerators.

Accelerator Model	Depth	Energy (MeV) 6	9	12	16	20
TrueBeam	d_{max} (cm)	1.4	1.9	2.8	**2.9**	2.4
	d_{50} (cm)	2.4	3.7	5.1	6.7	8.3
Clinac 21EX	d_{max} (cm)	1.4	2.2	2.9	**3.4**	2.1
	d_{50} (cm)	2.4	3.6	5.0	6.6	8.4
	d_{max} = 2.6 cm for 6×6 cm^2 at 16 MeV					
	d_{max} = 2.4 cm for 10×10 cm^2 at 20 MeV					
	d_{max} = 2.7 cm for 20×20 cm^2 at 20 MeV					
	d_{50} = 8.1 cm for 6×6 cm^2 at 20 MeV					

Following installation of the TrueBeam accelerator, but before decommissioning of the Clinac 21EX (accelerators were housed in different treatment rooms, and so were in clinical use at the same time), output measurements were performed on both machines in order to compare the TrueBeam to the Clinac 21EX as part of the TrueBeam commissioning process. Outputs were measured using a Markus ionization chamber in Solid Water at 100 cm SSD. The Markus chamber was placed at depths corresponding to nominal values of d_{max} where d_{max} = 1.3, 2.0, 2.8, 2.8 and 1.5 cm for 6, 9, 12, 16 and 20 MeV electrons, respectively. Outputs were assessed for the 6×6, 10×10, 20×20 and 25×25 cm^2 applicators described above. Output uncertainty was assessed based on the variation of representative repeated measurements as well as the positioning uncertainty described in Chapter 3.

4.1.2 Results

Relative dose measurements of applicator-shaped electron fields delivered at 100 cm SSD are plotted in Figures 4.1, 4.2 and 4.3 which show depth curves, half-profiles at d_{max} and half-profiles at d_{50}, respectively. Half profiles were determined by averaging the whole profile across the central axis. A gamma comparison of Clinac 21EX and TrueBeam depth measurements find that more than 97% of data points fall within 2%/2 mm up to a 20×20 cm^2 applicator. For the 25×25 cm^2 applicator, only 81% of dose points meet the 2%/2 mm criteria at 16 MeV, while at all other energies, at least 95% of data points agree.

Similar comparisons of profile data show the same 95% pass rate at d_{max} for 6×6

and 10 × 10 cm^2 applicators at all energies except 16 MeV, but there is drop in gamma pass rates for the larger field sizes. Visually, this is corroborated by obvious differences in flatness for 20 × 20 and 25 × 25 cm^2 applicators at energies of 9 MeV and greater. At d_{50}, crossline profiles agree within 2%/2 mm for up to and including 20 × 20 cm^2 applicators at all energies, while the differences that exist in the profile shoulder at d_{max} persist at d_{50}.

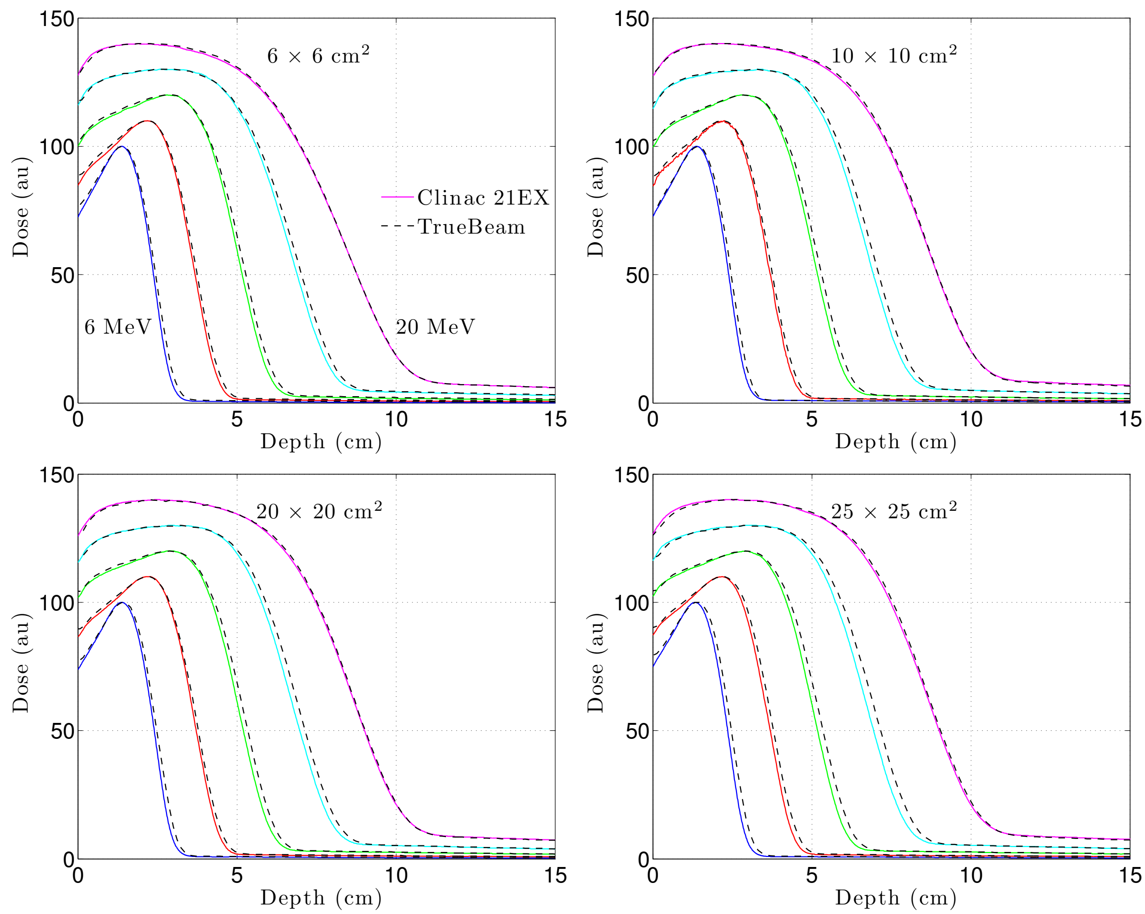

Figure 4.1: Measured depth dose curves for Clinac 21EX and TrueBeam applicator-shaped electron fields. All curves are normalized to a nominal value of d_{max} and scaled for visual clarity: 6 MeV to 100%, 9 MeV to 110%, 12 MeV to 120%, 16 MeV to 130% and 20 MeV to 140%.

Gamma pass statistics evaluated at 2%/2 mm for all data points with at least 5% of the maximum central axis dose are summarized in Table 4.3. When criteria are extended to 3%/3 mm, all depth curves fall within tolerance and all but two profiles have better than 97% pass rates. At 12 and 20 MeV, crossline profiles at d_{50} for the 25 × 25 cm^2 applicator have passing rates of at least 91% for 3%/3 mm gamma

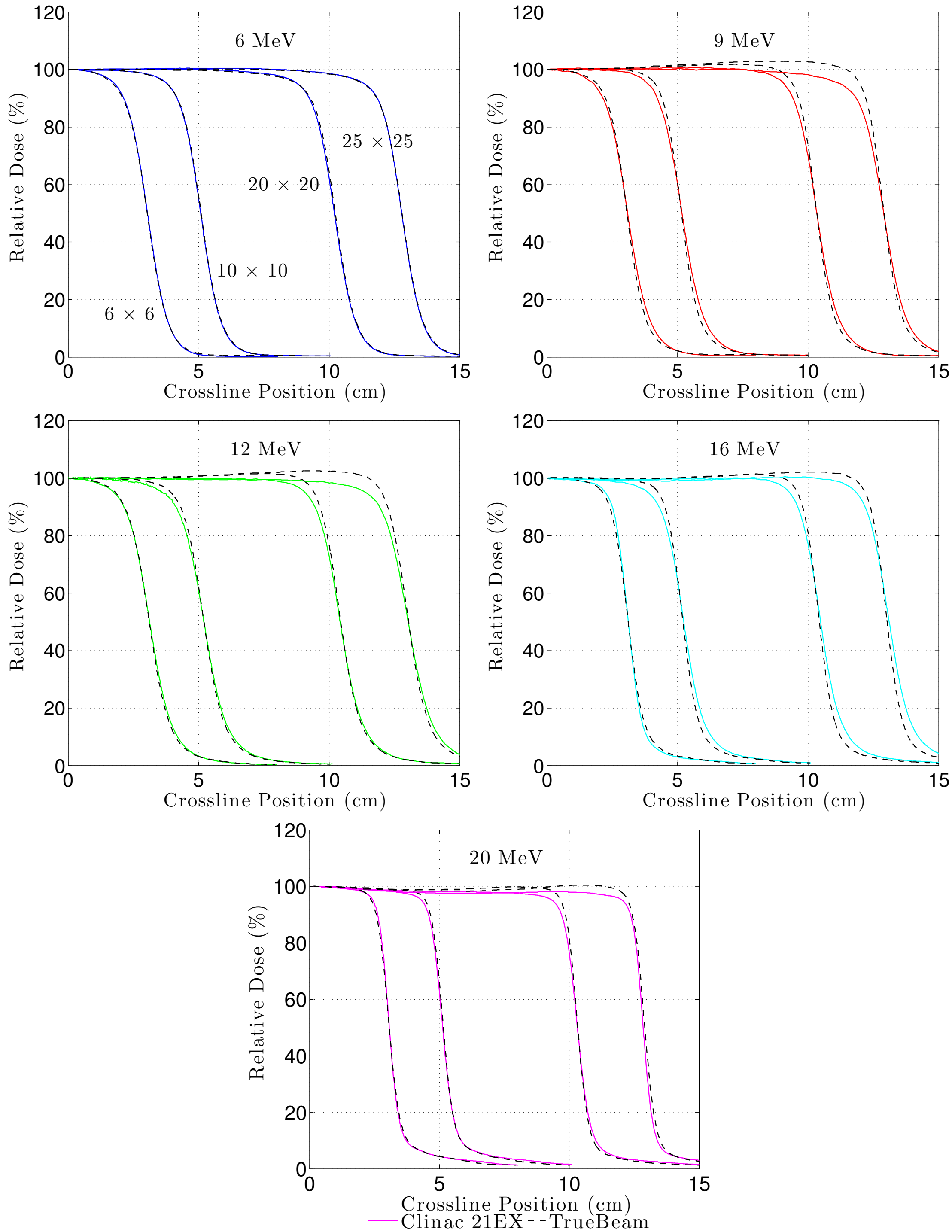

Figure 4.2: Measured crossline half-profiles at nominal values of d_{max} for Clinac 21EX and TrueBeam applicator-shaped electron fields. Curves are normalized to 100% along the central axis.

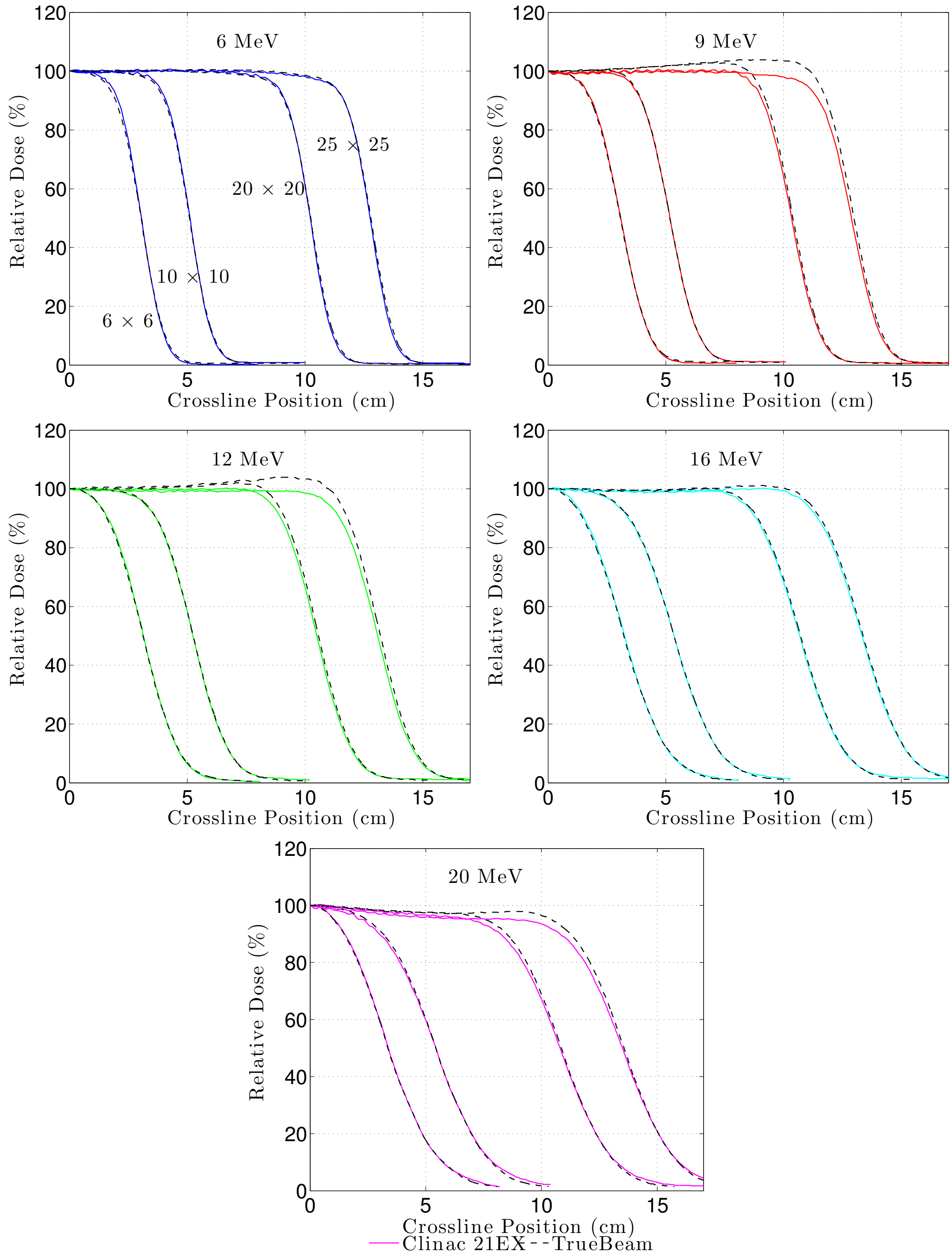

Figure 4.3: Measured crossline half-profiles at nominal values of d_{50} for Clinac 21EX and TrueBeam applicator-shaped electron fields. Curves are normalized to 100% along the central axis.

criteria.

Table 4.3: Gamma pass statistics for applicator-shaped Clinac 21EX and TrueBeam electron fields evaluated at 2%/2 mm with a 5% low-dose cut-off.

Applicator Size (cm^2)	Metric	6 MeV	9 MeV	12 MeV	16 MeV	20 MeV
6×6	PDD	97%	98%	100%	100%	100%
	$\text{crossline}_{\text{max}}$	100%	100%	100%	100%	100%
	crossline_{50}	100%	100%	100%	100%	100%
10×10	PDD	98%	98%	100%	100%	100%
	$\text{crossline}_{\text{max}}$	100%	99%	96%	83%	100%
	crossline_{50}	100%	100%	100%	100%	100%
20×20	PDD	97%	98%	100%	100%	100%
	$\text{crossline}_{\text{max}}$	100%	100%	100%	95%	84%
	crossline_{50}	100%	100%	98%	100%	100%
25×25	PDD	95%	99%	99%	81%	100%
	$\text{crossline}_{\text{max}}$	100%	63%	73%	95%	88%
	crossline_{50}	100%	69%	65%	100%	71%

Tables 4.4 and 4.5 summarize depth and profile characteristics for the fields plotted in Figures 4.1, 4.2 and 4.3 including d_{80} and d_{50}, photon contamination (D_x), FWHM, penumbra and field flatness at d_{max} and d_{50}. All parameter comparisons agree within 2% or 2 mm except for the 10×10 cm^2 field at 16 MeV whose width and flatness metrics agree within 3% and 3 mm, respectively, at d_{max}. The machines differ in field flatness by as much as 2.5% and there is an overall reduction in photon contamination for fields produced by the TrueBeam.

Relative outputs for all energies and applicator sizes described in Table 4.1 are summarized in Table 4.6, normalized to the output for a 10×10 cm^2 applicator. Outputs agree within 3% for the most part, even with the difference in jaw position, but reach as much as 4.6% for the 25×25 cm^2 applicator. Generally, the TrueBeam relative outputs are lower than the Clinac 21EX for 6×6 cm^2 fields and higher than the Clinac 21EX for fields larger than 10×10 cm^2. As well, the TrueBeam has a greater range of outputs than the Clinac 21EX for energies of 12 MeV and lower, while the Clinac 21EX has the greater range of outputs for 16 MeV and 20 MeV fields.

Table 4.4: Measured depth and crossline profile characteristics of Clinac 21EX and TrueBeam applicator-shaped 6, 9 and 12 MeV electron fields. Uncertainties in distance metrics are mostly with 1 mm except for penumbra metrics which are within 2 mm. Uncertainty in flatness is about 2%.

Applicator	6 × 6		10 × 10		20 × 20		25 × 25	
Size (cm^2)	21EX	TB	21EX	TB	21EX	TB	21EX	TB
				6 MeV				
d_{80} (cm)	2.0	2.1	2.0	2.1	2.0	2.1	2.0	2.1
d_{50} (cm)	2.4	2.5	2.4	2.5	2.4	2.5	2.4	2.5
FWHM (cm)$_{max}$	6.0	6.1	10.2	10.2	20.4	20.5	25.5	25.6
80%-20% (cm)$_{max}$	1.1	1.1	1.1	1.1	1.1	1.1	1.1	1.1
Flatness (%)$_{max}$	10.4	10.5	4.3	4.4	1.3	1.5	1.1	1.0
FWHM (cm)$_{50}$	6.1	6.1	10.2	10.2	20.4	20.5	25.5	25.6
80%-20% (cm)$_{50}$	1.3	1.4	1.3	1.3	1.3	1.4	1.4	1.4
Flatness (%)$_{50}$	12.6	13.4	5.6	5.9	1.4	1.4	1.4	1.2
D_x (%)	0.1	0.2	0.5	0.3	0.4	0.3	0.4	0.4
				9 MeV				
d_{80} (cm)	3.1	3.1	3.1	3.2	3.1	3.2	3.1	3.2
d_{50} (cm)	3.6	3.7	3.6	3.7	3.7	3.7	3.6	3.7
FWHM$_{max}$ (cm)	6.2	6.1	10.3	10.3	20.7	20.6	25.8	25.8
80%-20%$_{max}$ (cm)	1.2	1.0	1.2	1.0	1.2	1.0	1.3	1.0
Flatness$_{max}$ (%)	10.6	9.0	4.5	2.6	0.9	1.0	1.5	1.5
FWHM$_{50}$ (cm)	6.2	6.1	10.4	10.3	20.7	20.7	25.8	25.9
80%-20%$_{50}$ (cm)	1.6	1.7	1.6	1.6	1.6	1.6	1.7	1.7
Flatness$_{50}$ (%)	15.5	15.6	7.7	7.6	1.3	1.4	1.4	1.9
D_x (%)	0.4	0.4	0.9	0.4	0.6	0.5	0.8	0.6
				12 MeV				
d_{80} (cm)	4.3	4.3	4.3	4.4	4.3	4.4	4.3	4.4
d_{50} (cm)	5.0	5.1	5.0	5.1	5.0	5.2	5.0	5.2
FWHM$_{max}$ (cm)	6.2	6.2	10.4	10.4	20.8	20.9	26.0	26.0
80%-20%$_{max}$ (cm)	1.2	1.2	1.3	1.2	1.3	1.1	1.4	1.2
Flatness$_{max}$ (%)	10.8	10.6	5.9	4.1	0.9	0.8	1.2	1.3
FWHM$_{50}$ (cm)	6.3	6.2	10.5	10.5	21.0	21.1	26.2	26.3
80%-20%$_{50}$ (cm)	2.0	2.1	2.1	2.0	2.0	2.0	2.0	2.0
Flatness$_{50}$ (%)	17.7	18.1	11.1	11.0	2.1	1.8	1.2	2.0
D_x (%)	0.8	0.5	1.2	0.6	1.4	0.7	1.4	0.9

d_{80} = depth at 80% dose; d_{50} = depth at 50% dose; FWHM = full width at half maximum; 80%-20% = average width of the penumbra measured between 80% and 20% doses; D_x = dose beyond the electron range due to photon contamination; Flatness = variation over the mean within 80% of the FWHM.

4.2 MLC-defined fields

4.2.1 Methods

Additional depth, and profile scans were performed for MLC-shaped electron fields delivered at 70 cm SSD using the Clinac 21EX and TrueBeam linear accelerators.

Table 4.5: Measured depth and crossline profile characteristics of Clinac 21EX and TrueBeam applicator-shaped 16 and 20 MeV electron fields. Uncertainties in distance metrics are mostly with 1 mm except for penumbra metrics which are within 2 mm. Uncertainty in flatness is about 2%..

Applicator	6 × 6		10 × 10		20 × 20		25 × 25	
Size (cm^2)	21EX	TB	21EX	TB	21EX	TB	21EX	TB
				16 MeV				
d_{80} (cm)	5.4	5.5	5.6	5.8	5.7	5.8	5.6	5.8
d_{50} (cm)	6.6	6.7	6.6	6.7	6.7	6.8	6.6	6.8
FWHM_{max} (cm)	6.3	6.2	10.5	10.4	21.0	20.9	26.2	26.0
80%-20%$_{\text{max}}$ (cm)	0.8	0.9	1.2	0.9	1.2	0.9	1.2	0.9
$\text{Flatness}_{\text{max}}$ (%)	5.4	7.3	4.6	2.1	0.4	0.8	0.8	1.2
FWHM_{50} (cm)	6.5	6.4	10.7	10.7	21.4	21.4	26.6	26.7
80%-20%$_{50}$ (cm)	2.4	2.5	2.5	2.5	2.5	2.5	2.5	2.5
Flatness_{50} (%)	19.4	19.2	13.8	13.4	3.7	3.5	1.8	1.6
D_x (%)	1.6	1.0	2.3	1.2	2.5	1.4	2.4	1.7
				20 MeV				
d_{80} (cm)	6.4	6.5	6.9	6.9	7.0	7.0	7.0	7.0
d_{50} (cm)	8.1	8.1	8.4	8.4	8.4	8.5	8.4	8.5
FWHM_{max} (cm)	6.1	6.1	10.2	10.3	20.6	20.7	25.7	25.8
80%-20%$_{\text{max}}$ (cm)	0.6	0.7	0.7	0.7	0.8	0.7	0.6	0.6
$\text{Flatness}_{\text{max}}$ (%)	2.8	3.5	1.8	1.2	1.3	0.7	1.3	1.1
FWHM_{50} (cm)	6.8	6.7	10.9	10.9	21.6	21.7	27.0	27.1
80%-20%$_{50}$ (cm)	2.7	2.8	3.1	3.0	3.2	3.0	3.1	2.9
Flatness_{50} (%)	19.9	19.9	16.3	15.5	7.5	6.5	5.6	3.8
D_x (%)	3.0	1.8	4.0	2.1	4.4	2.4	4.0	3.0

d_{80} = depth at 80% dose; d_{50} = depth at 50% dose; FWHM = full width at half maximum; 80%-20% = average width of the penumbra measured between 80% and 20% doses; D_x = dose beyond the electron range due to photon contamination; Flatness = variation over the mean within 80% of the FWHM.

Measurements were performed for 5 × 5 and 20 × 20 cm^2 MLC-shaped fields of 6, 12 and 20 MeV electrons using the EFD^{3G} scanning electron field diode and CC13 ion chamber reference in the large water tank. Jaws were set to 6 × 6 and 21 × 21 cm^2 for 5 × 5 and 20 × 20 cm^2 MLC-settings, respectively, with all field sizes defined at isocenter. Profiles were acquired in both inline and crossline directions at nominal values of d_{max} and d_{50} where d_{max} = 1.4, 2.7, and 2.2 cm and d_{50} = 2.4, 5.1 and 8.3 cm for 6, 12 and 20 MeV, respectively. Data for the Clinac 21EX were acquired at the end of the accelerators clinical life while TrueBeam data were acquired within a year of installation. Data were acquired and processed using OmniPro-Accept v7.4.

Output factors as a function of MLC-size were also measured for both machines using a Markus ionization chamber in Solid Water at 70 cm SSD. Outputs for 6 MeV were measured at 1.5 cm depth while 12 and 20 MeV outputs were measured

Table 4.6: Measured electron outputs for applicator-shaped fields produced by the Clinac 21EX and TrueBeam linear accelerators. Output uncertainty is on the order of 1%.

Energy (MeV)	Machine	Applicator Size cm^2			
		6×6	10×10	20×20	25×25
6	Clinac 21EX	0.967	1.000	1.015	1.012
	TrueBeam	0.940	1.000	1.046	1.059
9	Clinac 21EX	0.985	1.000	0.990	0.966
	TrueBeam	0.981	1.000	1.012	1.008
12	Clinac 21EX	0.982	1.000	0.978	0.949
	TrueBeam	0.950	1.000	1.007	0.992
16	Clinac 21EX	0.989	1.000	0.973	0.946
	TrueBeam	0.976	1.000	0.988	0.975
20	Clinac 21EX	1.004	1.000	0.957	0.923
	TrueBeam	1.002	1.000	0.966	0.952

at 2.5 cm depth. Jaws were set to 40×40 cm^2 for all fields. Uncertainty in output measurements was assessed from the variation in repeated measurements as well as the positioning uncertainty described in Chapter 3.

4.2.2 Results

Relative dose measurements of MLC-shaped electron fields delivered at 70 cm SSD are plotted in Figures 4.4, 4.5 and 4.6 which show depth dose curves, half-profiles at d_{max} and half-profiles at d_{50}, respectively. Half profiles were determined by averaging the whole profile across the central axis. Measurements are shown for 6, 12, and 20 MeV electrons with 5×5 and 20×20 cm^2 MLC-shaped apertures and jaws set to 6×6 and 21×21 cm^2, respectively.

Gamma-pass statistics evaluated at 2%/2 mm are summarized in Table 4.7. As in the applicator-shaped field data, differences in depth measurements fall within 2% and 2 mm except at 20 MeV for the 5×5 cm^2 field where only 93% of data points fall within 2%/2 mm. Profile differences for 5×5 cm^2 apertures fall within 2%/2 mm for all energies in both directions and depths. At 20×20 cm^2 however, differences are

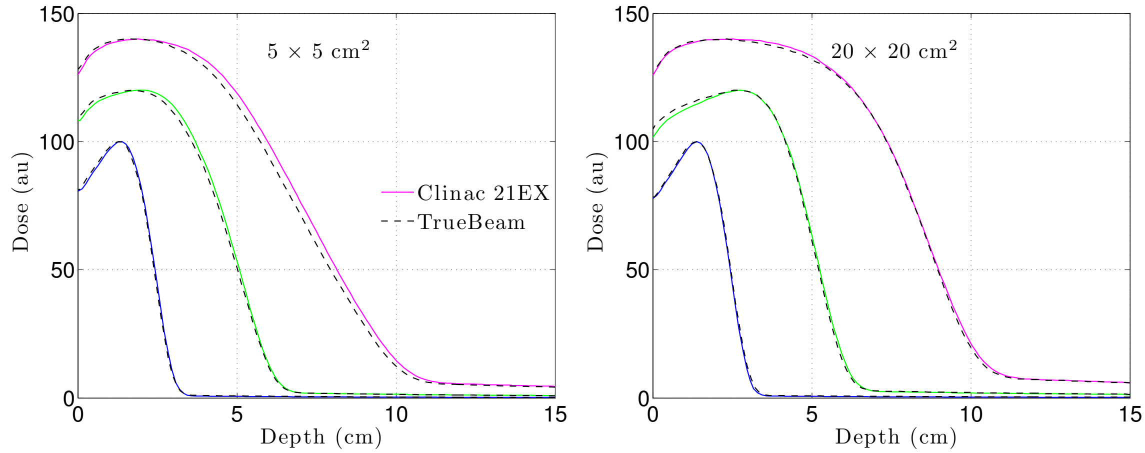

Figure 4.4: Measured depth dose curves for Clinac 21EX and TrueBeam MLC-shaped electron fields. All curves are normalized to nominal values of d_{max} and scaled for visual clarity: 6 MeV to 100%, 12 MeV to 120% and 20 MeV to 140%.

more pronounced in the profile shoulders and penumbras. By extending comparison criteria to 3%/3 mm, all profiles agree except for the 20 MeV inline profile at d_{max} and 6 MeV inline profile at d_{50} which have 96% and 86% gamma-pass rates, respectively.

Table 4.7: Gamma pass statistics for MLC-shaped Clinac 21EX and TrueBeam electron fields evaluated at 2%/2 mm with a 5% low-dose cut-off.

MLC Aperture Size (cm^2)	Metric	6 MeV	12 MeV	20 MeV
5 × 5	PDD	100%	100%	93%
	crossline_{max}	100%	100%	100%
	inline_{max}	100%	100%	100%
	crossline_{50}	100%	100%	100%
	inline_{50}	100%	100%	100%
20 × 20	PDD	100%	99%	100%
	crossline_{max}	91%	84%	80%
	inline_{max}	80%	92%	87%
	crossline_{50}	84%	100%	99%
	inline_{50}	75%	100%	100%

Table 4.8 summarizes depth and profile characteristics for the MLC-shaped electron fields plotted in Figures 4.4, 4.5 and 4.6. For the 5 × 5 cm^2 field, all but one parameter agree within 2% or 2 mm, and the outlier, d_{80} at 20 MeV, agrees within 3 mm. At 20 × 20 cm^2, all tabulated parameters agree within 2% or 2 mm with the

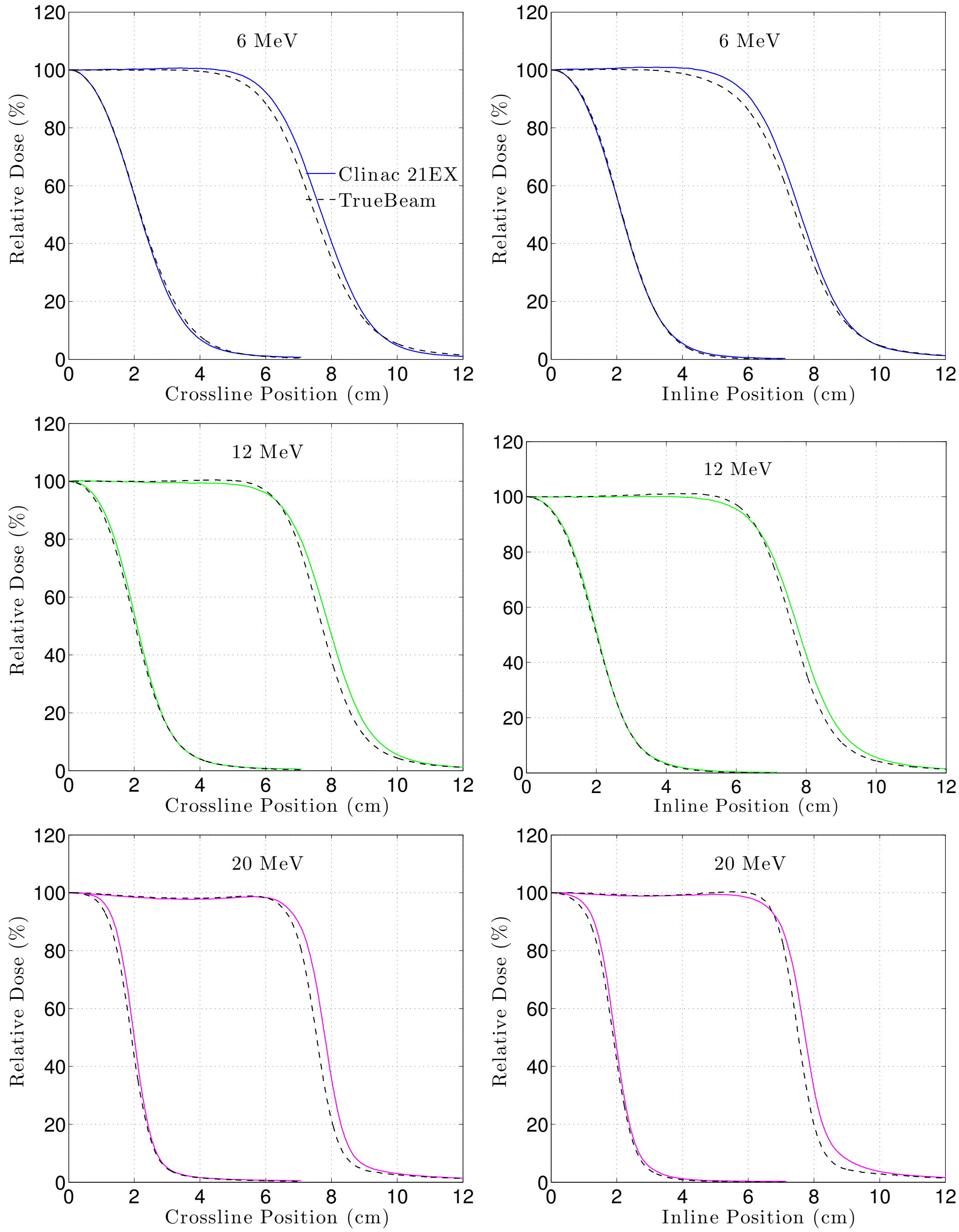

Figure 4.5: Measured crossline (left) and inline (right) half-profiles at nominal values of d_{max} for Clinac 21EX and TrueBeam MLC-shaped electron fields. All curves are normalized to 100% along the central axis.

exception of FWHM at all energies, which differ by as much as 5 mm. Note, however, that the difference in width represents twice the distance to agreement, and therefore

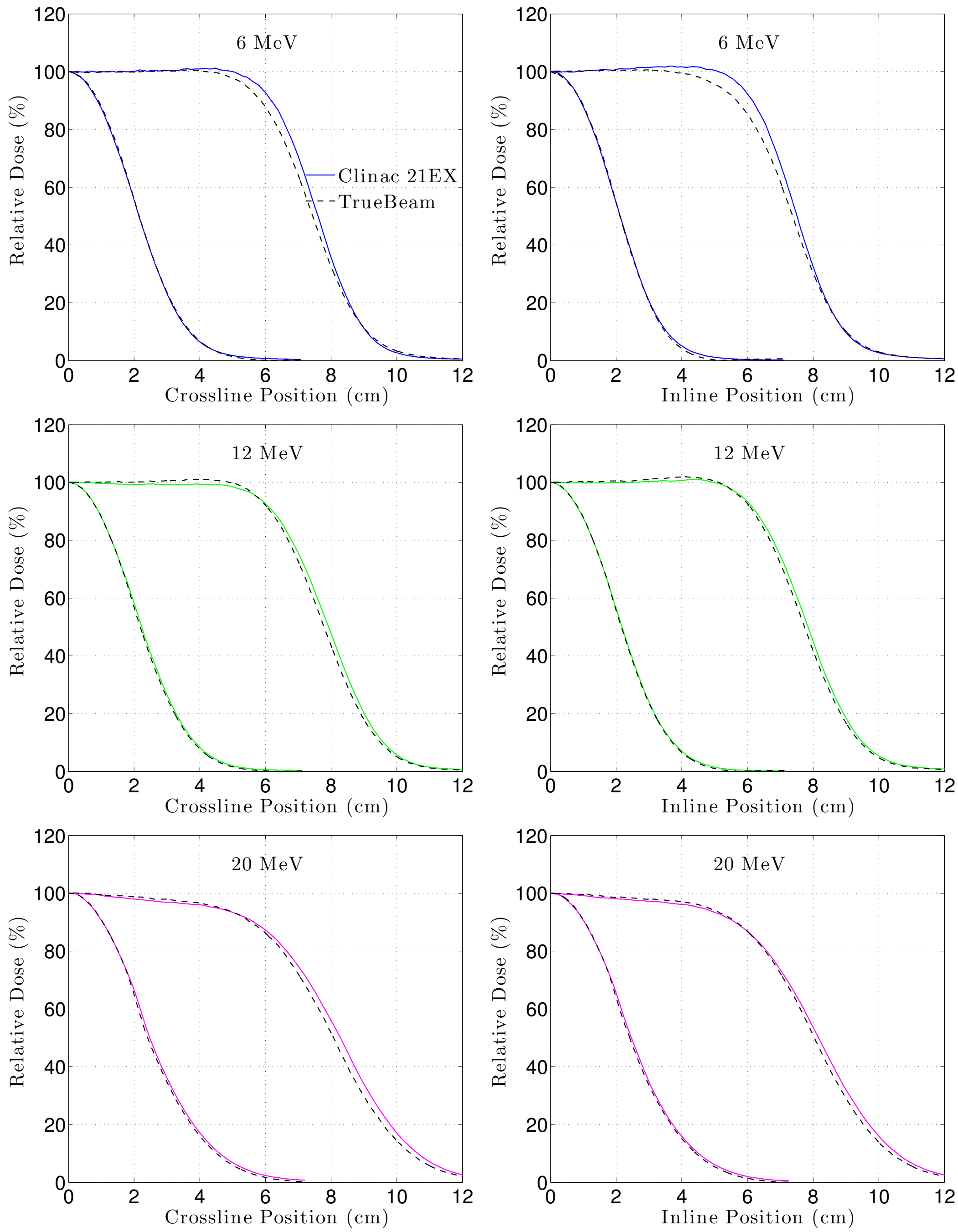

Figure 4.6: Measured crossline (left) and inline (right) half-profiles at nominal values of d_{50} for Clinac 21EX and TrueBeam MLC-shaped electron fields. All curves are normalized to 100% along the central axis.

the distance to agreement less than 3 mm. Also note that the FWHM of inline profiles at d_{50} agree within 2 mm at all energies. Compared to applicator-shaped fields, MLC field definition produces poorer field flatness, however, the difference in the flatness between machines is far less pronounced for MLC-shaped field comparison, within 1.7% compared to 2.5% for the applicator-shaped field comparison.

Table 4.9 summarizes output factors for 5×5 and 20×20 cm^2 MLC-shaped electron fields relative to a 10×10 cm^2 MLC-shaped field at 70 cm SSD with jaws at 40×40 cm^2. At 20 MeV, output factors agree within 1.6% while at 12 MeV output factors agree within 3.4%. At 6 MeV, the 20×20 cm^2 output factor agrees within 3.2% while at 5×5 cm^2 the difference is 9.1%. In this configuration, the relative output range is greater for the TrueBeam than for the Clinac 21EX at all three energies.

4.3 Film measurements of MLC-defined fields

4.3.1 Methods

Film measurements of the MLC-aperture shown in Figure 4.7 were performed using Gafchromic EBT2 (Clinac 21EX) and EBT3 (TrueBeam) radio-chromic film, both described in Section 3.1.3. Different film types were used to perform measurements on each machine due to a clinical transition from EBT2 to EBT3 during the timeframe of the measurements. Film was processed as outlined in Section 3.1.3, and uncertainties were assessed for the TrueBeam data by taking the standard deviation of multiple films exposed to the same field at each dose point.

The MLC aperture used was based on a 20×20 cm^2 open field with five closed leaf pairs. Jaws were set to 40×40 cm^2. Fields were delivered at 70 cm SSD with film placed between slabs of Solid Water orthogonal to the beam axis at depths of 1.5 cm and 2.0 cm for 6 and 20 MeV electrons, respectively.

4.3.2 Results

Figure 4.8 shows crossline and inline profiles taken from film measurements of the field shown in Figure 4.7, delivered by the Clinac 21EX and TrueBeam. Profiles have been extracted 3.5 cm from the central axis in both the crossline and inline directions, (i) and (ii) in Figure 4.7, respectively, and normalized at their intersection point (x = 3.5 cm, y = 3.5 cm).

At 6 MeV, the mean standard deviations away from the penumbra for the TrueBeam data are 3.0% and 4.4% for crossline and inline profiles, respectively. The

Table 4.8: Measured depth and profile characteristics of Clinac 21EX and TrueBeam MLC-shaped electron fields. Where profile and penumbra widths are difference in the crossline and inline directions, both values are given in the format crossline/inline. Uncertainties in distance metrics are mostly with 1 mm except for penumbra metrics which are within 2 mm. Uncertainty in flatness is about 2%.

MLC Field	5×5		20×20	
Size (cm^2)	21EX	TB	21EX	TB
		6 MeV		
d_{80} (cm)	2.0	2.0	2.0	2.1
d_{50} (cm)	2.4	2.4	2.4	2.5
D_x (%)	0.1	0.2	0.1	0.1
Flatness_{max} (%)	20.2	20.3	5.5	6.2
FWHM_{max} (cm)	4.3	4.4/4.3	15.4/15.2	15.0/14.9
80%-$20\%_{max}$ (cm)	1.8 /1.7	1.9/1.7	2.1 /2.0	2.2
FWHM_{50} (cm)	4.3/4.2	4.3/4.2	15.2/14.9	14.8/14.7
80%-$20\%_{50}$ (cm)	1.9/1.7	1.9/1.7	1.9/2.0	2.1/2.2
		12 MeV		
d_{80} (cm)	3.8	3.7	4.3	4.3
d_{50} (cm)	4.9	4.8	5.1	5.0
D_x (%)	0.2	0.2	0.4	0.3
Flatness_{max} (%)	17.9	18.5	3.6	2.7
FWHM_{max} (cm)	4.2 /4.1	4.1 /4.0	15.8/15.6	15.4/15.3
80%-$20\%_{max}$ (cm)	1.4	1.5/1.4	1.8	1.7/1.6
FWHM_{50} (cm)	4.5/4.4	4.4/4.3	15.8/15.6	15.5/15.4
80%-$20\%_{50}$ (cm)	2.0/1.9	1.9	2.2	2.2
		20 MeV		
d_{80} (cm)	5.4	5.1	6.8	6.8
d_{50} (cm)	7.3	7.1	8.4	8.4
D_x (%)	0.9	1.3	1.8	0.9
Flatness_{max} (%)	11.1	12.8	1.2	0.9
FWHM_{max} (cm)	4.0 /3.9	3.8	15.6/15.5	15.1
80%-$20\%_{max}$ (cm)	0.8/0.9	0.9/1.0	1.0	0.9
FWHM_{50} (cm)	4.9	4.8	16.6/16.3	16.1
80%-$20\%_{50}$ (cm)	2.3/2.2	2.2	3.2/3.1	3.1/3.0

d_{80} = depth at 80% dose; d_{50} = depth at 50% dose;
FWHM = full width at half maximum; 80%-20% = average width of the penumbra measured between 80% and 20% doses;
D_x = dose beyond the electron range due to photon contamination; Flatness = variation over the mean within 80% of the FWHM.

Table 4.9: Measured electron outputs for MLC-shaped fields produced by the Clinac 21EX and TrueBeam linear accelerators. Jaws were set to 40×40 cm^2. Output uncertainty is on the order of 1%.

Energy (MeV)	Machine	MLC Field Size cm^2		
		5×5	10×10	20×20
6	Clinac 21EX	0.759	1.000	1.066
	TrueBeam	0.668	1.000	1.098
12	Clinac 21EX	0.915	1.000	1.025
	TrueBeam	0.882	1.000	1.038
20	Clinac 21EX	0.977	1.000	1.020
	TrueBeam	0.961	1.000	1.027

maximum standard deviations are 5.0% and 6.0% for the crossline and inline profiles, respectively. At 20 MeV, the mean standard deviations away from the penumbra for the TrueBeam data are 2.7% and 5.2% for crossline and inline profiles, respectively. The maximum standard deviations are 4.5% and 9.7% for the crossline and inline profiles, respectively. Comparing the Clinac 21EX and TrueBeam data, profiles through the open portion of the aperture agree within one standard deviation of measurement as described above. The modulated portions of the inline profiles show differences of up to 10% between the Clinac 21EX and TrueBeam, but these differences fall within 2 standard deviations of the measurement.

4.4 Discussion

Despite the changes made to its internal design compared to previous generations of Varian linear accelerators, electron fields generated by the TrueBeam have depth and profile characteristics that fall within 3%/3 mm, for the most part, compared to those generated by the Clinac 21EX, whether delivered using conventional electron applicators at 100 cm SSD or with the photon MLC at 70 cm SSD.

At 6 MeV, applicator data are within 2%/2 mm for more than 95% of data points. At electron energies of 9, 12, 16, and 20 MeV, differences in the applicator depth data fall well within 2%/2 mm for the most part, and compared to the Clinac 21EX, the TrueBeam generates flatter applicator-shaped fields with reduced photon contamination. Differences in profile data fall within 3%/3 mm. Because commissioning data

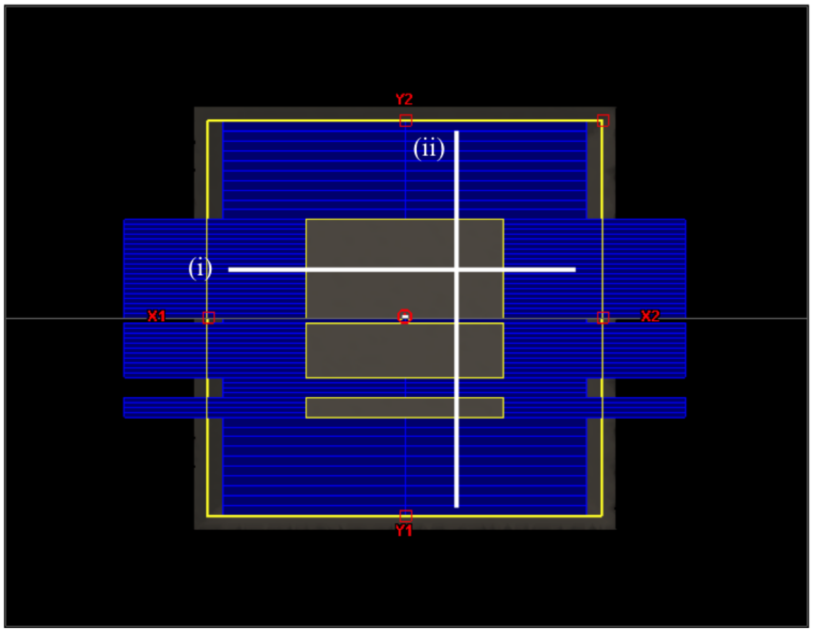

Figure 4.7: MLC-defined electron aperture used to expose radio-chromic film. The field is based on a 20×20 cm^2 open field with five closed leaf pairs. Crossline and inline profiles were assessed along the lines (i) and (ii), 3.5 cm from the central axis, as indicated on the aperture.

were acquired by two sets of physicists at different times, the depths at which some profiles were acquired on each machine differ by as much as 5 mm, but mostly within 1 mm. Based on beam divergence alone, the FWHM of a 25×25 cm^2 field delivered at 100 cm SSD changes less than 1 mm with a change in depth of 5 mm, so this is expected to have a small effect on the comparisons presented.

Differences of as much as 8% occur in the shoulder region at larger applicator sizes. Beyer [13] attributed similar differences in photon profile shoulder heights to changes in the incident electron source width, while Weinberg et al. [112] used Monte Carlo simulations to show the same relationship for electrons on a Clinac 2100C, demonstrating a more narrow source width to produce more peaked profile shoulders. Both Weinberg et al. and Huang et al.[49] investigated the role of electron source divergence on profile shape using Monte Carlo simulations, and both studies found a non-divergent source to produce peaked profile shoulders. The profile differences described in this chapter, therefore, can be attributed, in part, to differences in the electron source, in addition to changes in the scattering foil design.

For the three energies investigated using MLC-shaped fields, differences between the Clinac 21EX and TrueBeam are more pronounced than in applicator-based mea-

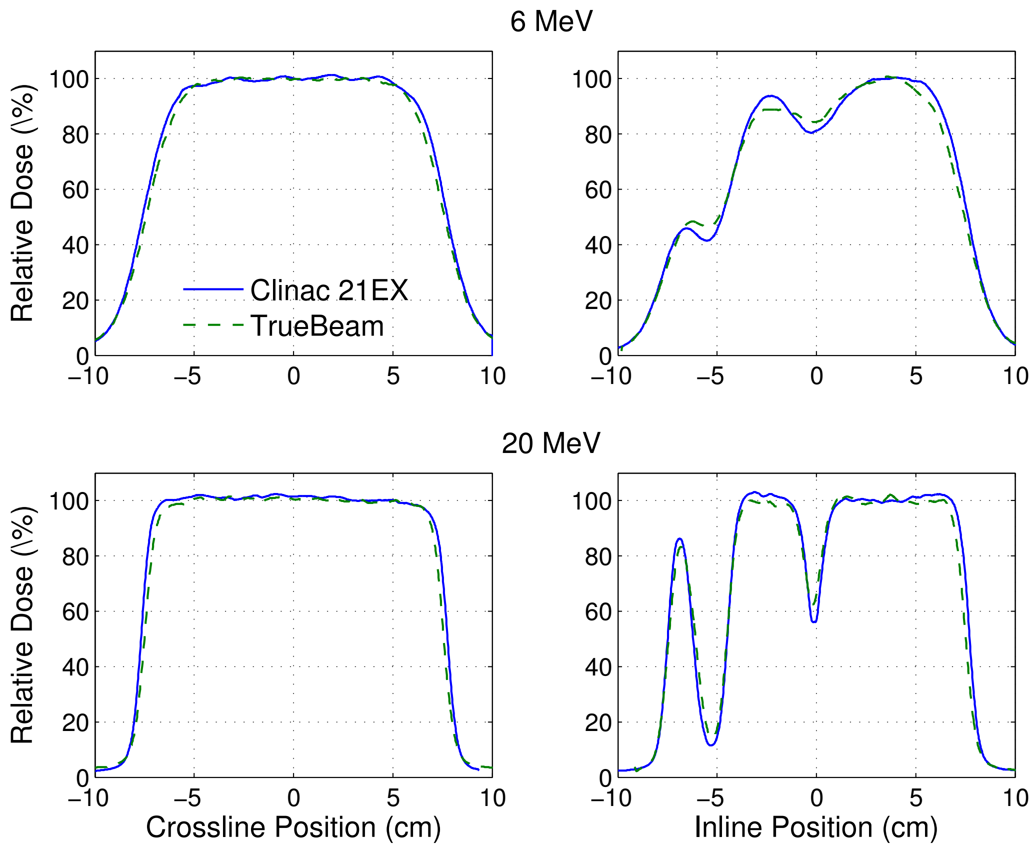

Figure 4.8: Film measurements of a 20 $\times$ 20 cm^2 MLC-shaped electron field with closed leaf pairs delivered by a Clinac 21EX and a TrueBeam at 6 MeV (top) and 20 MeV (bottom). Profiles are extracted 3.5 cm away from the central axis as illustrated in Figure 4.7.

surements. Differences in depth dose data fall, largely, within 2%/2 mm, while differences in profile data fall within 3%/3 mm. The differences seen in the profile shoulders of the largest applicator-shaped field are larger than those seen in the profile shoulders of the largest MLC-shaped fields, but note that the largest MLC-shaped aperture investigated was 20 $\times$ 20 cm^2, while the largest applicator-shaped aperture was 25 $\times$ 25 cm^2.

Film measured profiles acquired with jaws set to 40 $\times$ 40 cm^2 (Figure 4.8) agree better in width and penumbra than diode measured profiles acquired with the jaws set 1 cm beyond the MLC field (Figure 4.5). Differences in the accelerator head design above the jaws resulting in changes in scatter would be most evident in measured profiles when the jaws are close enough to the field edge to reflect the out-of-field scatter component back into the field. The role of jaws in MLC-shaped electron fields will be investigated further in subsequent chapters.

Film measured profiles through the open portions of the field show differences within 2% away from the penumbra, and all differences fall within 2 standard deviations of measurement. Good alignment in the modulated regions of the inline profiles is indicative of good MLC alignment between the machines perpendicular to the direction of leaf motion.

Applicator-based output factors agree within 3%, for the most part, despite changes in the electron source, jaw setting and design of the scattering foils. Output factors measured for MLC-shaped fields agree within 1.6% for 20 MeV, and within 3.4% for 12 MeV, but differ by as much as 9.1% at 6 MeV. Recalling that low energy electrons will be most sensitive to any change in the incident electron source or scattering foil design, it follows that the most dramatic changes in output would occur for 6 MeV. TrueBeam output dependencies on field size will be investigated further in Chapters 5 and 6.

In conclusion, the electron PDDs and profiles produced by the Clinac 21EX and TrueBeam linear accelerators fall within 3%/3 mm, for the most part when shaped by applicators or MLC. Given this agreement, it is hypothesized that a complete Monte Carlo accelerator model of a Clinac 21EX can be modified to simulate MLC-shaped electron fields generated by the TrueBeam to within 3%/3 mm. The validity of this hypothesis and associated challenges will be explored further in Chapter 5.

Chapter 5

Results & Discussion II: Complete accelerator models for Monte Carlo simulations of MLC-shaped electron fields

In Chapter 4 the differences between electron fields produced by the Clinac 21EX and TrueBeam linear accelerators were shown to be within 3%/3 mm, for the most part. Informed by this comparison, the current chapter presents complete Monte Carlo accelerator models of the Clinac 21EX and modification of these models in order to simulate electron fields that are dosimetrically equivalent to those produced by the TrueBeam. These accelerator models are benchmarked against measurement for electron fields characteristic of MERT and MPERT approaches, namely, shaped with the photon MLC and delivered at 70 cm SSD.

Complete accelerator models are the focus of this work, but they are not the only method for Monte Carlo simulations of radiation field production. Another approach to beam modelling, presented by Ma et al. [75], is the use of a multi-source model in which particles originating from different parts of the accelerator can be modelled as originating in various sub-sources. This approach was implemented by Jiang et al. [51] resulting in a four-source model for a Varian Clinac 2100C that could be tuned and applied to multiple machines of the same design and agreed with complete accelerator simulations within 2%/2 mm. Papaconstadopoulus and Seuntjens [84] presented a Clinac 21EX source model that separated the beam into a primary source and multiple scattered sources, which agreed with full simulations within 3%. Most recently, Henzen et al. [45] presented a dual electron source model for Varian TrueBeam and Clinac 23EX linear accelerators that utilized a primary foil source and secondary jaw source for fixed jaw settings, which agreed with measurement within 3%/3 mm.

While multi-source models can have faster calculation times, their efficiencies are bought through approximations. Furthermore, the accuracy of these approaches is generally evaluated against complete accelerator simulations. Klein et al. [64], Al-Yahya et al. [2], and Salguero et al. [96] used complete accelerator models to simulate Varian Trilogy, Clinac 2100EX, and Siemens Primus electron sources, respectively, with overall agreements within 3%/3 mm compared to measurement. However, a complete accelerator model of the TrueBeam for absolute dose calculations has been elusive, due to the proprietary nature of its internal geometry.

Rodriguez et al. [91] published a PRIMO-based, complete geometric model of the TrueBeam's flattening filter free photon fields called "FakeBeam" that produced relative PDDs that agreed within 1%/1 mm of measurement for 98% of data points and profiles that agreed within 1%/1 mm of measurement for 96% of data points. In that work, Varian confirmed with the authors that there is a large similarity between the TrueBeam and Clinac series accelerator head assemblies from the jaws down, and from the Monte Carlo data packages subsequently published by Varian, it is clear that they are the same. The geometry used in "FakeBeam" was based on the Clinac 2100 linear accelerator, with modifications made upstream of the jaws. Because the schematics of the ion chamber were not known explicitly, the authors did not perform absolute dose calculations. They suggested, however, that the technique used by Zavgorodni et al. [116] could be used to calculate absolute dose with close to 1% accuracy compared to measurement. This is explored further in Chapter 7.

In Section 5.1, an electron model of the Clinac 21EX based on the manufacturer's specifications is compared against measurement. In Section 5.2, the Clinac 21EX model is modified to simulate MLC-shaped electron fields produced by the TrueBeam and benchmarked against measurement.

5.1 Complete Monte Carlo model of the Clinac 21EX

5.1.1 Methods

Models and simulations

The internal geometric specifications of the Clinac 21EX linear accelerator are summarized in Varian's 2008 Monte Carlo High Energy Accelerator Data Package, and the electron beam models presented in this work are based on photon beam models described previously [115] which were built to these specifications. The primary collimator, energy-specific scattering foils, ion chamber, mirror, secondary collimating jaws and MLC were modelled in BEAMnrc using the CONS3R, CONESTAK, CHAMBER, MIRROR, JAWS and DYNVMLC component modules. A block representation of these component modules and their positional order in the accelerator head is shown in Figure 5.1. The DYNVMLC component module of Varian's Millenium-120 MLC was modified by the Vancouver Island Centre Monte Carlo group to achieve the best agreement between simulation and measurement for static and dynamic MLC-shaped photon fields. The source was modelled as a parallel elliptical beam with a symmetric Gaussian distribution (ISOURC = 19) and mono-energetic incident electrons.

Monte Carlo simulations were performed using BEAMnrc and DOSXYZnrc as implemented in the Vancouver Island Monte Carlo system (VIMC) described in Section 3.2.1. Photon and electron cut-off energies were set to `AP` = `PCUT` = 0.01 MeV and `AE` = `ECUT` = 0.7 MeV, respectively, and `ESAVE` was set to 1.0 MeV, so that electrons below 1.0 MeV were assumed to deposit the remainder of their energy locally if they would have less than 0.7 MeV (`ECUT`) upon exiting the region they currently occupied. Dose was scored in a $30 \times 30 \times 30$ cm^3 water phantom generated in VIMC by using the user code `ctcreate` to convert a CT Dicom image set and structures into an EGSnrc formatted phantom file. The CT Dicom image set was created in Varian's Eclipse treatment planning software where a cubic water box assigned to have water properties was defined within an empty 3D image. The image and water box structure were exported for use in VIMC. The calculation voxel size was set to $0.2 \times 0.2 \times 0.2$ cm^2. Approximately 10^9 particles were simulated to achieve in-field statistical uncertainties less than 1%.

To obtain the best match between simulation and measurement, the incident

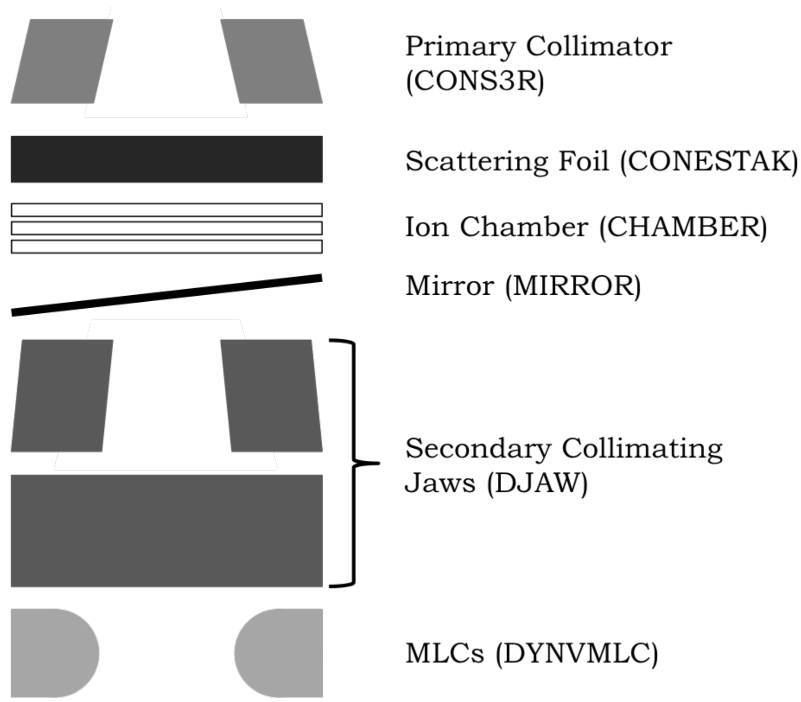

Figure 5.1: Block representation of the component modules used to model the Clinac 21EX and TrueBeam linear accelerators.

electron energy, source width and foil parameters for each model were optimized using a manual iterative method. In order to assess model performance, the depth and width parameters tabulated in Table 5.2 were assessed for the simulated data and compared against measurement with the goal of minimizing the differences in these parameter sets. Incident energy was modified to match depth parameters while source width and foil parameters were modified to match field width and penumbra parameters. Modification of the foil parameters impacted depth dose characteristics of the beam, so the incident electron source energy had to be updated to account for this effect following changes to the scattering foil.

Measurements

The same diode measurements of MLC-shaped fields delivered by the Clinac 21EX in water described and presented in Section 4.2 are used here for benchmarking. Relative depth and profile measurements for 5×5, 10×10 and 20×20 cm^2 MLC-apertures (defined at isocenter) with secondary collimating jaws set to 6×6, 11×11 and 21×21 cm^2, respectively were acquired for 6, 12, and 20 MeV electrons. Profiles are in the crossline and inline directions at nominal values of d_{max} and d_{50} where $d_{max} = 1.4$, 2.7, and 2.2 cm and $d_{50} = 2.4$, 5.1 and 8.3 cm for 6, 12 and 20 MeV electrons, respectively. Further details are summarized in Sections 3.1.2 and 4.2.1.

The same relative output measurements used in Section 4.2 are used here for comparison, however, outputs were not considered during the model tuning process. Outputs were compared for 5×5, 10×10 and 20×20 cm^2 MLC-shaped apertures at 70 cm SSD with jaws set to 40×40 cm^2 for 6, 12 and 20 MeV electrons. Outputs for 6 MeV fields were measured at 1.5 cm depth in Solid Water while outputs for 12 and 20 MeV were measured at 2.5 cm. Uncertainty in output measurements was assessed from the variation in repeated measurements as well as the positioning uncertainty described in Chapter 3.

5.1.2 Results

The source parameters that achieved the best agreement with measured depth and profile curves for each of the Clinac 21EX electron energies simulated are summarized in Table 5.1. Foil dimensions are given relative to the nominal values specified in the Monte Carlo data package.

Table 5.1: Model parameters for complete MC modelling of Clinac 21EX electrons.

Nominal Energy (MeV)	Incident Energy (MeV)	Source Width (cm)	Primary Foil Thickness (relative to nominal)	Secondary Foil Width (relative to nominal)
6	6.73	0.37	0.59	1.00
12	13.40	0.33	1.00	1.10
20	22.14	0.28	1.00	1.10

Figure 5.2 compares diode measurements of Clinac 21EX electron fields with Monte Carlo simulations performed using the parameters presented in Table 5.1. Both PDDs and dose profiles are plotted for 5×5, 10×10 and 20×20 cm^2 MLC-apertures with jaws set to 6×6, 11×11 and 21×21 cm^2, respectively. The central beam axis falls between data points in the Monte Carlo data sets, therefore, voxels adjacent to the beam axis were averaged to interpolate each dose point in the plane of the central axis. Simulated PDDs agree with measurement within 1%/2 mm, while profiles require that the gamma criteria be extended to 3%/3 mm in order for all points to pass. Disagreement is obvious in the penumbra tails where Monte Carlo consistently underestimates the measured dose. Monte Carlo also underestimates measurement in the profile shoulders at 6 and 12 MeV, especially at d_{50}.

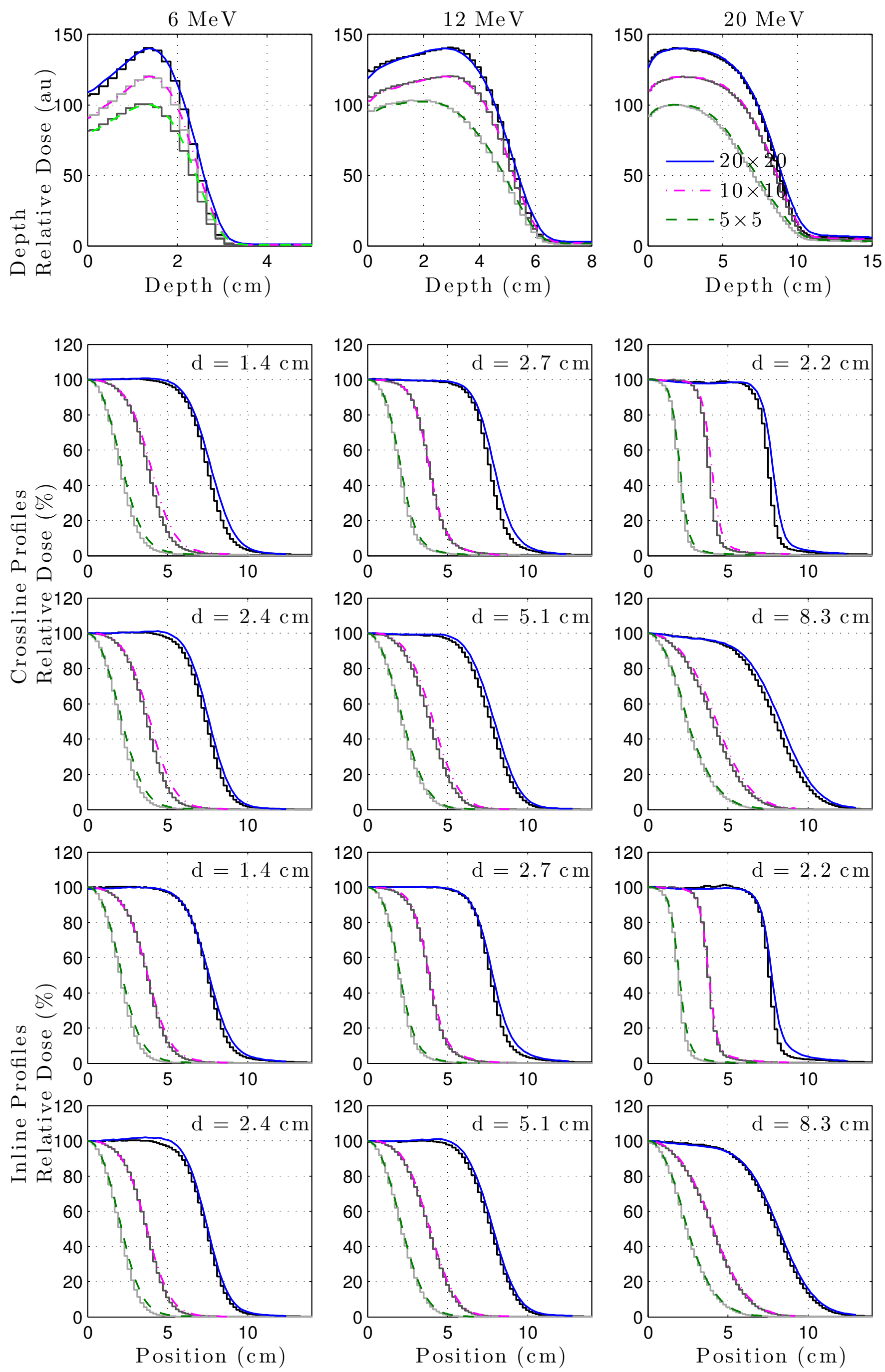

Figure 5.2: Relative measured (coloured lines) and Monte Carlo simulated (histogram) PDDs and profiles for Clinac 21EX MLC-shaped electron fields delivered at 70 cm SSD with 6, 12 and 20 MeV electrons. Jaws are set to the MLC aperture + 1 cm. PDDs are scaled for visual clarity: 5×5 cm^2 to 100% (green), 10×10 cm^2 to 120% (magenta) and 20×20 cm^2 to 140% (blue).

Table 5.2: Measured and simulated dose parameters for Clinac 21EX MLC-shaped electron fields delivered at 70 cm SSD with 6, 12 and 20 MeV electrons. Width metrics are given in crossline (cross) and inline (in) orientations. Uncertainty in measured distance metrics is mostly with 1 mm except penumbra which are within 2 mm. Uncertainty in simulated distance metrics is 1 mm.

MLC (cm^2)	5×5		10×10		20×20	
	Diode	MC	Diode	MC	Diode	MC
			6 MeV			
d_{90} (cm)	1.8	1.8	1.9	1.8	1.8	1.8
d_{80} (cm)	2.0	2.0	2.0	2.0	2.0	2.0
d_{50} (cm)	2.4	2.3	2.4	2.4	2.4	2.4
d_{20} (cm)	2.8	2.7	2.8	2.7	2.8	2.7
D_x (%)	0.3	0.2	0.2	0.2	0.3	0.2
$FWHM_{cross}$(cm)	4.3	4.1	7.9	7.5	15.4	15.0
80-20$\%_{cross}$ (cm)	1.8	1.6	2.1	1.8	2.1	1.8
$FWHM_{in}$ (cm)	4.3	4.1	7.5	7.5	15.2	15.0
80-20$\%_{in}$ (cm)	1.7	1.5	2.0	1.8	2.0	1.8
			12 MeV			
d_{90} (cm)	3.5	3.4	3.9	4.0	3.9	4.0
d_{80} (cm)	3.9	3.9	4.3	4.3	4.3	4.3
d_{50} (cm)	4.9	4.8	5.1	5.0	5.1	5.0
d_{20} (cm)	5.7	5.6	5.8	5.7	5.8	5.7
D_x (%)	0.8	0.8	0.9	0.8	1.1	1.0
$FWHM_{cross}$(cm)	4.2	4.0	7.7	7.7	15.8	15.8
80-20$\%_{cross}$ (cm)	1.4	1.3	1.5	1.5	1.8	1.6
$FWHM_{in}$ (cm)	4.1	3.9	7.7	7.7	15.6	15.4
80-20$\%_{in}$ (cm)	1.4	1.3	1.5	1.5	1.8	1.5
			20 MeV			
d_{90} (cm)	4.6	4.3	5.8	5.7	5.9	5.7
d_{80} (cm)	5.4	5.2	6.7	6.7	6.8	6.7
d_{50} (cm)	7.3	7.1	8.3	8.2	8.4	8.3
d_{20} (cm)	9.2	9.0	9.7	9.5	9.7	9.5
D_x (%)	3.2	3.0	3.7	3.7	4.3	3.7
$FWHM_{cross}$(cm)	4.0	3.8	8.0	7.6	15.6	15.1
80-20$\%_{cross}$ (cm)	0.8	0.7	0.9	0.7	1.0	0.8
$FWHM_{in}$ (cm)	3.9	3.8	7.6	7.6	15.5	15.2
80-20$\%_{in}$ (cm)	0.9	0.7	0.8	0.8	1.0	0.8

Table 5.2 summarizes depth dose and profile metrics for the curves plotted in Figure 5.2, including d_{90}, d_{80}, d_{50} and d_{20}, photon contamination (D_x), FWHM and 80%-20% penumbra width. Most simulated metrics fall with 2 mm of measurement, except for FWHM and penumbra metrics at 20×20 cm^2 MLC field-size for all energies. Here, the simulated widths fall short of measurement by as much as 5 mm in the crossline direction, however, this corresponds to a distance to agreement of 2.5 mm. Simulated penumbra widths are all within 3 mm of measurement.

Measured and simulated outputs for 5×5, 10×10 and 20×20 cm^2 MLC apertures with jaws set to 40×40 cm^2 are summarized in Table 5.3. Simulated outputs fall within 2% of measurement at 6 and 20 MeV, and within 4% of measurement at 12 MeV. Generally, simulated output factors at 20×20 cm^2 underestimate measurement by 2-3%.

Table 5.3: Measured and simulated electron output factors for the Clinac 21EX as function of MLC aperture with jaws set to 40×40 cm^2. Outputs are normalized to a 10×10 cm^2 jaw setting. Uncertainties are given in brackets.

Energy (MeV)		MLC Field Size (cm^2) 5×5	10×10	20×20
6	Measured	0.759 (0.008)	1.000 (0.01)	1.07 (0.01)
	Simulated	0.757 (0.004)	1.000 (0.002)	1.055 (0.003)
	Δ (Sim - Meas)	-0.002		-0.02
12	Measured	0.915 (0.009)	1.000 (0.01)	1.03 (0.01)
	Simulated	0.876 (0.004)	1.000 (0.002)	1.003 (0.003)
	Δ (Sim - Meas)	-0.039		-0.03
20	Measured	0.98 (0.01)	1.000 (0.01)	1.02 (0.01)
	Simulated	0.983 (0.007)	1.000 (0.004)	1.002 (0.006)
	Δ (Sim - Meas)	0.003		-0.02

5.1.3 Discussion

Overall, the complete electron Monte Carlo models of the Clinac 21EX presented here agree with measurement within 3%/3 mm and model output dependencies on MLC size within 4%. Deficiencies exist primarily in the profile and penumbra widths where simulated crossline profiles fall short of measurement by as much as 5 mm for the largest field size tested. Simulated inline penumbra widths are in better agreement with measurement, differing by only 3 mm for the largest field sizes.

As discussed in Section 4.4, studies by Weinberg et al. [112] and by Huang et al. [49] showed profile shape to be dependent on source width and divergence. Because the source parameters used in this work were manually optimized, only source width was examined, assuming zero divergence. Additionally, only symmetric sources were explored, while Huang et al. showed the true electron source is elliptical in shape. With more sophisticated parameter optimization tools to investigate these and other parameters, improvements to the model may have been achievable, however, the development of such tools was beyond the scope of this work.

While the performance of these models could be improved to achieve better agreement between simulation and measurement, agreement of 3%/3 mm compared to measurement was the goal of this proof of principle work, especially given that the ultimate aim was to build TrueBeam electron source models based on the models presented here. This is the focus of the next section.

5.2 Complete Monte Carlo model of the TrueBeam

Although the internal specifications of the TrueBeam are proprietary, some changes resulting from the reengineering process are known qualitatively. In particular, the bending magnet, carrousel, and electron scattering foils have been redesigned, the primary collimator is thicker than in older units, and an anti-backscatter foil has been added [19, 13, 41]. The net result of these changes produces photon fields [13] and electron fields [72] (Chapter 4) that are similar to those produced by older Varian machines.

In the last section, complete accelerator models of Clinac 21EX electrons that agreed with measurement within 3%/3 mm were presented. In this section, these models are modified in an attempt to match the dosimetric beam properties of TrueBeam electron fields within 3%/3 mm.

5.2.1 Methods

Models and simuliations

Monte Carlo models of the Clinac 21EX presented in Section 5.1.1 were modified in the same manual iterative process described previously in order to match the dosimetric beam properties of the TrueBeam within 3% and 3 mm. Given the knowledge that the TrueBeam scattering foils have been redesigned "from the ground up", various scattering foil dimensions and materials were investigated in order to remedy the differences in profile shape between simulation and measurement. In the end, the same materials specified for the Clinac 21EX scattering foils were used to model the TrueBeam scattering foils.

As before, BEAMnrc and DOSXYZnrc were used to perform simulations using VIMC (Section 3.2.1). Photon and electron cut-off energies were set to `AP` = `PCUT` = 0.01 MeV and `AE` = `ECUT` = 0.7 MeV, respectively, and `ESAVE` = 2.0 MeV. A 2.0 MeV `ESAVE` value was used in this work for efficiency purposes after the change was shown to have no impact on the dosimetric parameters being measured. Dose was calculated in a $30 \times 30 \times 30$ cm^3 water phantom with a $0.2 \times 0.2 \times 0.2$ cm^3 voxel grid based on an empty CT Dicom image set generated in the same fashion described in Section 5.1.1. Approximately 10^9 particles were simulated to achieve statistical uncertainties better than 1% in voxels receiving at least 50% of the maximum dose.

Measurements

The diode measurements presented in Section 4.2 of MLC-shaped fields delivered by the TrueBeam in water are used here for benchmarking. Relative depth and profile measurements for 5×5, 10×10 and 20×20 cm^2 MLC-apertures (defined at isocenter) with secondary collimating jaws set to 40×40 cm^2 were acquired for 6, 12, and 20 MeV electrons. Additionally, 5×5 and 20×20 cm^2 fields were delivered with jaws set to 6×6 and 21×21 cm^2, respectively, for all three energies. Profiles are in the crossline and inline directions at nominal values of d_{max} and d_{50} where $d_{max} = 1.4$, 2.7, and 2.2 cm and $d_{50} = 2.4$, 5.1 and 8.3 cm for 6, 12 and 20 MeV electrons, respectively. Further details are summarized in Sections 3.1.2 and 4.2.1.

The same relative output measurements used in Section 4.2 are also used here. Outputs were assessed for 5×5, 10×10 and 20×20 cm^2 MLC-shaped apertures at 70 cm SSD at with jaws set at 40×40 cm^2 for 6, 12 and 20 MeV electrons. Additionally, to investigate the role of jaw placement in MLC field shaping, output was also tracked as a function of jaw position for a fixed 5×5 cm^2 MLC-shaped field. Jaws were positioned from 5×5 cm^2 to 40×40 cm^2 in 1 cm increments up to 11×11 cm^2 where the interval gradually increased. Outputs for 6 MeV electrons were acquired at 1.5 cm depth in Solid Water while outputs for 12 and 20 MeV electrons were acquired at 2.5 cm depth. Uncertainty in output measurements was assessed from the variation in repeated measurements as well as the positioning uncertainty described in Chapter 3.

5.2.2 Results

PDDs and profiles

The source parameters that achieved the best agreement with measurement for each of the TrueBeam electron energies simulated are summarized in Table 5.4. Foil dimensions are given relative to the nominal values specified for the Clinac 21EX in the Monte Carlo data package.

Table 5.4: Model parameters for complete MC modelling of TrueBeam electrons.

Nominal Energy (MeV)	Incident Energy (MeV)	Source Width (cm)	Primary Foil Thickness (relative to nominal)	Secondary Foil Width (relative to nominal)
6	6.75	0.65	1.00	1.00
12	13.35	0.30	1.20	1.08
20	22.10	0.35	1.00	1.10

Figures 5.3 and 5.4 compare measured TrueBeam electron PDDs and profiles against those simulated using the modified complete accelerator model described in Section 5.2.1. Figure 5.3 shows PDDs and profiles for 5×5, 10×10 and 20×20 cm^2 MLC-shaped fields with jaws set to 40×40 cm^2 while Figure 5.4 shows 5×5 and 20×20 cm^2 MLC fields with jaws set 1 cm larger than the aperture.

For all energies, field sizes and jaw configurations, more than 99% of simulated depth dose points agree with measurement within 2%/2 mm. At 12 and 20 MeV, at least 98% of profile dose points agree within 2%/2 mm, while the 6 MeV model requires that agreement criteria to be extended to 3%/3 mm for at least 80% of data points to agree with measurement for the 5×5 cm^2 field. For the 20×20 cm^2 field at 6 MeV, by extending the gamma criterion to 3%/3 mm, at least 93% of profile data points agree with measurement. When the jaws are set 1 cm wider than the MLC aperture, all simulated profiles agree with measurement within 3%/3 mm except for the 5×5 cm^2 profile at dmax for which only 82% of data points pass.

Table 5.5 summarizes depth and profile characteristics for the measured and simulated TrueBeam electron fields shown in Figure 5.3 while Table 5.6 summarizes the same characteristics for the curves plotted in Figure 5.4. Differences between Monte Carlo and simulation at 12 and 20 MeV are well within 2 mm for distance metrics

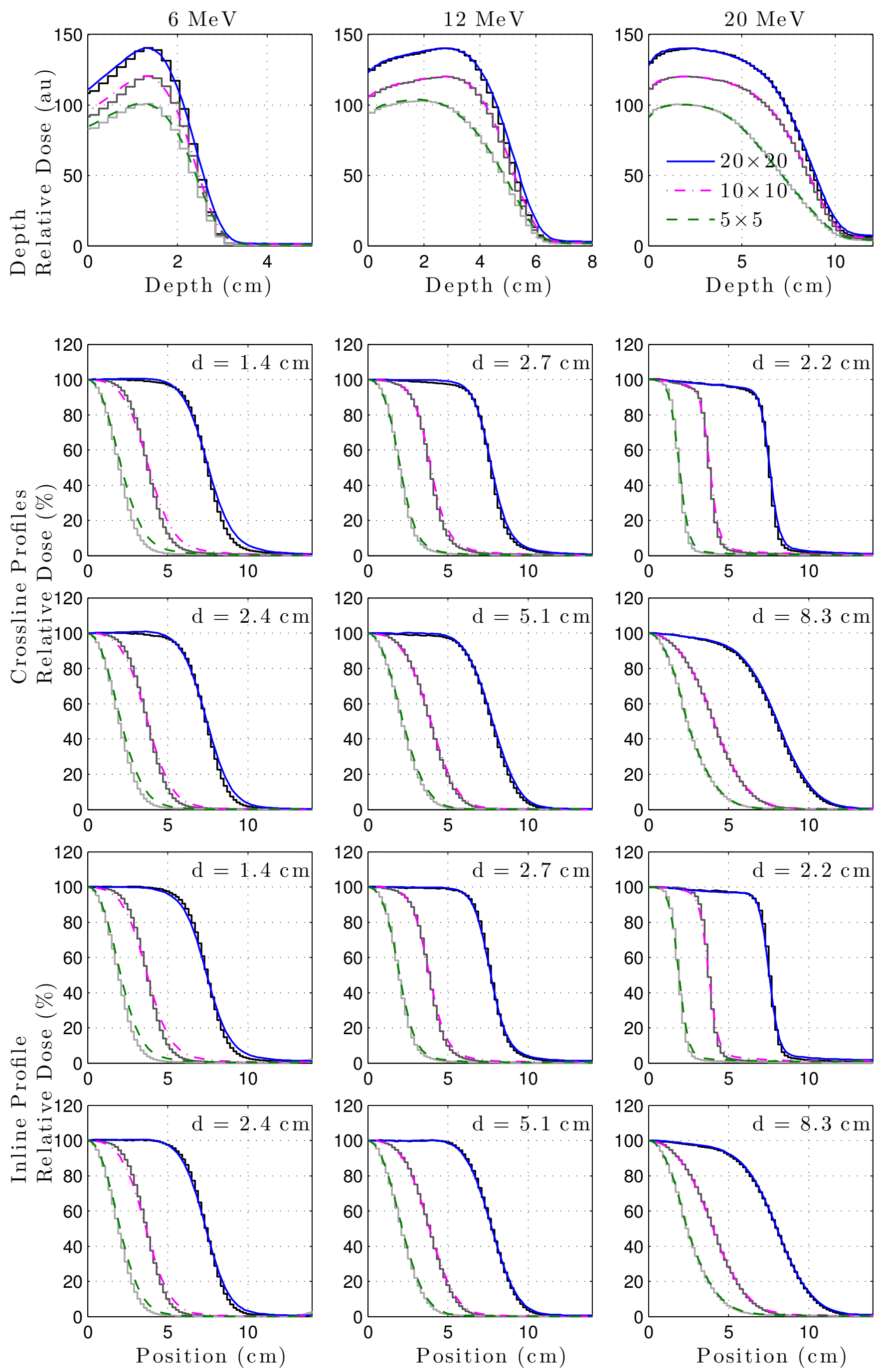

Figure 5.3: Relative measured (coloured lines) and Monte Carlo simulated (histogram) PDDs and profiles for TrueBeam electron fields at 6, 12 and 20 MeV for 5×5, 10×10 and 20×20 cm^2 MLC-apertures. Jaws are set to 40×40 cm^2. PDDs are scaled for visual clarity: 5×5 cm^2 to 100% (green), 10×10 cm^2 to 120% (magenta) and 20×20 cm^2 to 140% (blue).

Table 5.5: Measured and simulated dose parameters for TrueBeam electron fields at 6, 12 and 20 MeV for 5×5, 10×10 and 20×20 cm^2 MLC-apertures. Jaws are set to 40×40 cm^2. Width metrics are given in crossline (cross) and inline (in) orientations. Uncertainties in distance metrics are mostly with 1 mm except for penumbra metrics which are within 2 mm. Uncertainty in simulated distance metrics is 1 mm.

MLC (cm^2)	5×5		10×10		20×20	
	Diode	MC	Diode	MC	Diode	MC
			6 MeV			
d_{90} (cm)	1.8	1.8	1.8	1.8	1.8	1.8
d_{80} (cm)	2.0	2.0	2.0	2.0	2.0	2.0
d_{50} (cm)	2.4	2.4	2.4	2.4	2.4	2.4
d_{20} (cm)	2.8	2.7	2.8	2.7	2.8	2.7
D_x (%)	0.2	0.2	0.4	0.2	0.5	0.2
$\mathrm{FWHM}_{\mathrm{cross}}$(cm)	4.2	3.9	7.6	7.5	15.0	14.9
80-20$\%_{\mathrm{cross}}$ (cm)	1.9	1.6	2.2	1.7	2.2	1.8
$\mathrm{FWHM}_{\mathrm{in}}$ (cm)	4.1	3.9	7.4	7.4	14.9	14.9
80-20$\%_{\mathrm{in}}$ (cm)	1.8	1.5	2.1	1.6	2.1	1.8
			12 MeV			
d_{90} (cm)	3.4	3.4	3.9	3.9	4.0	3.9
d_{80} (cm)	3.9	3.9	4.3	4.3	4.4	4.3
d_{50} (cm)	4.9	4.8	5.1	5.0	5.1	5.0
d_{20} (cm)	5.7	5.6	5.7	5.6	5.8	5.6
D_x (%)	0.8	0.9	1.0	1.0	1.3	1.1
$\mathrm{FWHM}_{\mathrm{cross}}$(cm)	4.1	4.0	7.9	7.8	15.5	15.4
80-20$\%_{\mathrm{cross}}$ (cm)	1.4	1.3	1.6	1.4	1.6	1.5
$\mathrm{FWHM}_{\mathrm{in}}$ (cm)	3.9	3.9	7.7	7.7	15.3	15.4
80-20$\%_{\mathrm{in}}$ (cm)	1.4	1.3	1.6	1.4	1.5	1.5
			20 MeV			
d_{90} (cm)	4.4	4.4	5.6	5.5	5.7	5.8
d_{80} (cm)	5.3	5.3	6.6	6.6	6.8	6.8
d_{50} (cm)	7.2	7.1	8.2	8.2	8.4	8.3
d_{20} (cm)	9.1	9.0	9.6	9.5	9.6	9.5
D_x (%)	3.4	3.2	3.9	3.4	4.4	3.8
$\mathrm{FWHM}_{\mathrm{cross}}$(cm)	3.9	3.8	7.7	7.6	15.1	15.1
80-20$\%_{\mathrm{cross}}$ (cm)	0.8	0.7	0.9	0.7	0.9	0.8
$\mathrm{FWHM}_{\mathrm{in}}$ (cm)	3.8	3.8	7.5	7.6	15.1	15.2
80-20$\%_{\mathrm{in}}$ (cm)	0.8	0.7	0.9	0.7	0.9	0.8

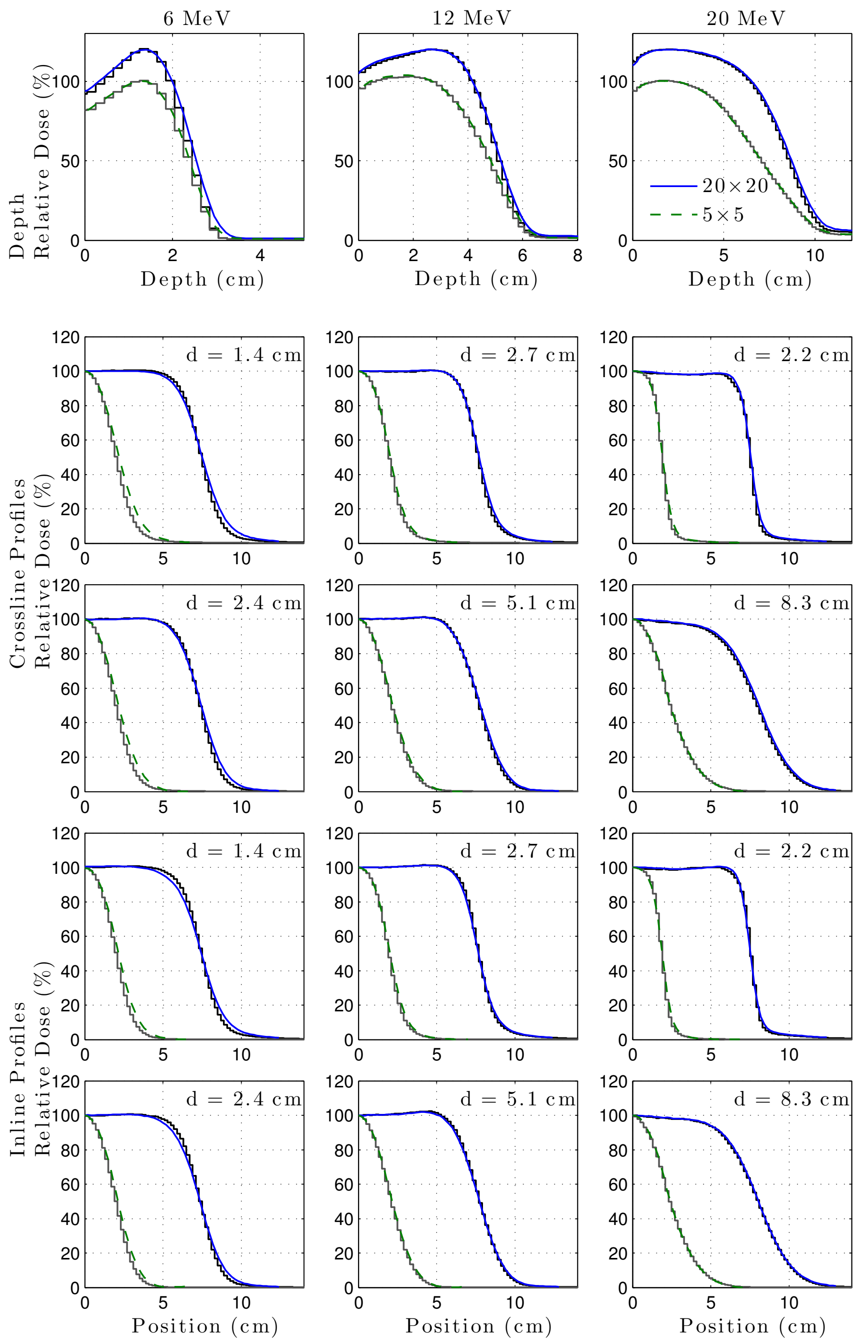

Figure 5.4: Relative measured (coloured lines) and Monte Carlo simulated (histogram) PDDs and profiles for TrueBeam electron fields at 6, 12 and 20 MeV for 5×5 and 20×20 cm^2 MLC-apertures. Jaws are set to the MLC aperture + 1 cm. 20×20 cm^2 data is plotted in blue while 5×5 cm^2 data is plotted in green. Depth plots are scaled for visual clarity: 5×5 cm^2 to 100% (green) and 20×20 cm^2 to 120% (blue).

Table 5.6: Measured and simulated dose parameters for TrueBeam electron fields at 6, 12 and 20 MeV for 5 × 5 and 20 × 20 cm^2 MLC-apertures. Jaws are set to the aperture + 1 cm. Width metrics are given in crossline (cross) and inline (in) orientations. Uncertainties in distance metrics are mostly with 1 mm except for penumbra metrics which are within 2 mm. Uncertainty in simulated distance metrics is 1 mm.

MLC (cm^2)	5 × 5		20 × 20	
	Diode	MC	Diode	MC
	6 MeV			
d_{90} (cm)	1.8	1.8	1.9	1.8
d_{80} (cm)	2.0	2.0	2.1	2.0
d_{50} (cm)	2.4	2.4	2.5	2.4
d_{20} (cm)	2.8	2.7	2.8	2.7
D_x (%)	0.2	0.2	0.4	0.2
$FWHM_{cross}$(cm)	4.4	4.1	15.0	14.9
80-20%$_{cross}$ (cm)	1.9	1.6	2.2	1.8
$FWHM_{in}$ (cm)	4.3	4.1	14.9	14.9
80-20%$_{in}$ (cm)	1.7	1.5	2.2	1.7
	12 MeV			
d_{90} (cm)	3.4	3.4	3.9	3.9
d_{80} (cm)	3.9	3.9	4.3	4.3
d_{50} (cm)	4.8	4.8	5.0	5.0
d_{20} (cm)	5.7	5.6	5.7	5.6
D_x (%)	0.8	0.9	1.2	1.1
$FWHM_{cross}$(cm)	4.1	4.0	15.4	15.3
80-20%$_{cross}$ (cm)	1.5	1.3	1.7	1.5
$FWHM_{in}$ (cm)	4.0	3.9	15.3	15.4
80-20%$_{in}$ (cm)	1.4	1.3	1.6	1.5
	20 MeV			
d_{90} (cm)	4.3	4.3	5.8	5.7
d_{80} (cm)	5.2	5.2	6.8	6.7
d_{50} (cm)	7.1	7.1	8.4	8.3
d_{20} (cm)	9.0	9.0	9.7	9.5
D_x (%)	3.1	2.9	4.2	3.7
$FWHM_{cross}$(cm)	3.8	3.8	15.1	15.1
80-20%$_{cross}$ (cm)	0.9	0.7	1.0	0.8
$FWHM_{in}$ (cm)	3.8	3.8	15.1	15.1
80-20%$_{in}$ (cm)	0.9	0.7	0.9	0.8

and within 1% for dose metrics. At 6 MeV, simulated depth-dose metrics are within 1 mm of measurement while profile metrics are mostly within 3 mm. The disagreement observed in profile widths at 6 MeV is due, primarily, to the discrepancy in penumbra slope between measurement and simulation at all field sizes and jaw settings. Note that any differences in measured and simulated FWHM represent twice the distance to agreement.

Outputs

Table 5.7 summarizes output factors for 5×5 and 20×20 cm^2 MLC apertures relative to a 10×10 cm^2 aperture with jaws set to 40×40 cm^2. At 12 and 20 MeV, simulated output factors fall within 1.3% and 4% of measurement, respectively. At 6 MeV, however, the simulated output for a 5×5 cm^2 MLC aperture is almost 14% higher than measurement while the simulated output at 20×20 cm^2 is 7% lower than measurement. Overall, simulated output factors for 20×20 cm^2 fields are lower than measurement.

Table 5.7: Measured and simulated electron output factors for the TrueBeam as a function of MLC aperture with jaws set to 40×40 cm^2. Outputs are normalized to a 10×10 cm^2 jaw setting. Uncertainties are given in brackets.

Energy (MeV)		MLC Field Size (cm^2) 5×5	10×10	20×20
6	Measured	0.667 (0.007)	1.00 (0.01)	1.10 (0.01)
	Simulated	0.802 (0.002)	1.000 (0.002)	1.029 (0.003)
	Δ (Sim - Meas)	0.135		-0.07
12	Measured	0.882 (0.009)	1.000 (0.01)	1.04 (0.01)
	Simulated	0.895 (0.003)	1.000 (0.003)	1.028 (0.004)
	Δ (Sim - Meas)	0.013		-0.01
20	Measured	0.96 (0.01)	1.00 (0.01)	1.03 (0.01)
	Simulated	0.947 (0.005)	1.000 (0.004)	0.989 (0.006)
	Δ (Sim - Meas)	-0.01		-0.04

Figure 5.5 compares measured and simulated output factors for a 6 MeV, 5×5 cm^2 MLC-shaped field with varying jaw setting. Output factors are normalized to a 40×40 cm^2 jaw setting. Measured data shows output to be most sensitive to jaw position when the jaw setting is within 10 cm of the MLC-field (jaws set 5 cm from each field edge). While the complete accelerator model does demonstrate this overall

trend, the simulated curve deviates from measured data in the shoulder of the curve, and discrepancies between measurement and simulation are as large as 15%.

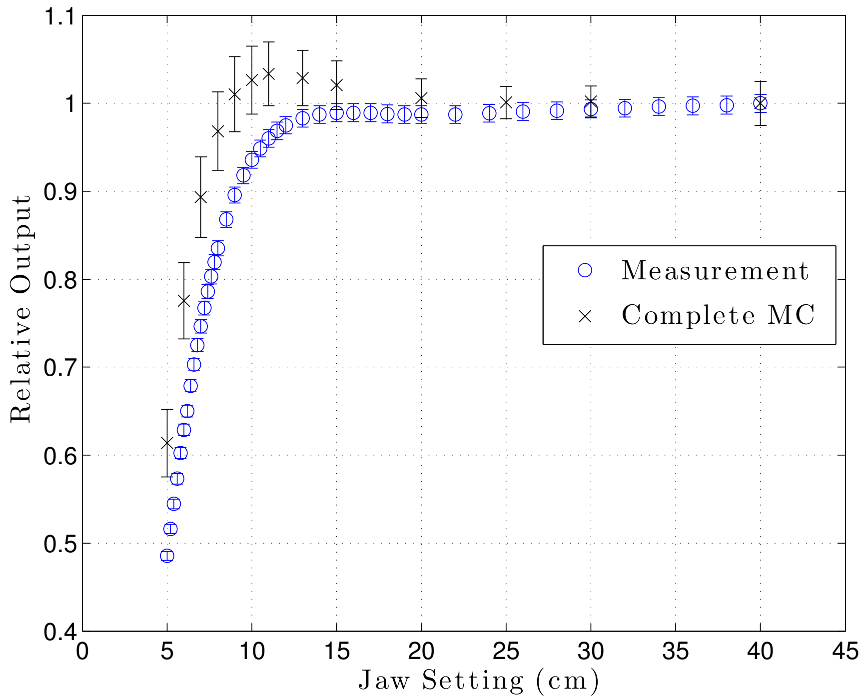

Figure 5.5: Measured and simulated electron output factors as a function of jaw size for a fixed 5×5 cm^2 MLC-aperture at 6 MeV. Outputs are normalized to a 40×40 cm^2 jaw setting. Error bars reflect measurement uncertainty and statistical uncertainty in the Monte Carlo simulation.

5.2.3 Discussion

At 12 and 20 MeV, Figures 5.3 and 5.4 and Tables 5.5 and 5.6 demonstrate the successful modification of Clinac 21EX Monte Carlo models to simulate the relative dosimetric characteristics of TrueBeam electron fields within 2%/2 mm for 98% of data points. Table 5.7 demonstrates the ability of these models to simulate changes in output as a function MLC-aperture within 4%. At 6 MeV, however, substantial discrepancies exist between simulation and measurement that have not been resolved by modifying the available model parameters, namely, the primary electron energy, source width and scattering foil dimensions. Additionally, the substantial differences between measured and simulated output dependence on jaw and MLC position of nearly 14% is indicative of a fundamental deficiency in the complete accelerator model for this energy.

In comparison, the dual-source TrueBeam model presented by Henzen et al. [45] achieved agreement with measurement that was largely within 3%/3 mm for 6, 12 and 22 MeV fields. Relative output data was presented for only one field size, however, a 5×5 cm^2 MLC with 15×34 cm^2 jaws compared to the reference field, 15×34 cm^2 MLC and jaws. Absolute dose differences between measurement and simulation were within 2% for the reference field and mostly within 3% for the smaller field, showing good representation of output dependence on MLC position for the range examined.

Given that the scattering foils have been entirely re-engineered for the TrueBeam, and because electron scattering power varies inversely with the square of the energy [61], it is not surprising that the 6 MeV beam would be the most difficult to model based on the Clinac 21EX geometry. Underestimates of penumbra slope compared to measurement may be indicative of a missing scattering component from some part of the accelerator geometry that was not modelled, like shielding, or of components that were sub-optimally modelled for electron field simulation.

In the Clinac 21EX jaw model used in this work, jaw divergence is defined to project to a point in the plane of the photon target. The TrueBeam Monte Carlo Data Package, which contains schematics for only the beam shaping components of the TrueBeam, became available following the conclusion of this work and specifies that the jaw divergence projects to a 3×3 mm^2 square in the plane of the photon target. The jaw model used in this work was not corrected to account for this. The resulting changes in jaw position are on the order of millimetres, and, as will be seen in Chapter 6, have little impact on the depth and profile characteristics of MLC-shaped fields, but do play an important roll in the relative output curve plotted in Figure 5.5.

5.3 Conclusions

Repurposing complete Monte Carlo models of the Clinac 21EX linear accelerator to simulate electron fields produced by the TrueBeam was accomplished with mixed results. Because the exact schematics were available, modelling the Clinac 21EX was reasonably straight forward. The manual iterative optimization process was used to define complete accelerator models that agreed with measured data within 3%/3 mm for all three energies investigated. For the TrueBeam, at 12 and 20 MeV, simulations fall within 2%/2 mm of relative measured data while simulated output factors fall within 4% of measurement. These models were deemed to be appropriate for investigations into MERT and MPERT optimization and treatment planning. Modelling the TrueBeam at 6 MeV proved more challenging. The best complete model at 6 MeV was able to achieve, for the most part, relative depth and profile dose agreement with measurement of 3%/3 mm, however, differences in relative output were as large as 14%. In order to perform MERT simulations, a look-up table would be required in order to simulate relative dose changes with field size to within 3%. Although unsatisfying as a solution, this would be acceptable for early investigations into MERT and MPERT planning and optimization.

Near the conclusion of this work, Varian released electron phase-spaces sources of the TrueBeam scored below the last field-independent structure in the linear accelerator and above the secondary collimating jaws. These phase-spaces allow for Monte Carlo simulation of the TrueBeam that do not require explicit knowledge of the internal schematics of the accelerator above the field-dependent modifiers. These phase-spaces are evaluated for MERT and MPERT applications in the following chapter.

Chapter 6

Results & Discussion III: Phase-space source files for Monte Carlo simulations of MLC-shaped electron fields

The complete Monte Carlo models described in Chapter 5, used to simulate electron fields generated by the TrueBeam, failed to reflect measured changes in output as a function of field size at 6 MeV within 3%, as was intended, despite producing relative PDD and profile curves that agreed with measurement, for the most part, within 3%/3 mm. At about the same time this was becoming evident, Varian published electron phase-space source files for the TrueBeam. The phase-space files were generated with the GEANT4 transport code (v10.0.patch1) [1] using a model based on those described in an article by Constantin et al. [23] outlining the production of phase-space source files for TrueBeam photon fields. Initially, these phase-spaces were scored on a cylindrical surface to account for the arc-trajectory of the y-jaws around the primary collimator. Eventually, these phase-spaces were processed to be scored on a single z-plane for end-user software compatibility. Rodrigues et al. [88] described the non-proprietary specifics of the electron simulations and compared the results of phase-space-based simulations with measurement. Even with manufacturer specifications, the authors initially found that simulations underestimated measured dose for open fields by 8%, 10-20 cm from the beam axis. Changing the properties of the incident electron source were found to make no improvement, however, decreasing the thickness of the monitor chamber windows to 80% of their nominal value in conjunction with slight adjustments to primary scattering foil was found to address this deficiency. All modifications fell within manufacturer's specified fabrication tolerances of 20% for the ion chamber window thickness and less than 10% for the thin, outermost step of the secondary scattering foil.

When used as the source in Monte Carlo simulations performed using BEAMnrc and DOSXYZnrc, Rodrigues et al. showed the phase-spaces to produce dose distributions that agreed with end-user measurement within 2%/1 mm, for the most part, for conventional electron fields shaped by applicators and delivered at 100 cm SSD. In this chapter, the phase-spaces' accuracy are tested in simulations of MERT and MPERT fields shaped with photon MLCs, delivered at short SSD. Depth and profile characteristics, as well as relative output as a function of field size are investigated.

6.1 Methods

6.1.1 Measurement

PDDs and profiles

The same relative dose measurements of TrueBeam electron fields shaped with MLCs and delivered at 70 cm SSD presented in Chapters 4 and 5 were used to benchmark simulations performed with the phase-space source files. Depth and profile scans for 5×5, 10×10 and 20×20 cm^2 MLC-shaped fields (defined at isocentre) with jaws set to 40×40 cm^2 were used. Profiles were taken at nominal values of d_{max} where d_{max} = 1.4, 2.7, and 2.2 cm. Further details are summarized in Sections 3.1.2 and 4.2.1.

Outputs

To assess output dependencies on MLC-aperture and jaw setting in configurations relevant to MERT and MPERT, output measurements were performed at 70 cm SSD using the Markus chamber in Solid Water. Outputs were assessed for MLC apertures ranging in size from 3×3 to 25×25 cm^2 (defined at isocentre) with jaws set to 40×40 cm^2. In addition, 5×5, 10×10 and 20×20 cm^2 MLC-shaped fields were delivered with jaw settings ranging from the MLC aperture size to 40×40 cm^2 in increments of 1 cm when the jaws were closest to the MLC-defined field edge and the output gradient was highest, increasing to increments of 10 cm when the jaws were furthest from the MLC-defined field edge. Again, the full range of jaw positions was assessed to evaluate the role of jaw position in MLC electron field shaping. To verify that there was no field-size dependence on the response of the Markus chamber at the smallest field sizes, a subset of Markus measurements were compared against EFD^{3G} scanning field diode output measurements in water. Differences were less than 0.2% at the smallest field sizes. Measurements for 6 MeV fields were performed at 1.5 cm depth while measurements for 12 and 20 MeV electrons were performed at 2.5 cm depth.

6.1.2 Monte Carlo

TrueBeam electron source phase-space files are available in IAEA format on the Varian website and are scored 26.7 cm from the source, just above the secondary collimating jaws. These files are made available for research use and modifications to their source parameters cannot be made without registering for Varian's pay-per-use TrueBeam simulation service, VirtuaLinac. Before they could be used, the header file for each phase-space file had to be modified to specify that the cosine direction along the beam axis was stored and to set all particle weights to 1. This was done by modifying the line '0 // W is stored ?' under RECORD_CONTENTS to read '1 // W is stored ?' and by adding the line '1 // Constant Weight' under RECORD_CONSTANTS. Each phase-space was available as a set of 1 GB phase-space files (between 20 and 25 individual files depending on the energy) that were downloaded separately and summed to form a single source. Even with the header modifications, the IAEA formatted phase-spaces are not compatible with BEAMnrc 2008, but are compatible with BEAMnrc 2013, therefore, BEAMnrc 2013 or later should be used in any future work.

The BEAMnrc accelerator model used in this study consisted of JAWS, DYNVMLC and SLABS component modules to model the secondary collimating jaws, Millennium-120 MLC, and exit window respectively. Initially, the component modules used were identical to those specified in Chapter 5 with the addition of the mylar exit window. A block diagram of this accelerator model is given in Figure 6.1. Note that the component modules outlined in dashed lines were not included in the model and are shown here for reference only.

The y-jaws follow an arc trajectory while the x-jaws follow a linear trajectory and then tilt away from the central axis to match the divergence of the beam. Given these

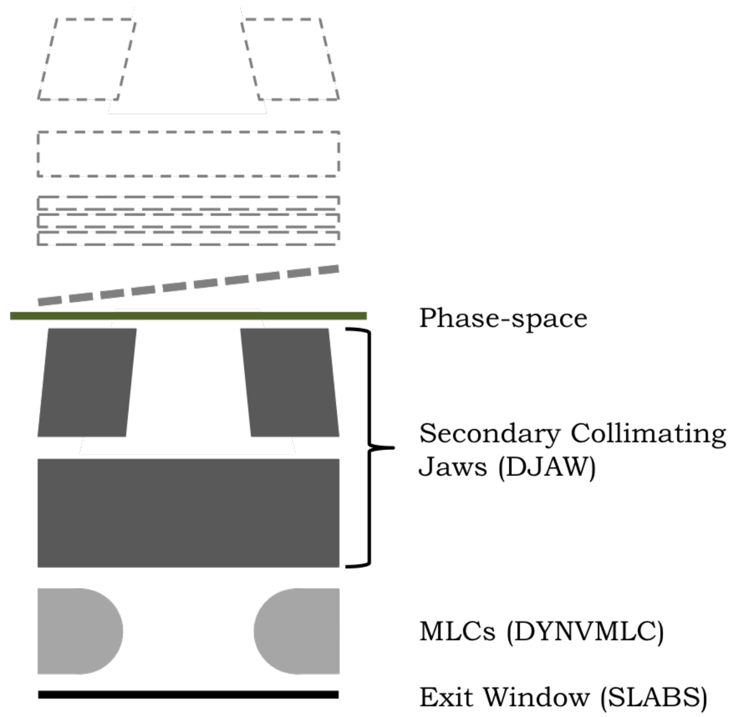

Figure 6.1: Block representation of the component modules used to model the field-specific components of the TrueBeam for phase-space based simulations. Note that the component modules outlined in dashed lines were not included in the model and are shown here for reference only.

allowed geometries, VIMC uses a back-end algorithm to determine jaw positions based on the field-size specified in the uploaded Eclipse-generated plan file. The TrueBeam Monte Carlo Data Package specifies that the divergence of the jaws projects to a 3×3 mm^2 square in the plane of the photon target when the jaws are closed, which is not accounted for in the VIMC jaw position algorithm. The VIMC algorithm, instead, projects jaw divergence back to a point in the target plane. Based on this new divergence information, jaw positions were recalculated outside of the VIMC infrastructure to account for both the jaw trajectory and divergence. In the process of recalculating jaw positions, it was discovered that the VIMC jaw algorithm also places the x-jaws 0.6 cm higher than specified in the Monte Carlo data package. This was also corrected in the independent jaw position calculations. A schematic of the geometry specified in the Monte Carlo data package is shown in Figure 6.2. Unless specified, the updated jaw model is used for the remainder of this dissertation.

Note that the component module JAWS models the top and bottom jaw surfaces to be orthogonal to the primary beam axis. The resulting modelled geometry

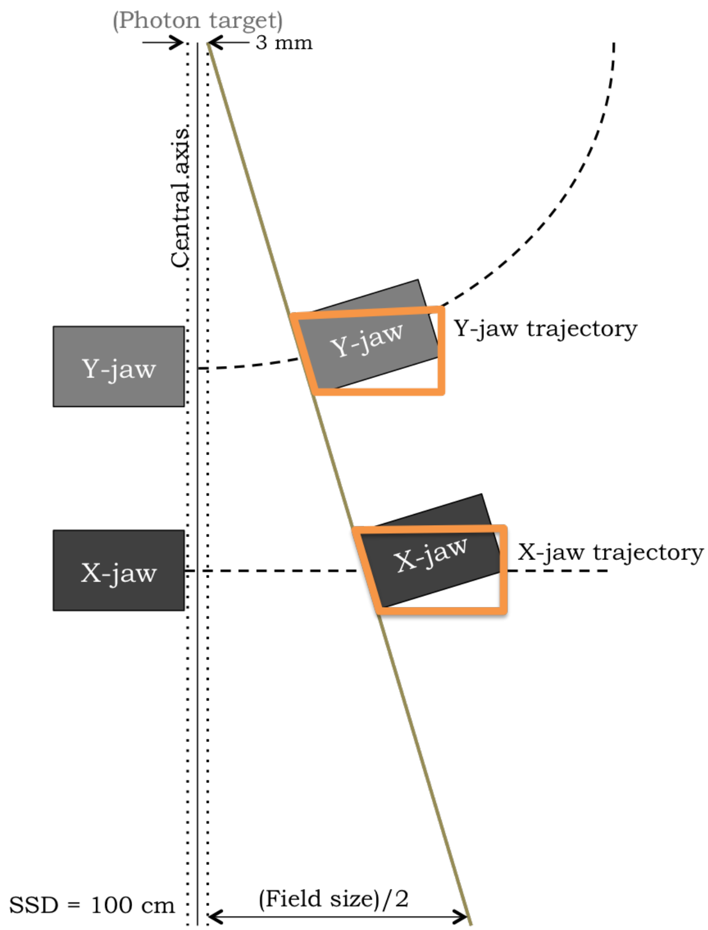

Figure 6.2: Schematic of x- and y-jaw trajectories and field definition for the Varian Clinac 21EX and TrueBeam linear accelerators. The component module JAWS models these positions as illustrated by the orange outline. X- and Y-jaws are shown moving in the same plane for illustration purposes only. Also, only one of each jaw-pair is shown positioned away from the central axis. For a symmetrically defined field, both jaws would be symmetrically positioned about the central axis. Image is not to scale.

is illustrated in Figure 6.2 by orange outlines. The impact of this approximation on simulated backscatter (discussed in Chapter 7) was investigated by adding a PYRAMIDS component module immediately before the JAWS module to explicitly model an oblique Y-jaw top surface. The effect was found to be negligible and the approximate model was used for simplicity throughout the remainder of this work.

DOSXYZnrc was used to score dose in water using the BEAMnrc output as its source. Dose was scored in a $30 \times 30 \times 15$ cm^3 water phantom with voxel dimensions of $0.2 \times 0.2 \times 0.2$ cm^3 specified within the DOSXYZnrc input file. In both BEAMnrc and DOSXYZnrc, the transport parameters `ECUT` and `PCUT` were set to 0.521 MeV and 0.01 MeV, respectively. Particle recycling was used in DOSXYZnrc and each particle was used no more than 9 times [109]. In the interest of saving disk space on the shared VIMC computer system, only the first ten available Varian phase-spaces were summed to form the 6 and 12 MeV sources for EGSnrc, corresponding to 6.5×10^8 and 4.2×10^8 primary histories, respectively. With particle recycling enabled in DOSXYZnrc, the mean statistical uncertainty for all voxels containing at least 50% of the maximum dose was better than 1%. In order to maintain the same level of uncertainty for 20 MeV, all twenty available phase-space source files were summed to form the 20 MeV source, corresponding to 7.0×10^8 primary histories. Calculation times ranged from 10 to 64 hours on 64 shared research cores.

6.2 Results

6.2.1 PDDs and profiles

Percent depth dose curves for 6, 12 and 20 MeV electrons are plotted in Figure 6.3 for 5×5, 10×10 and 20×20 cm^2 MLC-shaped apertures delivered at 70 cm SSD with jaws set to 40×40 cm^2. The central beam axis falls between data points in the Monte Carlo data sets, therefore, four voxels adjacent to the beam axis were averaged to interpolate each dose point along the beam axis. Each curve is normalized to the dose at nominal values of d_{max} and differences between simulation and measurement are included below each subplot. Differences between measured and simulated data are as large as 7.5% (global), however, with the addition of a distance to agreement tolerance, at least 98% of simulated PDD data points agree with measurement within 2%/2 mm. Overall, Monte Carlo underestimates dose in the build-up region.

Profiles at nominal values of d_{max} for the same 5×5, 10×10 and 20×20 cm^2 MLC-shaped apertures are shown in Figure 6.4 for 6, 12 and 20 MeV electrons in both the inline and crossline directions. Again, adjacent voxels were averaged to interpolate dose in the plane of the central axis, and differences between simulation and measurement are included below each subplot. In-field (within 90% of the normalized dose) the differences between measurement and simulation do not exceed 2.5% and the mean absolute difference is less than 1.5% for all profiles. Simulated curves underestimate measured dose in the shoulders and penumbra tails at 20 MeV for 10×10 and 20×20 cm^2 MLC-apertures.

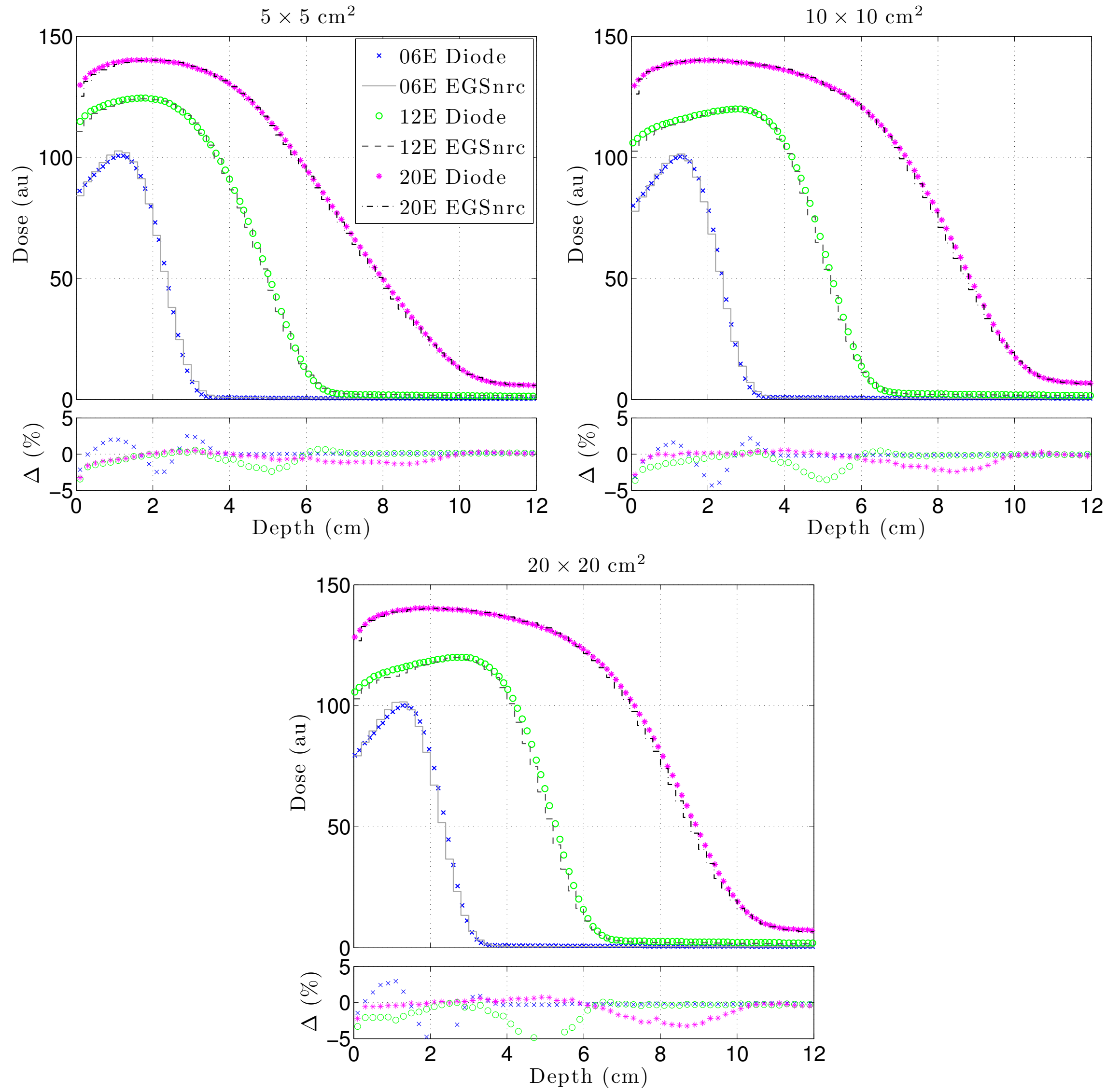

Figure 6.3: Percent depth dose curves for 5 × 5, 10 × 10 and 20 × 20 cm^2 MLC-defined apertures of 6, 12 and 20 MeV electrons. Jaws are set to 40 × 40 cm^2. Diode measurements are plotted as points, while Monte Carlo data are plotted as histograms. Percent differences between simulation and measurement are plotted in the lower panels. Data is scaled for visual clarity, 6 MeV to 100%, 12 MeV to 120% and 20 MeV to 140%.

Table 6.1 summarizes depth and width characteristics of the PDDs and profiles presented in Figures 6.3 and 6.4, including d_{90}, d_{80}, d_{50} and d_{20}, photon contamination (D_x), FWHM and 80%-20% penumbra widths. Simulated data agree with measurement within 1 mm for most distance parameters and within 2 mm for all distance parameters except for the crossline FWHM for a 20×20 cm^2 field at 6 MeV.

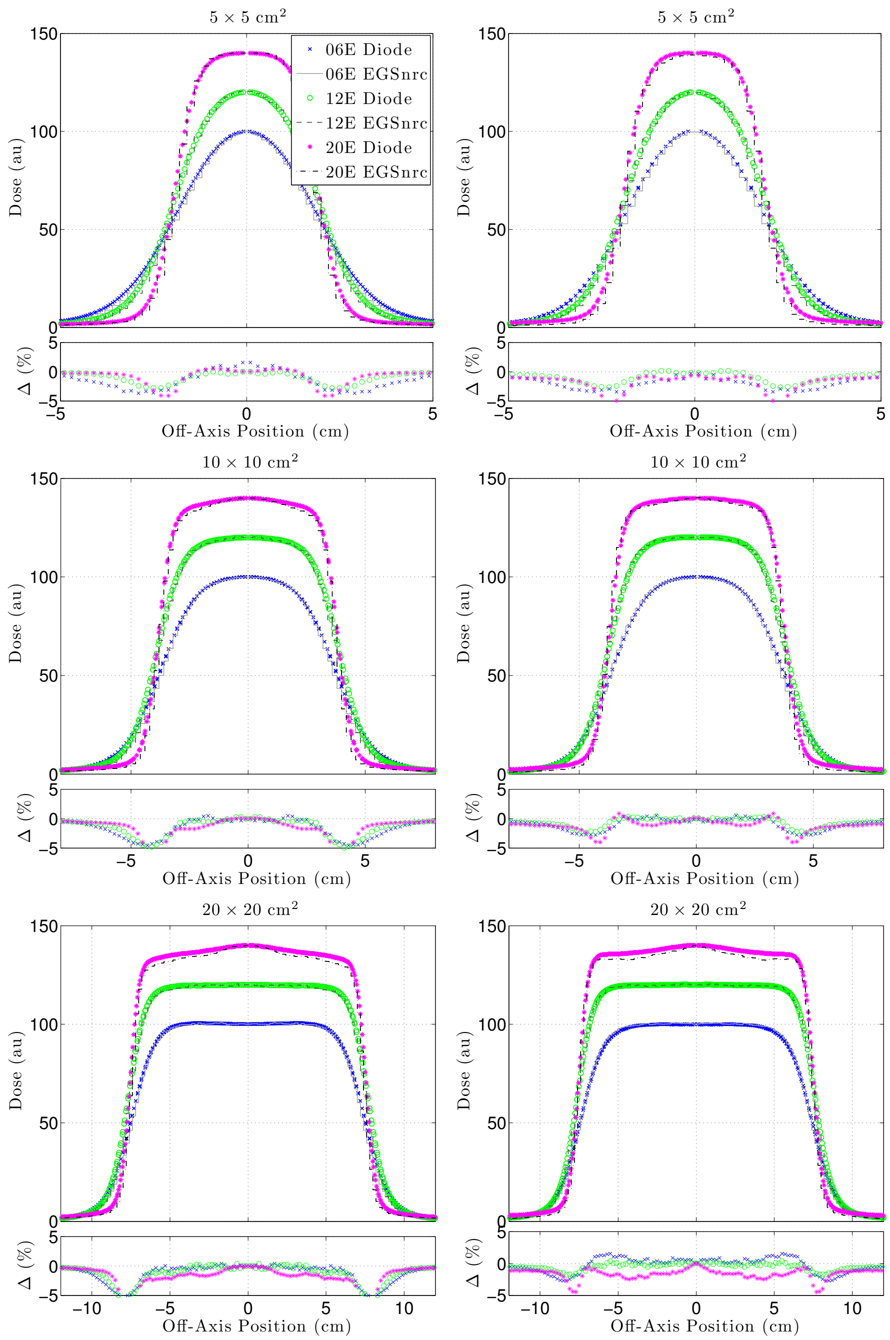

Figure 6.4: Crossline (left) and inline (right) profiles for 5×5 (top), 10×10 (middle) and 20×20 cm^2 (bottom) MLC-shaped apertures delivered with 6, 12 and 20 MeV electrons. Jaws are set to 40×40 cm^2. Diode measurements are plotted as points, while Monte Carlo data are plotted as histograms. Percent differences between simulation and measurement are plotted in the lower panels. Data is scaled for visual clarity, 6 MeV to 100%, 12 MeV to 120% and 20 MeV to 140%.

Note, however, that the 3 mm disagreement in width represents twice the distance to agreement. Overall, the FWHM and penumbra widths of simulated fields tend to be shorter than measurement in the crossline direction, with differences increasing with increasing field size, while inline FWHM metrics are within 1 mm of measurement. All simulated photon contamination metrics agree with measurement within 0.3%.

Gamma pass statistics using 2%/2 mm criteria for the PDDs and profiles presented in Figures 6.3 and 6.4 are summarized in Table 6.2. PDDs have better than 98% pass rates for all energies and field sizes and all 5×5 cm^2 profile metrics have 100% passing rates at all energies. At 10×10 cm^2, crossline profiles have better than 98% pass rates while the 20 MeV inline pass rate drops to 80%. At 20×20 cm^2, 12 MeV profiles still pass in both profile directions while 91% of dose points in the 6 MeV crossline profile pass and only 73% of dose points in the 20 MeV inline profile fall within 2%/2 mm of measurement. When gamma criteria are extended to 3%/3 mm, all simulated curves agree with measurement with the exception of the 20 MeV inline profile where 87% of dose points agree with measurement. Visually, this is corroborated by the obvious differences in flatness of the measured and simulated inline profile at 20 MeV (Figure 6.4).

6.2.2 Outputs

MLC outputs

Figure 6.5 plots measured and simulated output factors for 6, 12 and 20 MeV electron fields as a function of MLC-aperture sizes between 3×3 and 25×25 cm^2 with jaws set to 40×40 cm^2. Each output curve is normalized to a 10×10 cm^2 MLC-aperture. At 6 MeV, Monte Carlo overestimates the measured output by, at most, 4.0% at a 5×5 cm^2 MLC and underestimates the measured output by, at most, 2.7% at a 25×25 cm^2 MLC. At 12 MeV, simulated outputs fall within 0.7% of measured values except at the smallest field size where the discrepancy reaches 3.7%. At 20 MeV, simulation falls within 0.4% of measurement for all field sizes.

Jaw outputs

Figure 6.6 plots measured and simulated output factors for fixed 5×5, 10×10 and 20×20 cm^2 MLC-apertures as a function of jaw position. Each curve is normalized to the measured output of the particular MLC-aperture with jaws set to 40×40 cm^2,

Table 6.1: Measured and simulated characteristics of PDDs and profiles for 6, 12 and 20 MeV electron fields shaped with 5 × 5, 10 × 10 and 20 × 20 cm^2 MLC-shaped apertures delivered at 70 cm SSD. Jaws are set to 40 × 40 cm^2. Uncertainty in measured distance metrics is mostly with 1 mm except penumbra which are within 2 mm. Uncertainty in simulated distance metrics is 1 mm.

6 MeV	5 × 5		10 × 10		20 × 20	
	Diode	**EGSnrc**	**Diode**	**EGSnrc**	**Diode**	**EGSnrc**
d_{90} (cm)	1.7	1.7	1.8	1.7	1.8	1.7
d_{80} (cm)	2.0	1.9	2.0	1.9	2.0	1.9
d_{50} (cm)	2.4	2.3	2.4	2.3	2.4	2.3
d_{20} (cm)	2.8	2.8	2.8	2.8	2.7	2.8
D_x (%)	0.2	0.3	0.4	0.3	0.4	0.3
$FWHM_{cr}$ (cm)	4.2	4.0	7.6	7.4	15.1	14.8
80-20%$_{cr}$ (cm)	1.9	1.8	2.2	2.0	2.2	2.0
$FWHM_{in}$ (cm)	4.1	4.0	7.4	7.3	14.9	14.8
80-20%$_{in}$ (cm)	1.8	1.7	2.1	2.0	2.1	1.9
12 MeV	5 × 5		10 × 10		20 × 20	
	Diode	**EGSnrc**	**Diode**	**EGSnrc**	**Diode**	**EGSnrc**
d_{90} (cm)	3.4	3.4	3.9	3.9	3.9	3.9
d_{80} (cm)	3.9	3.8	4.3	4.3	4.3	4.2
d_{50} (cm)	4.8	4.8	5.1	5.0	5.0	5.0
d_{20} (cm)	5.7	5.6	5.7	5.7	5.7	5.7
D_x (%)	0.8	0.9	1.0	1.0	1.2	1.0
$FWHM_{cr}$ (cm)	4.1	4.0	7.9	7.7	15.5	15.2
80-20%$_{cr}$ (cm)	1.4	1.4	1.6	1.5	1.6	1.5
$FWHM_{in}$ (cm)	3.9	3.9	7.7	7.7	15.3	15.3
80-20%$_{in}$ (cm)	1.4	1.3	1.6	1.4	1.5	1.5
20 MeV	5 × 5		10 × 10		20 × 20	
	Diode	**EGSnrc**	**Diode**	**EGSnrc**	**Diode**	**EGSnrc**
d_{90} (cm)	4.4	4.4	5.6	5.5	5.7	5.7
d_{80} (cm)	5.2	5.2	6.6	6.5	6.8	6.7
d_{50} (cm)	7.1	7.1	8.2	8.2	8.4	8.2
d_{20} (cm)	9.1	9.0	9.6	9.5	9.6	9.5
D_x (%)	3.3	3.5	3.9	3.6	4.3	3.8
$FWHM_{cr}$ (cm)	3.9	3.8	7.7	7.5	15.1	14.9
80-20%$_{cr}$ (cm)	0.8	0.8	0.9	0.9	0.9	0.9
$FWHM_{in}$ (cm)	3.8	3.7	7.5	7.5	15.1	15.0
80-20%$_{in}$ (cm)	0.8	0.8	0.9	0.8	0.9	0.9

d_{90} = depth at 90% dose; d_{80} = depth at 80% dose; d_{50} = depth at 50% dose
d_{20} = depth at 20% dose; D_x = photon contamination measured 10 cm beyond the depth of 10% dose; FWHM = full width at half maximum;
80-20% = average width of the penumbra measured between 80% and 20% doses.

to remove the output discrepancies displayed in Figure 6.6 for the specified aperture. Agreement between simulation and measurement was within 1% for most data points

Table 6.2: One-dimensional gamma metrics for Monte Carlo simulated PDDs and profiles compared against measurement. Values represent the percent of dose points with greater than 5% of the normalized dose that agree with measurement within 2%/2 mm.

Field Size (cm^2)	Curve	6 MeV	12 MeV	20 MeV
	PDD	99%	100%	100%
5 × 5	crossline	100%	100%	100%
	inline	100%	100%	100%
	PDD	100%	98%	100%
10 × 10	crossline	98%	100%	100%
	inline	100%	100%	80%
	PDD	100%	100%	100%
20 × 20	crossline	91%	100%	81%
	inline	100%	100%	73%

across all energies and field sizes. The largest discrepancies of 2.3% and 1.5% occur for the 5×5 cm^2 MLC and jaw setting at 12 and 20 MeV, respectively.

6.2.3 Jaw model

Figures 6.7 and 6.8 compare Monte Carlo simulated depth and profile curves generated with the VIMC default jaw model and the updated jaw model based on the TrueBeam Monte Carlo Data Package. PDDs are shown for 6, 12 and 20 MeV electrons shaped by jaws set to a 5×5 cm^2 field (MLC retracted). Influence of the change in jaw model is most evident at 20 MeV, where the additional 3 mm separation of the jaws in the updated model increases the PDD by as much as 4% due to increased lateral scatter [61].

In Figure 6.8, crossline profiles at d_{max} are compared for 6 MeV electron fields shaped by jaws set to 5×5, 10×10 and 20×20 cm^2. Aside from the obvious increase in field size due to the 3 mm widening of jaw setting in the updated model, there is no change in profile shape. In fact, with a 1.5 mm distance to agreement, all data points agree within 1%. Comparisons at 12 MeV yield the same results while at 20 MeV the distance to agreement must be extended to 2 mm.

In the case of MLC-field shaping with the jaws set away from the periphery, profile and depth dose curves simulated using the VIMC and updated jaw models are

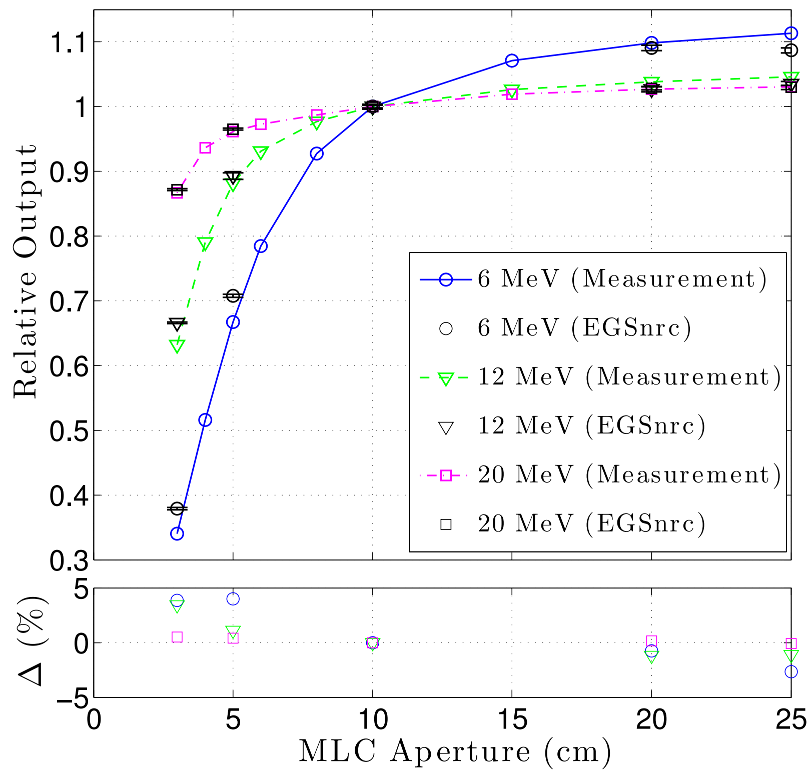

Figure 6.5: Measured and simulated relative outputs as a function of MLC-aperture size with fixed 40×40 cm^2 jaws for 6, 12 and 20 MeV electrons. Note that measurements are discrete and that the connecting line is intended only as a visual guide. The lower subplot indicates the percent difference between measurement and simulation, colour and symbol matching the corresponding curves in the main plot.

indistinguishable at all energies and field sizes. The dependence of relative outputs on jaw position, however, differs greatly between the two jaw models. Figure 6.9 shows relative dose outputs for fixed MLC-apertures as a function of secondary jaw position for 6, 12 and 20 MeV electrons shaped with 5×5, 10×10 and 20×20 cm^2 MLCs. Given the good agreement between measurement and data simulated using the updated jaw model (Figure 6.6), it is clear that the default VIMC jaw model is suboptimal for modelling this output dependency. While the default VIMC jaw model output curve follows the general trend of output curve - nearly constant and linear for jaws from 40×40 cm^2 to about 10 cm larger than the MLC-aperture size, increasing briefly with decreasing jaw setting and then dropping rapidly as jaws approach the MLC edge - the overall curvature of the simulated curve does not match the expected trend and differences in output are as large as 22%, 20% and 8% for 5×5 cm^2 MLCs and jaws at 6, 12 and 20 MeV, respectively. A similar effect is seen in Figure 5.5.

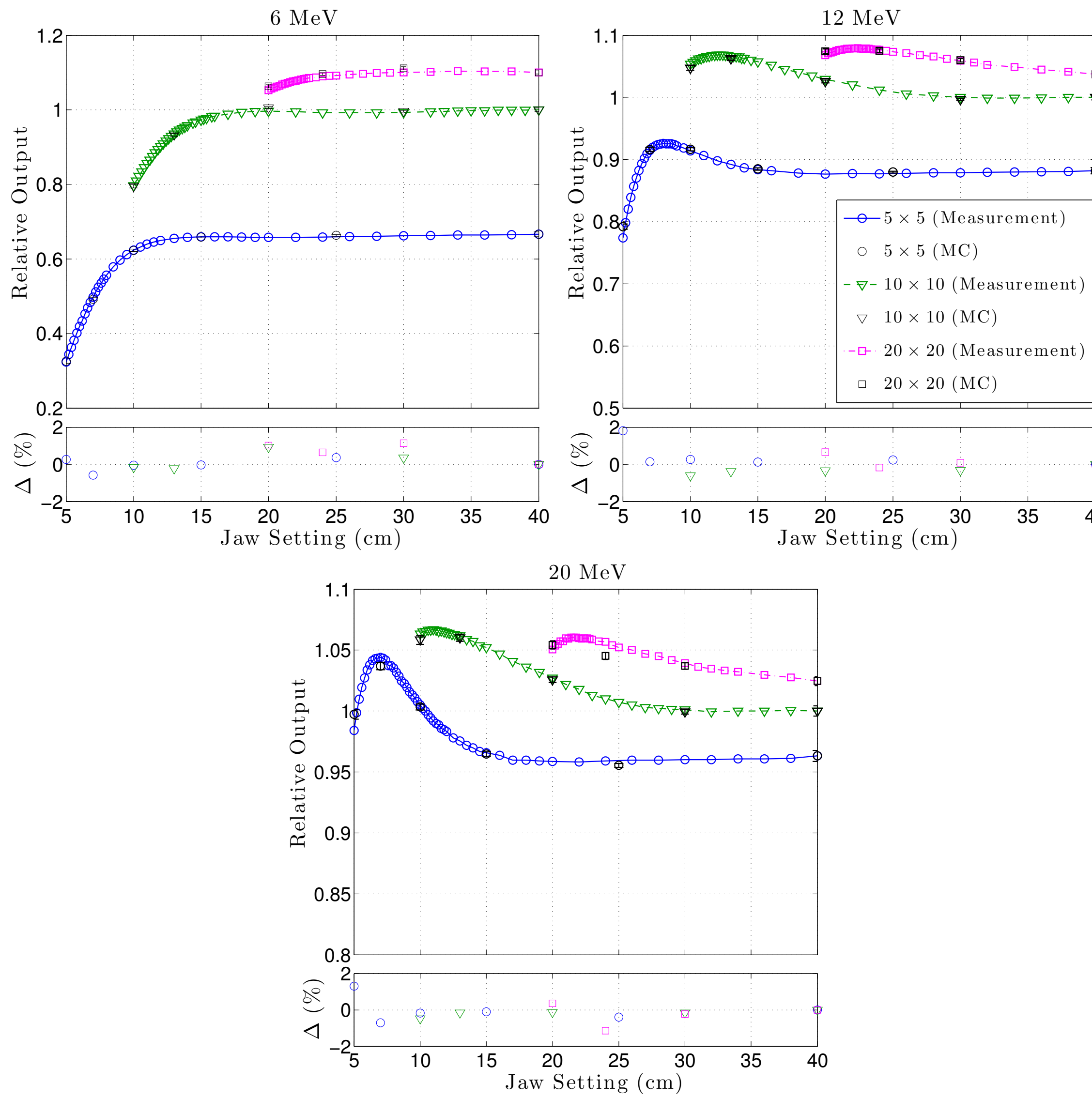

Figure 6.6: Measured and simulated relative outputs as a function of jaw-size for 6, 12 and 20 MeV electrons delivered with fixed 5×5, 10×10 and 20×20 cm^2 MLC-defined apertures. Note that measurements are discrete and that the connecting line is intended only as a visual guide. The lower subplot indicates the percent difference between measurement and simulation, colour and symbol matching the corresponding curves in the main plot.

6.3 Discussion

This was the first verification of Varian's TrueBeam electron phase-space source files for Monte Carlo simulations performed under modulated electron radiation therapy delivery conditions (MLC field-shaping and short SSD). Overall, the phase-spaces

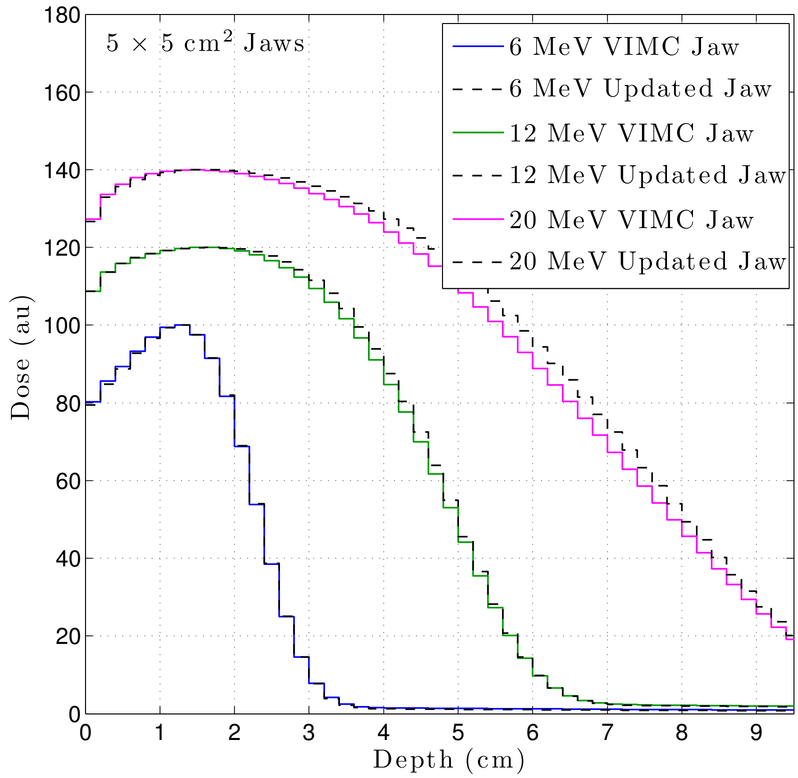

Figure 6.7: Simulated depth dose curves generated using the default VIMC and updated jaw models. PDDs are shown for 5×5 cm^2 jaw-shaped fields at 6, 12 and 20 MeV. Curves are scaled for visual clarity.

produced PDDs that agreed with measurement within 2%/2 mm, and profiles that agreed with measurement within 3%/3 mm at the energies and field sizes investigated, with one exception. Most output factors simulated using EGSnrc fell within 2.7% of measured output factors, however, discrepancies were as large as 4.0% for the smallest MLC-shaped field at 6 and 12 MeV.

The phase-spaces were previously benchmarked against measurement by Rodrigues et al. for large, open fields and applicator-shaped fields delivered at 100 cm SSD. The results of that study are consistent with those found here. As in Rodrigues et al., the phase-spaces produced depth dose curves that slightly underestimated dose in the build-up region, but agreed with measurement within 2% with a distance to agreement (2 mm in this study, 1 mm in the former), and both investigations found that simulated profiles underestimated dose in the penumbra tails. Discrepancies in the build-up region are not surprising, as this is traditionally the most difficult region of the PDD curve to measure or simulate [20]. As was suggested in the former paper, the

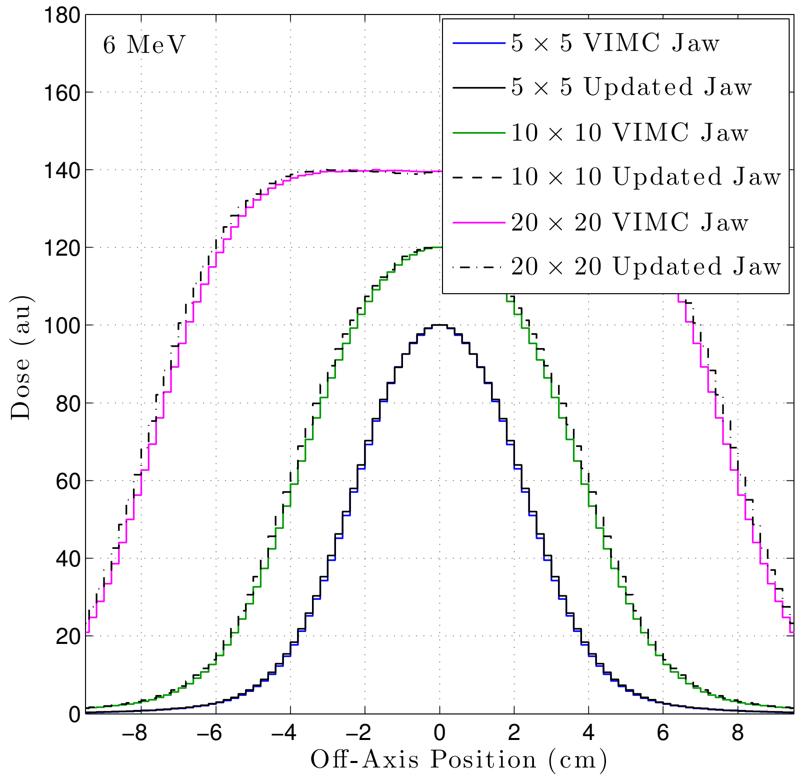

Figure 6.8: Monte Carlo dose profiles generated using the default VIMC and updated jaw models. Profiles are shown for 6 MeV at 5×5, 10×10 and 20×20 cm^2 jaws-shaped fields.

underestimate here is likely due to missing low energy electron scatter, either in simulating the field shaping components of the linear accelerator, or in the phase-space file.

Klein et al. [64] characterized electron fields generated by a Varian Trilogy accelerator under MERT delivery conditions and found field parameters consistent with those summarized in Table 6.1. This is expected, given that the dosimetric characteristics of electron fields produced by the TrueBeam and earlier Varian linear accelerators do not differ significantly [72], although, as was illustrated in Chapter 4, some differences are evident in the penumbras and there is an overall reduction of photon contamination in electron fields generated by the TrueBeam. Both of these features are reflected in the presented Monte Carlo data. EGSnrc-simulated field widths systematically underestimated measured crossline field widths, and the discrepancy between measurement and simulation increases with increasing field size, a feature also demonstrated in the Klein data. It is possible that this discrepancy is

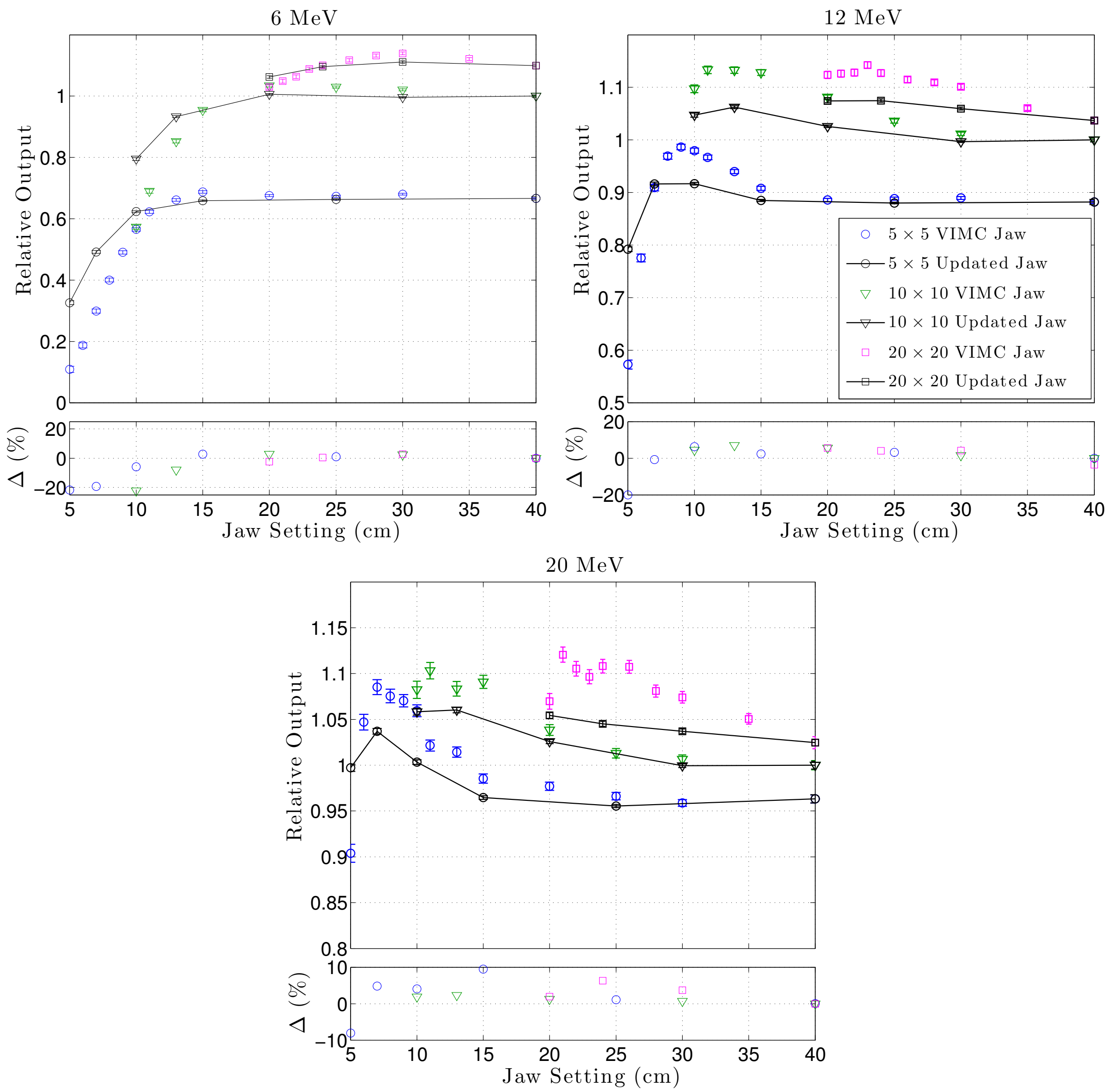

Figure 6.9: Simulated output as a function of jaw position for fixed MLC apertures using the VIMC (coloured) and updated (black) jaw models. Outputs are plotted for 6, 12 and 20 MeV electrons shaped with 5×5, 10×10 and 20×20 cm^2 MLC-apertures with varying jaw setting. Note that simulated data points are discrete and that the connecting line is intended only as a visual guide. The lower subplot indicates the percent difference between simulations, colour and symbol matching the corresponding curves in the main plot.

a result of sub-optimal modelling of the MLC leaf-end. The DYNVMLC component model used in this work was tuned for photon field simulations, and it is possible that this MLC model is not optimal for electron fields. Profile widths in the inline direction agree within 1 mm for all fields.

A difference of note between simulation and measurement is in the shoulders of the 10×10 and 20×20 cm^2 fields at 20 MeV where simulated data underestimates the measured dose. This trend seems to be specific to the 20 MeV phase-space off-axis. A similar effect is shown in Rodrigues et al. for 20 MeV electrons delivered with a 15×15 cm^2 applicator at 100 cm SSD.

The paper by Klein et al. and another by Connell et al. [22] characterize the high sensitivity of electron output to field size in the absence of applicators. As expected, this sensitivity is most pronounced at the lowest energy investigated, 6 MeV, and is evident in Figures 6.5 and 6.6, where the 6 MeV output changes up to 80% between the smallest and largest collimation settings. A similar output range was demonstrated by Klein et al. for the Trilogy at 6 MeV. In comparison, the output varies less than 15% between the smallest and largest applicator sizes at 6 MeV. For simulation of MERT and MPERT, then, accurate modelling of output dependence on field size and collimator arrangement is essential. The outputs presented in Figure 6.5 for fixed MLC-apertures and varying jaw position demonstrate excellent agreement between measurement and simulation, with all but two simulated outputs falling within 1% of measurement. The largest discrepancies of 2.3% and 1.5% occur at 12 MeV and 20 MeV, respectively, both for a 5×5 cm^2 MLC-aperture and jaw setting.

The discrepancies in Figure 6.6, where the MLC-aperture size varies, are more substantial, reaching as much as 4.0% at 6 MeV for a 5×5 cm^2 MLC-aperture. The steep slope of the 6 MeV curve in Figure 6.6 means that a 1 mm error in MLC position can result in up to a 1.8% change in output, in addition to the 0.7% measurement uncertainty described in Section 3.1.1. Figure 6.10 shows that the same discrepancy is present when the field is formed by jaws alone, which suggests that the 6 MeV phase-space may be the source of the disagreement. 12 and 20 MeV output simulations fall within 1% of measurement at small MLC-shaped field size.

Rodrigues et al. summarized applicator output factors at 100 cm SSD where the largest discrepancies occurred at 6 MeV, ranging from a 1.7% overestimate to 2.5% underestimate of measured output for a 5×5 cm^2 cut-out and 25×25 cm^2 applicator, respectively. The same trend is evident for 6 MeV in Figure 6.6 at 70 cm SSD for MLC-shaped fields, and again in Figure 6.10 at 70 cm SSD for jaw shaped fields. In Figure 6.10, the discrepancies range from a 3.5% overestimate to a 5.5% underestimate when jaws are set to 5×5 and 40×40 cm^2, respectively. Demonstration of this trend in two independent studies and its amplification under non-standard delivery conditions support the argument that at least some of the issue lies with the 6 MeV phase-space.

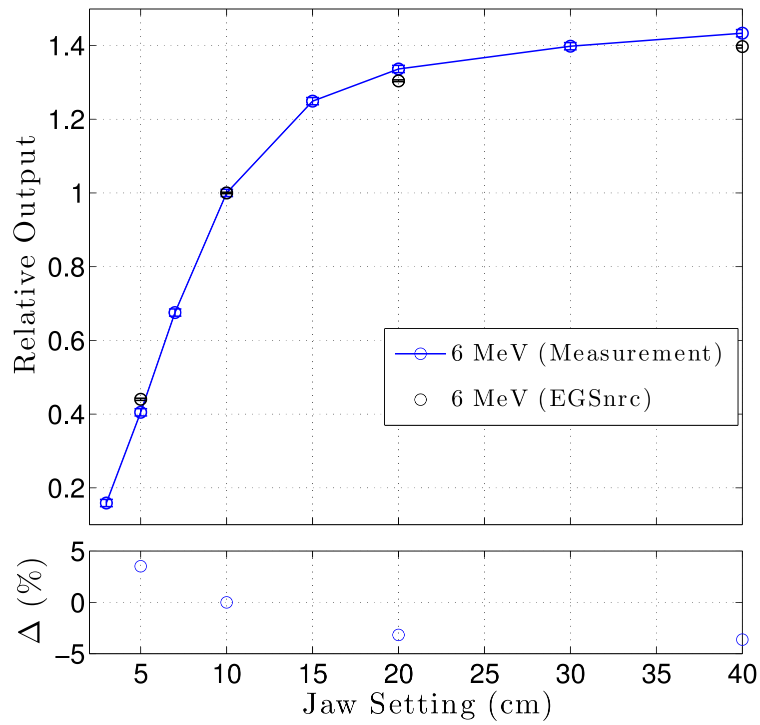

Figure 6.10: Measured and EGSnrc-simulated relative outputs as a function of jaw position for 6 MeV electrons (MLCs set to 40×40 cm^2). Note that measurements are discrete and that the connecting line is intended only as a visual guide. Percent difference between measurement and simulation is plotted in the lower panel.

In the work presented by Rodrigues et al., the jaw divergence focused on a 0.3×0.3 cm^2 spot in the source plane was modelled, but the arc trajectory of the Y-jaws was not. The authors suggested that this did not impact the accuracy of their results provided that the face of the jaws maintained the correct tilt. As can be seen in Figure 6.9, correcting for the divergence of the jaws towards the true source focus has a dramatic impact on the relative outputs of the simulation. In contrast, differences in profile and PDD shapes between the default VIMC and updated jaw models were minimal. Remarkably, the translational shift of the jaws 1.5 mm away from the central axis to account for this non-zero focus, and a 6 mm correction away from the source dramatically impacts the overall shape of the output curve.

It is worth noting that the evaluation of these output discrepancies is subjective to the choice of normalization point. Assuming that the dose calculation engine is employing appropriate particle transport parameters, discrepancies in output between measurement and simulation are due to deficiencies in either the source model (the phase-space in this case), or the accelerator model. By selecting the largest field as the reference, the largest discrepancies will occur at small field size where the most collimation is utilized. In this scenario, issues with the phase-space may be washed out by deficiencies due to collimator modelling error which would dominate. The reverse is true of choosing the smallest field as the reference. A 10×10 cm^2 field normalization point is a typical reference field in the clinic, and allows for investigation of both phase-space deficiencies and collimation modelling errors, and so was chosen as the reference field for the data sets presented in Figures 6.6 and 6.10.

Finally, the steep slopes and build-up regions at the beginning of the output curves in Figure 6.5 inform a strategic selection of jaw setting for clinical electron fields delivered with MLCs. At 6 MeV, jaws set 5 to 10 cm beyond the MLC-field setting will maximize output for efficient delivery, while a closer setting at the higher energies will accomplish the same. Note, however, that the output build-up demonstrated at 12 and 20 MeV for the 5×5 cm^2 MLC aperture may require a compromise between efficient delivery and stable output with respect to field size in order to minimize delivery errors.

6.4 Conclusions

Varian's TrueBeam electron phase-spaces have been evaluated for use in Monte Carlo simulations of fields delivered under MERT and MPERT conditions. Depth dose curves agree with measurement, within 2%/2 mm beyond the build-up region, although, without the distance to agreement, differences are as large as 7.3%. Simulated profiles underestimate the measured dose in the shoulder and tail regions, by as much as 3.5%. Most simulated outputs agree with measurement within 2.7% except at 6 MeV when the field is shaped by MLCs and the discrepancy reaches 4.0%. For the type of proof-of-concept work that is currently being done towards the implementation of MERT and MPERT, these sources are acceptable for use with existing accelerator models. Before clinical work can be performed, however, modifications must be made to the accelerator models or corrections made to the phase-space files to reduce or eliminate the existing dose and output factor discrepancies.

As mentioned in the discussion of Chapter 5, a look-up table could be implemented to correct for the remaining discrepancies in output, however, it was hypothesized that the inclusion of a backscatter correction factor may provide sufficient improvement to simulated outputs. The backscatter correction factor accounts for changes in radiation scattered from the collimating devices backwards into the monitor ion chamber as a function of field size. Techniques for measuring backscatter, as well as a method for simulating backscatter in the absence of exact schematics for the monitor chamber are presented in Chapter 7.

Chapter 7

Results & Discussion IV: Measured and simulated electron backscatter factors for the TrueBeam

7.1 Introduction

In order for Monte Carlo simulations to be clinically useful, there must be a formalism by which to translate dose per particle simulated into dose per monitor unit delivered by a linear accelerator, and to account for output changes as a function of collimation by the jaws or by the MLC. Electron output dependencies on jaw or MLC field-size are already accounted for in the explicit geometric modelling performed in many Monte Carlo systems, provided that an accurate model is being used [42]. The accelerator model presented in Chapter 6 models changes in relative output to within 4% using Varian's electron phase-space source files. The change in output due to backscatter into the monitor chamber, on the other hand, requires additional calculations be performed in order to maintain calibration accuracy for calculations under varied field collimation and size.

To calculate the backscatter factor, S_b, Verhaegen et al. [110] created a complete accelerator model of a Varian 2100C linear accelerator including a carefully detailed model of the monitor ionization chamber, referencing characterization of the chamber foils by Duzenli et al. [28] in addition to direct measurements of the monitor chamber to verify its dimensions. Simulations were performed in two parts: in the first part, an intermediate phase-space was scored just below the monitor chamber and the forward dose component in the monitor chamber was recorded. In the second part, the remainder of the linear accelerator was modelled using the intermediate phase-space as the source, and additional dose delivered to the monitor chamber due to backscattered radiation was recorded. These simulations were compared with measurements of backscatter acquired by integrating the machine's dose rate over a fixed time interval with the dose servo turned off. For a limited set of measurements, simulated and measured backscatter from the secondary collimating jaws were found to agree within combined measurement and statistical uncertainties of 1.5% for square fields of 6, 12 and 20 MeV electrons fields, as well as for 6 and 10 MV photon fields.

Using the same technique to simulate forward and backscattered dose components in the monitor chamber, Popescu et al. [85] used simulated values of S_b to perform absolute Monte Carlo dose calculations of photon fields. Absolute dose simulated for jaw shaped fields, fields completely blocked by the MLC and MLC sliding windows agreed with measurement to within 1.3%. Additionally, the authors argued that the geometry of the volume used to model the monitor chamber need not match the geometry of the true monitor chamber, provided that the dose values scored in the virtual volume are proportional to those that would be measured in the true volume.

Simulating the forward dose scored in the monitor chamber typically requires a complete linear accelerator model that includes the field-independent components of the head geometry. In the case of the TrueBeam linear accelerator, Varian has kept this information proprietary and, instead, has released the phase-space source files discussed in Chapter 6, scored above the secondary collimating jaws as in Figure 6.1. Zavgorodni et al. [116] presented a technique for determining the forward dose component for Varian's photon phase-space files based on a "virtual" monitor chamber and measured values of S_b for photon fields. Simulated values of S_b determined using these virtual forward dose components agreed with measurement within 0.1%.

Measuring S_b presents its own challenges. Verhaegen et al. [110] and Zavgorodni et al. [116] described different approaches to measuring photon backscatter. In Verhaegen et al., charge was collected in the bremsstrahlung target of the Clinac 2100 using the TARGET I port and assessed, per monitor unit, as a function of jaw position, while in Zavgorodni et al., narrow collimators and a small detector were used to measure machine output per monitor unit for the TrueBeam, independent of collimation and room scatter. Neither of these approaches are appropriate for electron fields as there is no bremsstrahlung target in electron field generation and electron scatter is unavoidable inside the narrow collimators used for the small ionization chamber measurements.

Verhaegen et al. addressed the challenge of measuring electron backscatter by designing a measurement system that integrated charge collected in the monitor chamber over a fixed period of time. With the dose servo turned off, changes in the dose rate were assessed as a function of field size. While individual measurements were acquired with sufficient precision in 30 seconds, this approach required the design and fabrication of specialized electronics.

In normal operation, the TrueBeam control systems maintain a constant dose rate, regardless of backscatter, therefore, the time to deliver a fixed number of monitor units is constant, regardless of jaw setting. By turning off the dose and pulse forming network (PFN) servos while operating the TrueBeam in Service mode, the dose rate is allowed to fluctuate with changes in backscatter, therefore, the time to deliver a requested number of monitor units will also change with backscatter.

In this work, both the change in dose rate and the time to deliver a fixed number of monitor units were exploited to measure backscatter into the monitor chamber as a function of collimation style and setting without the need for specialized electronics. These techniques were developed to assess electron backscatter for the Varian TrueBeam, but can be extended to any accelerator with similar dose rate control systems. As well, the technique presented by Zavgorodni et al. [116] for determining the forward dose component in a virtual monitor chamber for simulations of S_b was extended to electron fields.

7.2 Materials and methods

7.2.1 Measured backscatter factors

The formal definition of S_b is presented in Section 2.3.3. With the dose rate and PFN servos turned off, dose rate is allowed to fluctuate with changes in backscatter and S_b is described by Equation 2.9. This work uses a 40×40 cm^2 field as the reference, and therefore assumes absolute dose calibration is performed in Monte Carlo based on a 40×40 cm^2 field. This selection was made as an open field is expected to have the smallest backscatter contribution to the monitor chamber dose, so changes relative to the reference can be interpreted, uniformly, as an increase in backscatter. The values of S_b reported can be modified for use with the more conventional 10×10 cm^2 calibration field by dividing each value of S_b by the value of S_b for a 10×10

cm^2 field. Had a 10×10 cm^2 references been chosen in this work, any disagreement between measured and simulated values of S_b would be divided between either end of the S_b versus field size curve. By selecting one end of this curve as the reference, any differences between measurement and simulation can be quantified in full at the other end of the curve. This is shown schematically in Figure 7.2.

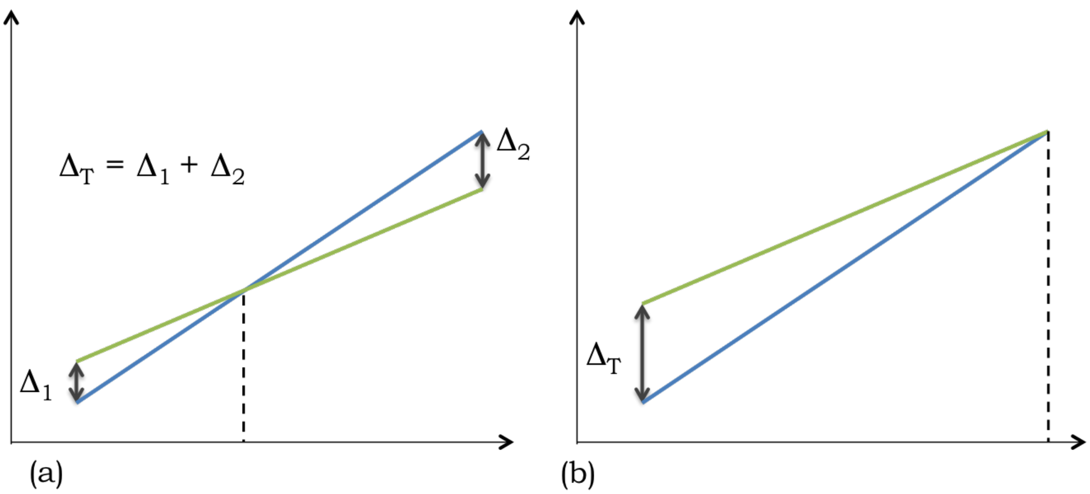

Figure 7.1: Comparison of normalization strategies for S_b curves. The curves in (a) have been normalized to a point in the middle of the curve, 10×10 cm^2 for example, while the curves in (b) have been normalized to one end of the curve, in the case presented here, 40×40 cm^2.

Delivery timing method

With the dose and PFN servos turned off, delivery time, t, and monitor units delivered, MU, (9999 MU requested at the nominal dose rate 1000 MU/min) were recorded to assess an average dose rate for the delivery. S_b was calculated as

$$S_b = \frac{MU'_{\text{avg},40}}{MU'_{\text{avg,field}}} = \frac{MU_{40}/t_{40}}{MU_{\text{field}}/t_{\text{field}}}. \tag{7.1}$$

Square jaw settings between 1×1 and 40×40 cm^2 were assessed, as well as rectangular jaw settings ranging from 5×40 to 40×5 cm^2.

Without the dose rate control systems engaged, the output of the TrueBeam drifted over time. To account for this drift, time to deliver a reference field with jaws set at 40×40 cm^2 was measured before and after measuring the time to deliver each field of interest. The average of these reference measurements was used to normalize the field of interest measurement. The error in S_b was determined by propagating the uncertainty in measured values of time and monitor units delivered, which were determined by the precision of the readings. In all cases, the resulting uncertainty in S_b was less than 0.07%.

Dose rate sampling method

The delivery timing technique described above requires about 1.5 hours to acquire 5 data points. Given a sufficiently stable dose rate, the instantaneous dose rate for a given field can also be sampled to determine backscatter as a function of field size in a more efficient manner. A second set of dose rate measurements was performed by sampling the instantaneous dose rate with the dose and PFN servos turned off. After running beam for about two minutes to avoid warm up effects, dose rates at six jaw settings were recorded in sequence, concluding with the reference 40×40 cm^2 field. This was done four times without beam interruption and the average value for each jaw setting was calculated to determine S_b as

$$S_{\mathrm{b}} = \frac{MU'_{\mathrm{avg},40}}{MU'_{\mathrm{avg,field}}}. \tag{7.2}$$

With the nominal dose rate set to 1000 MU/min, the entire data set for one energy was collected in less than 10 minutes. These measurements were done for square jaw settings between 1×1 and 40×40 cm^2 and for rectangular fields ranging from 5×40 to 40×5 cm^2. For the rectangular study, six data sets were acquired to span the range of jaw positions requiring an hour of data acquisition per energy.

On the time scale of a single measurement, with the dose and PFN servos turned off, there was noise in the dose rate signal which was quantified by taking the standard error of the dose rate samples. This was added in quadrature with the measurement error associated with the precision of each reading and used to quantify the uncertainty in each determination of dose rate. These errors were propagated in order to determine the uncertainty in each value of S_b which were no greater than 0.2%.

7.2.2 Simulated backscatter factors

Absolute dose calculations can be performed with Monte Carlo by using an appropriate conversion between dose per particle simulated and dose per monitor unit delivered. Popescu et al. [85] presented such a conversion that included a backscatter correction factor

$$D_{xyz}^{\mathrm{abs}} = D_{xyz}\left(\frac{D_{\mathrm{ch}}^{\mathrm{forward}} + D_{\mathrm{ch}}^{\mathrm{back}}(\mathrm{ref})}{D_{\mathrm{ch}}^{\mathrm{forward}} + D_{\mathrm{ch}}^{\mathrm{back}}(\mathrm{field})}\right)\frac{D_{\mathrm{cal}}^{\mathrm{abs}}}{D_{\mathrm{cal}}} = D_{xyz} \cdot S_{\mathrm{b}} \cdot \frac{D_{\mathrm{cal}}^{\mathrm{abs}}}{D_{\mathrm{cal}}} \tag{7.3}$$

where

- D_{xyz}^{abs} is the absolute dose, in Gy/MU, measured or calculated at the coordinates (x, y, z)
- D_{xyz} is the dose per incident particle, in Gy/particle, scored in the voxel with coordinates (x, y, z)
- $D_{\mathrm{cal}}^{\mathrm{abs}}$ is the absolute dose, in Gy/MU, measured at a reference point in the chosen calibration geometry
- D_{cal} is the dose per incident particle, in Gy/particle, scored in the voxel corresponding to a reference point in the chosen calibration geometry
- $D_{\mathrm{ch}}^{\mathrm{forward}}$ is the dose scored in the monitor chamber model, in Gy/particle, due to forward directed radiation
- $D_{\mathrm{ch}}^{\mathrm{back}}$ is the dose scored in the monitor chamber model, in Gy/particle, due to backscattered radiation
- **ref** refers to the reference field used in the chosen calibration geometry. Typically this is a 10×10 cm^2 field, but in this work, a 40×40 cm^2 field is used
- **field** refers to the field of interest.

From this, we can define $\mathrm{S_b}$ as

$$S_{\mathrm{b}} = \frac{(D_{\mathrm{ch}}^{\mathrm{forward}} + D_{\mathrm{ch}}^{\mathrm{back}}(\mathrm{ref}))}{(D_{\mathrm{ch}}^{\mathrm{forward}} + D_{\mathrm{ch}}^{\mathrm{back}}(\mathrm{field}))}. \tag{7.4}$$

The forward directed dose contribution to the monitor chamber, $D_{\mathrm{ch}}^{\mathrm{forward}}$, can be calculated directly in a complete accelerator simulation by dividing the simulation into two parts, one that terminates in a phase-space scored just below the monitor chamber, and a second that carries on using that phase-space as its source. In the case of the TrueBeam, the photon and electron phase-space source files published by Varian are scored below the monitor chamber, and $D_{\mathrm{ch}}^{\mathrm{forward}}$ cannot be calculated directly. Zavgorodni et al. showed, however, that $D_{\mathrm{ch}}^{\mathrm{forward}}$ can be computed by rearranging equation 7.4:

$$D_{\mathrm{ch}}^{\mathrm{forward}} = \frac{D_{\mathrm{ch}}^{\mathrm{back}}(\mathrm{ref}) - S_{\mathrm{b}} \times D_{\mathrm{ch}}^{\mathrm{back}}}{S_{\mathrm{b}} - 1}. \tag{7.5}$$

By using simulated values of $D_{\mathrm{ch}}^{\mathrm{back}}$ and measured values of $\mathrm{S_b}$, a value for $D_{\mathrm{ch}}^{\mathrm{forward}}$ can be predicted and applied to any future Monte Carlo simulation. Then, only $D_{\mathrm{ch}}^{\mathrm{back}}$ need be calculated in order to determine the specific $\mathrm{S_b}$ factor for an arbitrary simulation, which can be done quickly and conveniently in BEAMnrc. This was applied successfully for photon phase-space sources in the paper by Zavgorodni et al. and its application for electron phase-spaces is presented here using both methods for measuring $\mathrm{S_b}$.

EGSnrc/BEAMnrc

Monte Carlo backscatter simulations were performed using BEAMnrc [94]. The accelerator model used includes a monitor chamber, anti-backscatter plate, jaws and MLC modelled using the component modules CHAMBER, SLABS, JAW and DYNVMLC. The jaw model included the arc-trajectory of the Y-jaws, as well as the tilting of the X-jaw faces to match the beam divergence as described in the TrueBeam Monte Carlo Data Package. A block diagram of the beam model is shown in Figure 7.2.

Dose in the monitor chamber was scored by setting `DOSE_ZONE` = 1 for each air layer, the sum of which was then printed out in the output (.egslst) file. The number of particles used in each simulation ranged between 1 and 5 million depending on the energy and field size, resulting in statistical uncertainties between 0.4% and 1.2% for jaw-shaped fields, and between 0.7% and 1.6% for MLC-shaped fields. Simulation times ranged between 0.5 and 10 CPU hours run on a single core. Cut-off energies `PCUT` = 0.01 MeV and `ECUT` = 0.521 MeV were used. Phase-spaces for 6, 12 and 20 MeV electron fields were downloaded from the Varian website and ten of each were summed to form the sources used in this work.

Because Varian has not released specifications for the monitor chamber used in the TrueBeam, a model of the monitor chamber used in the Clinac 21EX accelerator was used with the addition of an anti-backscatter foil on its exit surface. Following the conclusion of this work, email correspondence with Varian representatives revealed

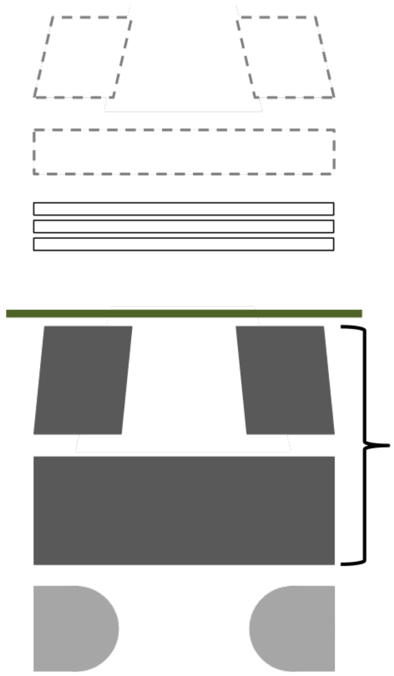

Figure 7.2: Block representation of the component modules used to simulate backscatter for the TrueBeam. Note that the component modules outlined in dashed lines were not included in the model and are shown here for reference only.

that the anti-backscatter foil is not present during electron beam delivery. For this reason, the values of $D_{\mathrm{ch}}^{\mathrm{back}}$ and $D_{\mathrm{ch}}^{\mathrm{forward}}$ scored and calculated in this work are not reflective of the true dose deposited in the TrueBeam's monitor chamber. This is consistent with the approach described in Zavgorodni et al., and the recommendation in Popsecu et al. that the exact monitor chamber specifications are not required for absolute dose calculations using Equation 7.3.

VirtuaLinac

The backscatter factors for jaw-shaped fields simulated using BEAMnrc were also simulated by Dr. Magdalena Bazalova-Carter using VirtuaLinac (version 1.2.5, Varian Medical, Palo Alto, CA) as an independent second check. VirtuaLinac is a GEANT4-based [1] Monte Carlo simulation package administered by Varian through a pay-per-use web-platform. Simulations are based on the true internal geometry of the accelerator without disclosing this information to the user, and these geometries can be modified proportionally. Rodrigues et al. [88] published beam energy, energy spread and beam size parameters that were used for the simulations presented in this work, and input parameters are summarized in Table 7.1. The Foil 1 thickness and ionization chamber thickness were proportionally modified by the values specified in Table 7.1 compared to specification.

Table 7.1: VirtuaLinac simulation parameters for 6, 12 and 20 MeV electrons.

	Energy (MeV)	Energy spread (MeV)	Spot Size (mm)	Foil 1 thickness factor	Ionization chamber metal thickness factor
6 MeV	6.84	0.6	0.7	1.07	0.64
12 MeV	13.18	0.7	0.7	1.02	0.64
20 MeV	21.80	1.0	0.7	1.02	0.64

Jaw settings were specified directly while a 40×40 cm^2 MLC setting was specified using a Varian Developer Mode .xml file. VirtuaLinac simulations used the G4EmStandardPhysics_option4 physics list with a 100-μm range cutoff. The total dose scored in the monitor chamber for a particular field was recorded and backscatter factors were calculated as the ratio of the reference 40×40 cm^2 field dose over the field-of-interest dose. 10^7 particles were simulated for each field, requiring about 32 CPU hours.

7.2.3 MLC backscatter

Photon backscatter from the multileaf collimator (MLC) into the monitor chamber is regarded as negligible [119], and given that the relative increase in backscatter is similar for photons and electrons [110], the same conclusions may be drawn for electrons. To show this definitively, measurements and simulations of backscatter due to the multileaf collimator were performed and compared. MLC fields ranging in size from 1×1 to 40×40 cm^2 were delivered at 6, 12 and 20 MeV with jaws set to 40×40 cm^2 and the dose and PFN servos turned off. Changes in dose rate were measured using the delivery timing technique and a modified dose rate sampling technique. Because the MLC apertures were defined in separate files for each field-size, apertures could not be changed without interrupting the beam. In the modified dose rate sampling measurements, each aperture was delivered on its own with a 40×40 cm^2 reference field sampled before and after. For each measurement, the beam was run for about two minutes to warm up and stabilize, after which, four samples of the dose rate were recorded, each about 30 seconds apart. The average dose rate was used to calculate S_b as in Equation 7.2.

7.3 Results

7.3.1 Measured backscatter

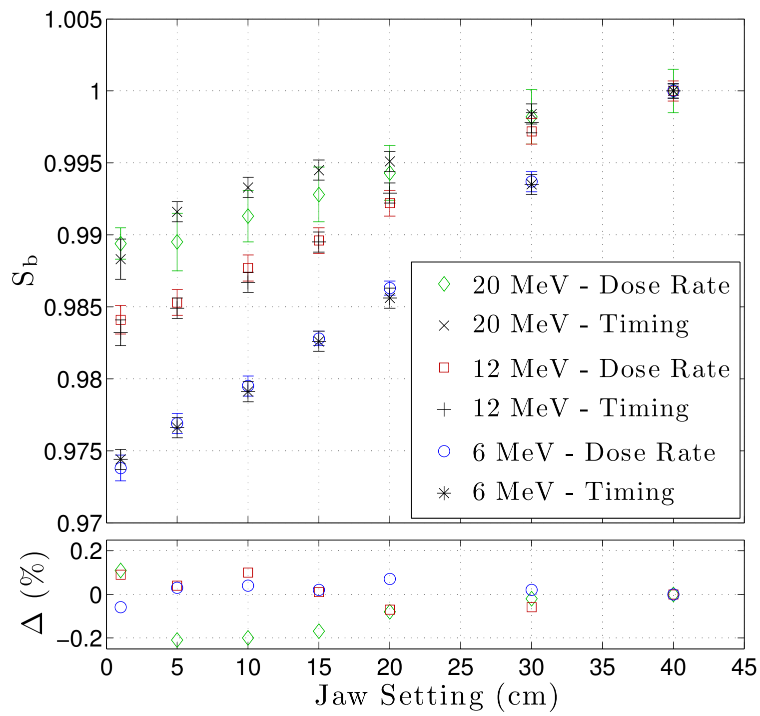

Figure 7.3: Comparision of measured backscatter factors, S_b, for square, jaw-shaped, 6, 12 and 20 MeV electron fields. Backscatter factors determined by sampling instantaneous dose rate are displayed as open points while backscatter factors determined by timing a 9999 MU delivery are displayed as black line-based points.

Figure 7.3 plots backscatter factors, S_b, for square, jaw-shaped fields at 6, 12 and 20 MeV measured using the dose rate sampling and delivery timing techniques. Differences between measured data sets are within 0.10% for 6 and 12 MeV, and within 0.21% at 20 MeV. All but two data points agree within measurement uncertainty. Backscatter is greatest at 6 MeV where $S_b = 0.974$ for a 1×1 cm^2 jaw setting corresponds to a 2.6% change in dose rate due to backscatter compared to the 40×40 cm^2 reference field. At 12 and 20 MeV, a 1×1 cm^2 jaw setting corresponds to a 1.7% and 1.2% change in dose rate, respectively.

Figure 7.4 plots backscatter factors for rectangular fields measured using the dose rate sampling and delivery timing techniques. Differences in measured values are within 0.21%. Backscatter is most sensitive to the position of the Y-jaw at 6 MeV, where the change in dose rate due to backscatter into the monitor chamber is as much as 2.3% when the field is 40×5 cm^2 compared to a 40×40 cm^2 field. The analogous change for X-jaws is only 0.8% for a 5×40 cm^2 field. At 12 MeV, the range of the Y- and X-jaws are 1.4% and 0.6%, respectively, while at 20 MeV, the jaw ranges are 0.9% and 0.4%, respectively.

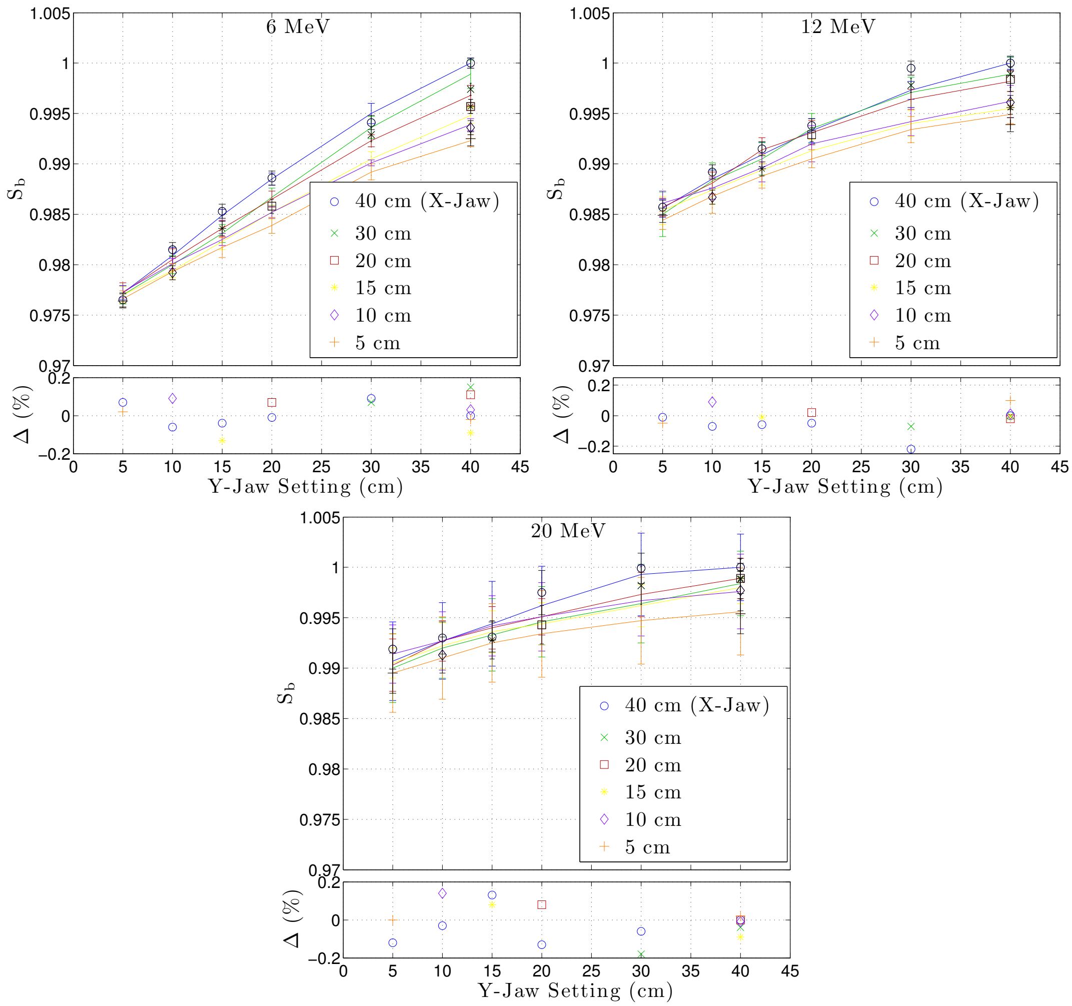

Figure 7.4: Comparison of measured backscatter factors, S_b, for rectangular, jaw-shaped, 6, 12 and 20 MeV electron fields. Backscatter factors determined by dose rate sampling are displayed as connected by a line while backscatter factors determined by delivery timing are displayed as black, free-floating points.

The drift in dose rate was investigated by plotting the reference dose rate measurements acquired using the timing technique against time, shown in Figure 7.5. From the slope of each curve, the drift in dose rate for a 10 minute delivery was found to be between 0.2% and 0.3%.

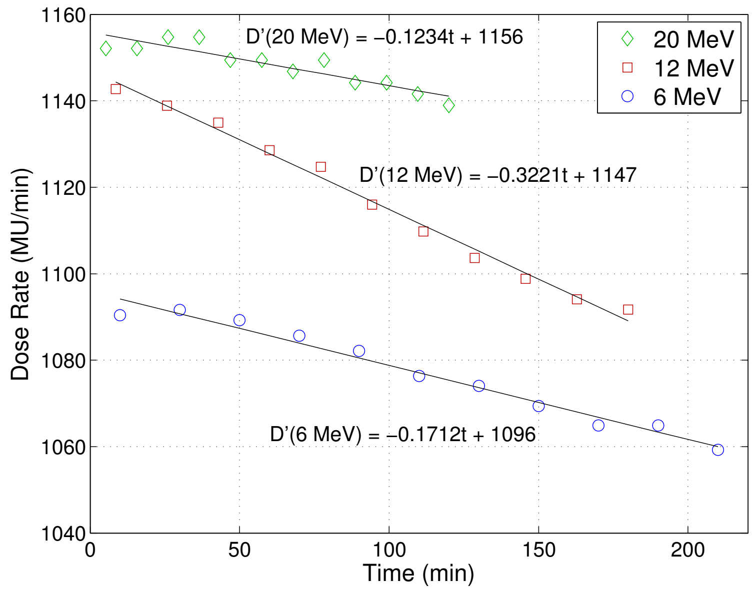

Figure 7.5: Drift in dose rate with dose and pulse forming network servos turned off. Data is shown for 40×40 cm^2 jaw-shaped fields at 6, 12 and 20 MeV measured using the timing technique.

7.3.2 Simulated backscatter

The values of S_b for square fields presented in Figure 7.3, along with simulated backscatter dose, were used with Equation 7.5 to calculate the forward directed radiation dose deposited in the virtual monitor chamber for each jaw setting. An average forward dose component was calculated for each energy and the results are summarized in Table 7.2. Measurement-based uncertainties in S_b and Monte-Carlo reported uncertainties in backscattered dose were included in the error propagation to determine uncertainty in the forward dose component.

Table 7.2: Virtual monitor chamber forward dose components as determined using equation 7.5.

Energy (MeV)	Forward Component ($\times 10^{-12}$ Gy/particle)
6	2.417 ± 0.006
12	3.223 ± 0.006
20	3.089 ± 0.009

Using the forward dose components in Table 7.2 and simulated values of backscatter into the monitor chamber, values of S_b were calculated and are compared with measurement in Figures 7.6 for square fields and 7.7 for rectangular fields. Differences between measurement and simulation are within 0.17%. Backscatter dependence on the Y- and X-jaws, independently, agree within 0.1% of the measured ranges given in Section 7.3.1.

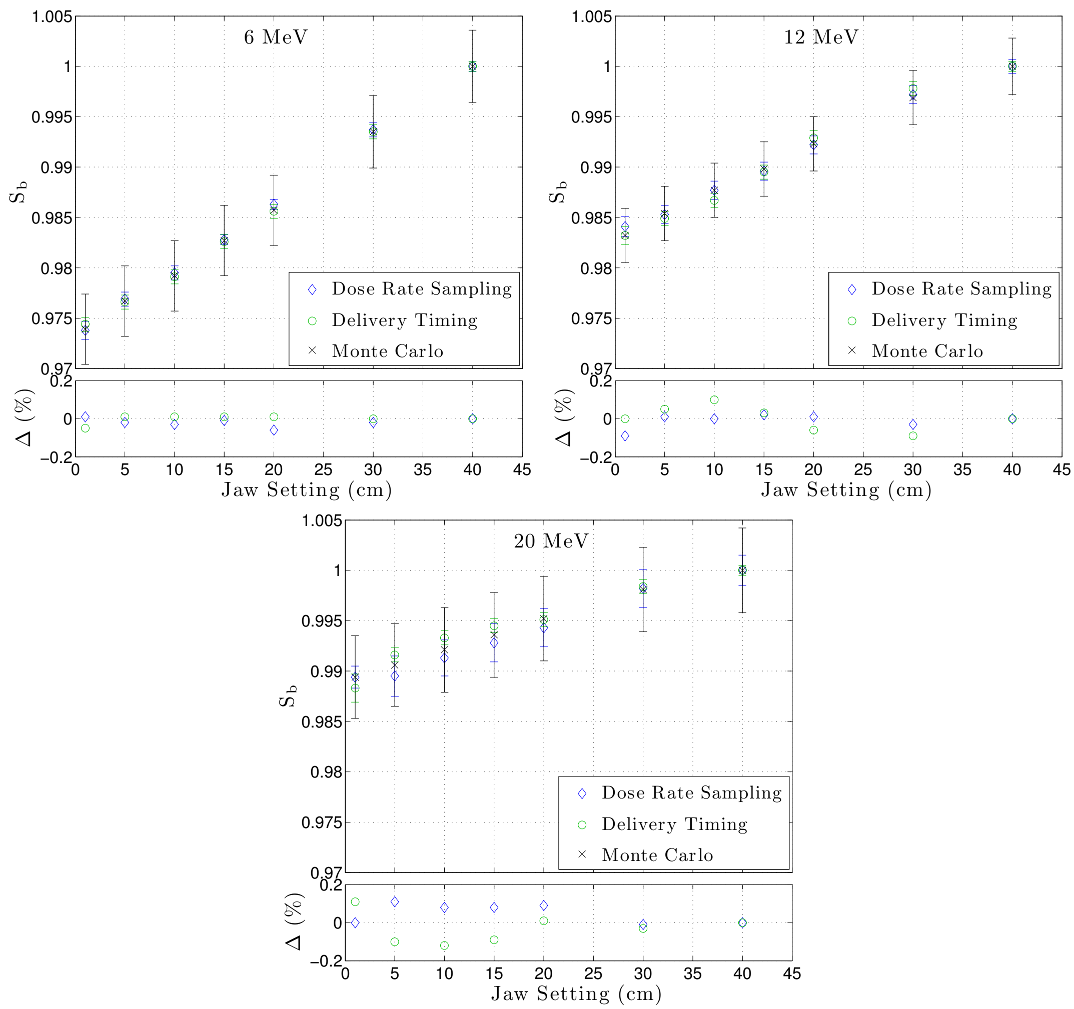

Figure 7.6: Measured and BEAMnrc Monte Carlo simulated backscatter factors, S_b, for square, jaw-shaped electron fields at 6, 12 and 20 MeV.

Simulated backscatter factors were applied to the simulated output factors presented in Figure 6.10 and the resulting outputs were compared, again, against measurement in Figure 7.8. In this figure, a 10×10 cm^2 field was chosen as the reference, so that values of S_b were also normalized to 10×10 cm^2. At each point, agreement between measurement and simulation is improved with the inclusion of the backscatter factor. At 40×40 cm^2, the difference between measurement and simulation is

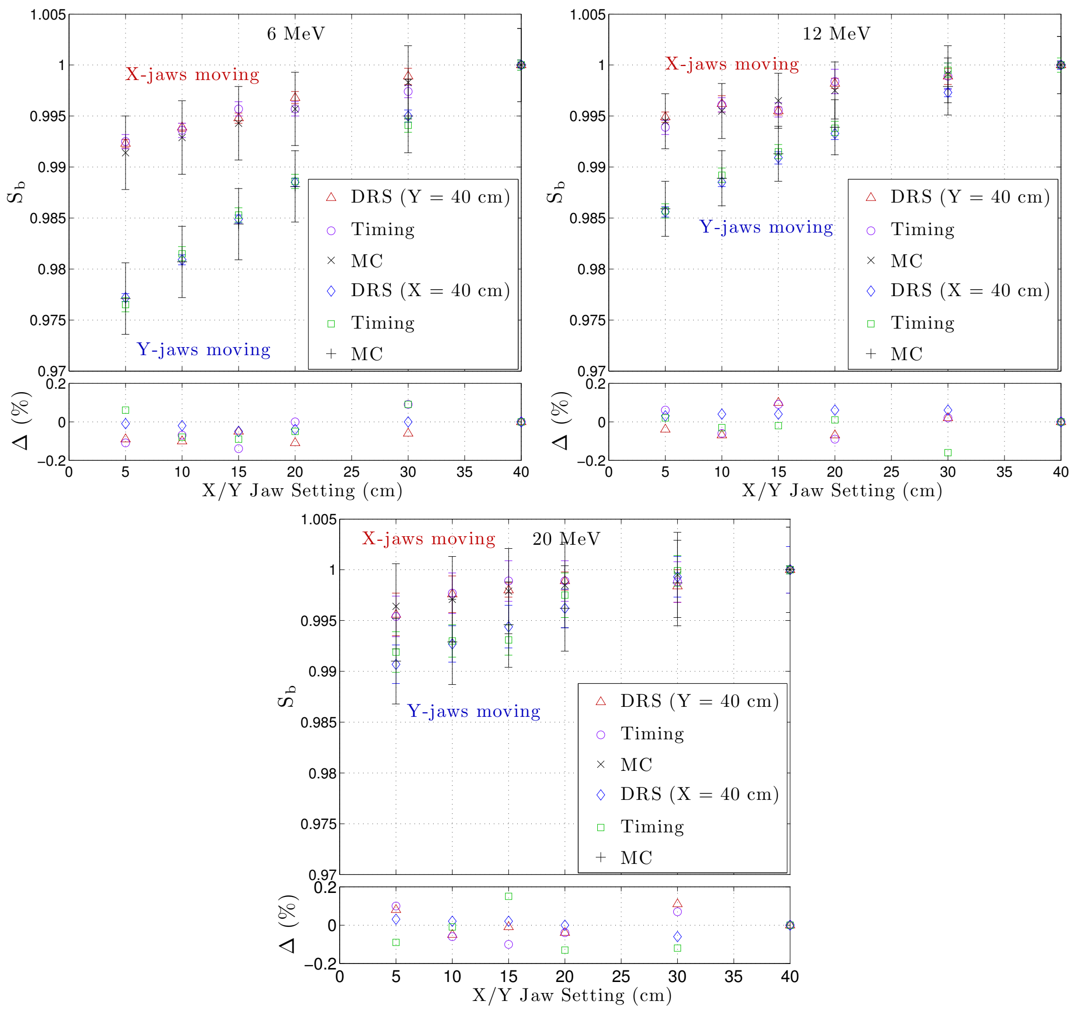

Figure 7.7: Measured and BEAMnrc Monte Carlo simulated backscatter factors, S_b, for rectangular, jaw-shaped, 6, 12 and 20 MeV electron fields. In each panel, the top curve shows backscatter dependence on X-jaw position (Y-jaw set to 40 cm) while the lower curve shows backscatter dependence on Y-jaw position (X-jaw set to 40 cm).

reduced to 0.7% compared to 3.7% without correction.

VirtuaLinac

Figure 7.9 compares backscatter factors simulated by BEAMnrc and by VirtuaLinac. At 6 MeV, BEAMnrc and VirtuaLinac backscatter factors agree within 0.06% while at 12 and 20 MeV, discrepancies reach 0.19%. While these differences fall within simulation uncertainty, BEAMnrc consistently predicts values of S_b that are closer to one than VirtuaLinac.

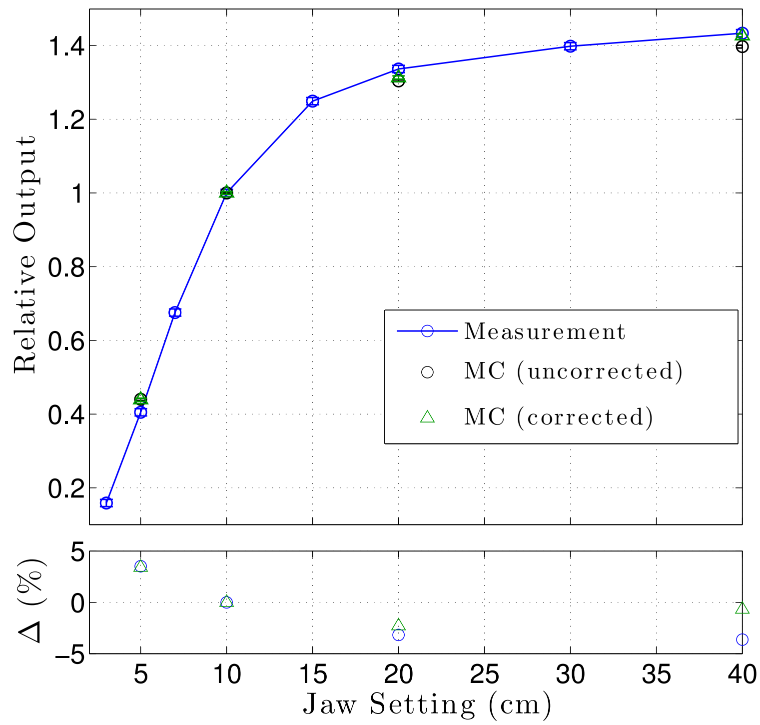

Figure 7.8: Measured and EGSnrc-simulated relative outputs as a function of jaw position for 6 MeV electrons (MLCs set to 40×40 cm^2) with and without simulated correction for backscatter effects. Note that measurements are discrete and that the connecting line is intended only as a visual guide. Percent difference between measurement and simulation is plotted in the lower panel.

7.3.3 MLC backscatter

Figure 7.10 plots values of S_b measured using the delivery timing and dose rate sampling techniques for MLC-shaped fields. Differences between measurement techniques are up to 0.41%. These measured values are then compared to Monte Carlo simulation in Figure 7.11. Differences between simulation and measurement are as great as 0.4%, however, most measured and simulated values fall within experimental uncertainty. From the Monte Carlo prediction, the largest change in backscatter should occur at 6 MeV, where the backscatter into the monitor chamber increases by 0.3% for a 1×1 cm^2 field.

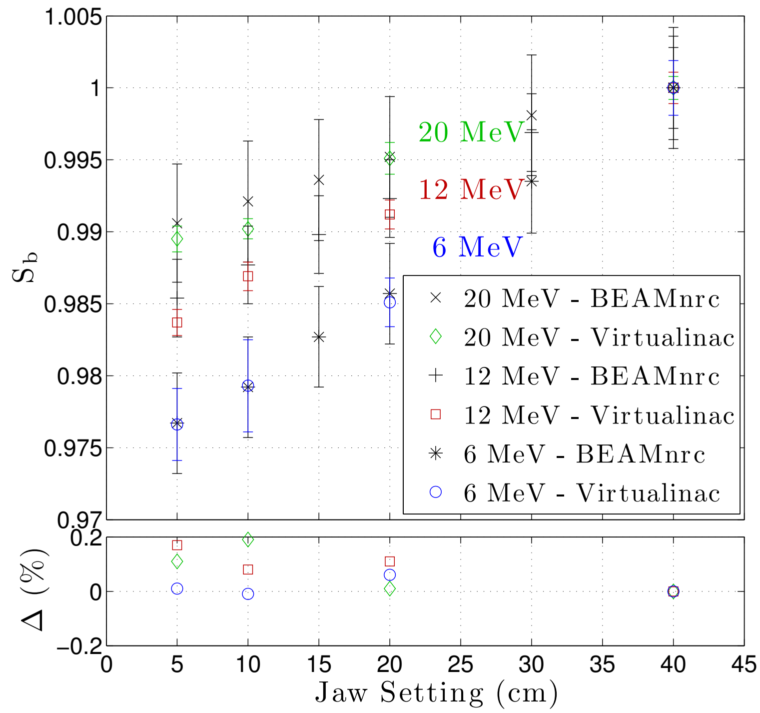

Figure 7.9: Backscatter factors, S_b, simulated by BEAMnrc and VirtuaLinac for square, jaw-shaped electron fields at 6, 12 and 20 MeV.

7.4 Discussion

This study is the first to measure backscattered radiation in the monitor chamber for TrueBeam electron fields, as well as the first to provide a framework for including backscatter corrections in absolute Monte Carlo electron dose calculations that use electron phase-space source files provided by Varian. Additionally, users who have the geometric specifications for the monitor chamber used in the Clinac series accelerators can use the forward dose contributions listed in Table 7.2 in concert with Equation 7.4 and their own simulation of backscattered monitor chamber dose to determine field-specific backscatter factors independently.

Table 7.3 summarizes the range of measured and simulated backscatter factors by energy. The largest increase in backscatter relative to a 40×40 cm^2 field, 2.6%, occurred at 6 MeV for the smallest jaw size investigated, 1×1 cm^2. Klevenhagen et al. [65] showed that for electron energies between 4.6 MeV and 33 MeV, backscatter decreases with increasing energy. Comparing the TrueBeam to data published on the Clinac 2100C, the largest measured increase in backscatter relative to a 40×40 cm^2 field, 2.1%, also occurred for the smallest jaw size investigated at 6 MeV, in this

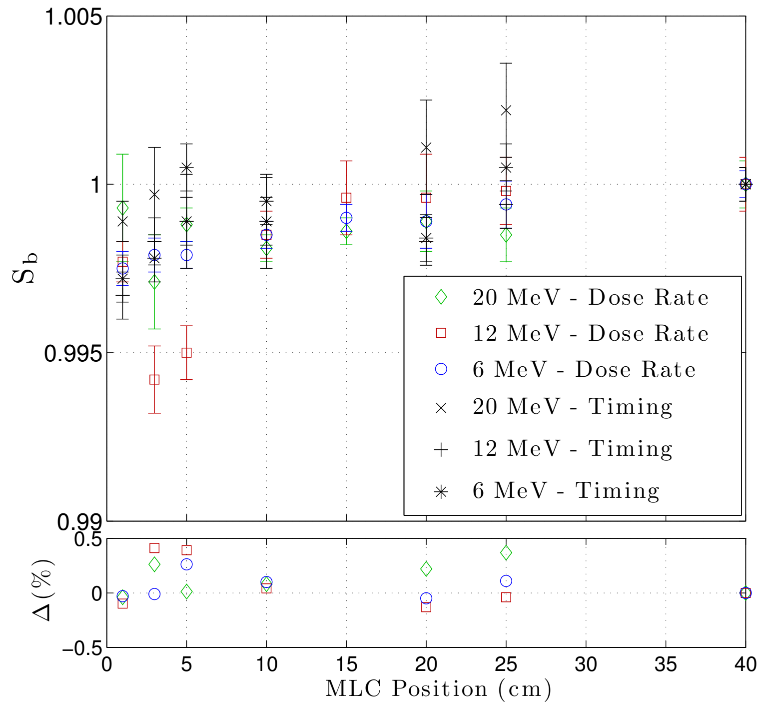

Figure 7.10: Comparision of measured backscatter factors, S_b, for symmetric, MLC-shaped, 6, 12 and 20 MeV electron fields. Backscatter factors determined by dose rate sampling are displayed as open points while backscatter factors determined by timing a 9999 MU delivery are displayed as black line-based points.

case, 0.5×0.5 cm^2 [110]. These factors are comparable to the measured increase in backscatter for photons due to jaws on the Clinac 2100C (2.0-2.9%) and the Clinac 21EX (2.0 - 2.5%), but larger than the increase measured for TrueBeam photons (1.0-1.5%) [110, 116], likely due, in part, to the addition of the anti-backscatter plate for photon beam delivery.

Overall, agreement between measured and simulated values of S_b was very good. Differences of up to 0.21% between measured and simulated backscatter due to the jaws was well within measurement uncertainty, which was, at most, 0.4%. In comparison, differences between measurement and Monte Carlo reported by Verhaegen et al. were up to 0.9%, although this fell within the reported measurement uncertainty of 1%. Additionally, inclusion of backscatter factors in simulations of output as a function of jaw setting improved agreement with measurement by as much as 3%, as demonstrated in Figure 7.8.

For backscatter due to the MLC, measured and simulated values agreed within 0.35%, again, within measurement uncertainty, however, in half of the MLC field sizes

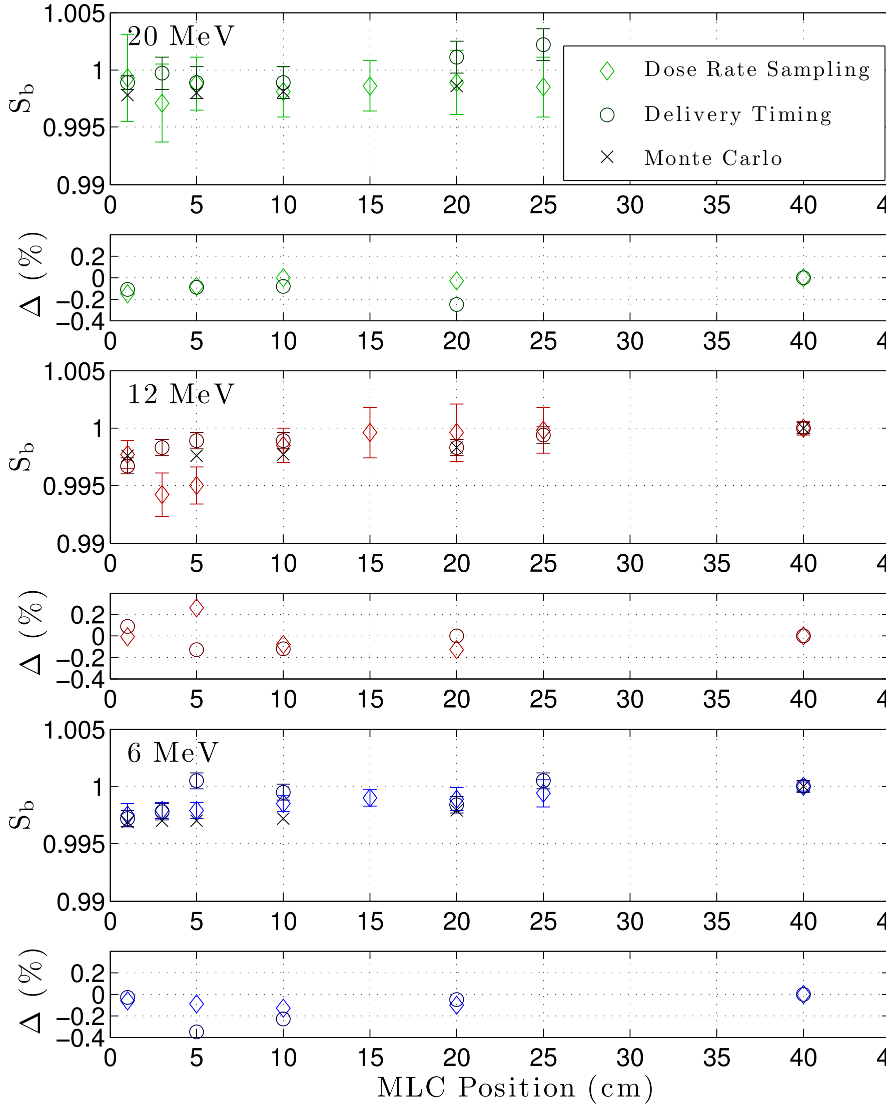

Figure 7.11: Measured and BEAMnrc Monte Carlo simulated backscatter factors, S_b, for symmetric, MLC-shaped, 6, 12 and 20 MeV electron fields.

investigated at 12 MeV and nearly all of the MLC field sizes investigated at 20 MeV, measurement uncertainty was large and neither measurement technique was sensitive enough to definitively conclude a backscatter effect at all. Monte Carlo simulations predicted backscattered dose contributions of 0.3%, 0.2%, and 0.2% for a 1×1 cm^2 field at 6, 12 and 20 MeV, respectively. This amount of backscatter is well within recommended machine output variation limits [63], and therefore, S_b from MLCs may be ignored.

Measurement fidelity using the dose rate sampling technique degraded with in-

Table 7.3: Measured and BEAMnrc Monte Carlo simulated backscatter factors, S_b, for a square 1×1 cm^2 field shaped by either jaws or MLCs at 6, 12 and 20 MeV. Uncertainty is given in brackets.

Energy	Dose Rate Sampling	Delivery Timing	Monte Carlo
		Jaws	
6 MeV	0.974 (0.001)	0.974 (0.001)	0.974 (0.004)
12 MeV	0.984 (0.001)	0.983 (0.001)	0.983 (0.003)
20 MeV	0.989 (0.001)	0.988 (0.001)	0.989 (0.004)
		MLC	
6 MeV	0.998 (0.001)	0.997 (0.001)	0.997 (0.004)
12 MeV	0.998 (0.001)	0.997 (0.001)	0.998 (0.003)
20 MeV	0.999 (0.004)	0.999 (0.001)	0.998 (0.004)

creasing energy due to a decrease in output stability. Delivery timing measurements were far less sensitive to dose rate variability, however, after long periods of running high energy beam, the long term output stability degraded and the standard deviation of repeated reference measurements reached 0.7%. A large number of monitor units were delivered to minimize the impact of precision uncertainty in the time and monitor unit readings; by delivering half as many monitor units for 20 MeV beams and scheduling data acquisition over a number of days, this standard deviation was reduced to 0.3%. This reduction was still insufficient to provide the sensitivity required to measure backscatter from the MLCs in a significant way.

Values of S_b simulated in BEAMnrc using the inferred monitor chamber forward dose component agreed well with VirtuaLinac simulations, within 0.19%. BEAMnrc systematically predicted less of a backscatter contribution to the monitor chamber than VirtuaLinac, but not beyond simulation uncertainty. Because VirtuaLinac is based on the true, proprietary geometry of the TrueBeam accelerator head and, specifically, the monitor chamber, agreement between BEAMnrc and VirtuaLinac is additional verification that the geometry of the modelled monitor chamber is not critical in these calculations.

Dose rate drift over the course of a 10 minute measurement was on the order of 0.2% or 0.3%. Most of this drift, however, was accounted for in repeated measurement of the reference 40×40 cm^2 field. Any residual drift error not accounted for in this way is expected to be negligibly small.

7.5 Conclusions

Electron backscatter factors have been measured for the Varian TrueBeam Linac without specialized electronics, and these values have been used to infer forward dose in a virtual monitor chamber for Monte Carlo calculations of absolute electron dose using phase-space source files provided by Varian. Backscatter from the jaws was shown to contribute as much as 2.6% of the monitor chamber signal, therefore, the inclusion of a backscatter factor is essential for accuracy in absolute dose calculations of modulated electron fields formed with the jaws in place. Backscatter due to the MLC was shown to be negligible, no more than 0.3%. Finally, simulations of backscatter using a virtual monitor chamber and inferred forward dose components agreed with direct simulation of backscatter using Varian's VirtuaLinac system within 0.2%, further validating this approach.

Chapter 8

Conclusions and Future Work

The potential advantages of modulated electron radiation therapy, alone or in concert with photons, are only achievable with planning tools capable of performing accurate simulations of complex electron fields. This work has explored two approaches to the development of such tools for the Varian TrueBeam linear accelerator: a complete Monte Carlo accelerator model based on inferred modifications to the known internal specifications of the Varian Clinac 21EX linear accelerator, and the careful implementation of vendor provided electron phase-space source files. Each of these approaches has its own strengths and challenges, and the results are summarized here.

8.1 Complete accelerator models of the Clinac 21EX and TrueBeam

Much of this work was motivated by Varian's decision to keep the internal schematics of the TrueBeam linear accelerator proprietary. Because the internal schematics of the Clinac 21EX accelerator were explicitly known and had been implemented for use in Monte Carlo simulations of photon fields, a comparison of electron fields generated by the two machines was undertaken to assess their differences in Chapter 4.

Despite the knowledge that changes had been made in the design of the TrueBeam's electron scattering foils, among other things, the electron fields generated by the two machines were not dramatically different. With applicators in place, differences in depth dose curves fell within 2%/2 mm, while profile curves fell within 3%/3 mm everywhere except in the shoulders of the larger fields. Relative outputs as a function of field size were mostly within 3%.

When the electron fields were shaped by the MLC, depth and profile curves agreed within 2%/2 mm and 3%/3 mm, respectively, but differences in output were as great as 9.1%. Given that the Clinac 21EX and TrueBeam accelerators use the same applicators but different jaw positions to control the relative output for each applicator size, differences of this magnitude were not surprising, and presented a significant challenge in the development of complete accelerator models.

Complete accelerator models used to perform Monte Carlo simulations of Clinac 21EX photon fields were modified iteratively to best match the measured dosimetric characteristics of Clinac 21EX electron fields in Chapter 5. Measured and simulated depth and profile curves agreed within 3%/3 mm, and outputs as a function of jaw size agreed within 4%. While some systematic discrepancies remained in the slope of the profile penumbras, the performances of these models were considered adequate for proof-of-principle work, and could be useful for MERT research in facilities that still use Clinac-series accelerators. Because the BC Cancer Agency's Vancouver Island Centre has only TrueBeam accelerators, focus shifted to modifying these Clinac 21EX models for simulation of TrueBeam electrons.

Simulations performed using the 12 and 20 MeV TrueBeam electron models agreed with measured depth and profile curves within 2%/2 mm for 98% of data points and simulated output dependencies on jaw position within 3.7% of measurement. At 6 MeV, however, even after extending the gamma criteria to 3%/3 mm, only 80% of simulated data points agreed with measurement and differences in relative outputs were as great as 15%. Even if it were decided that the relative depth and profile characteristics of the 6 MeV accelerator model presented were adequate to push forward with MERT research, the inability to accurately model changes in relative output as a function of field size would necessitate the implementation of look-up tables for accurate absolute dose calculations.

At this stage in the project, Varian released electron phase-space source files for the TrueBeam and it was decided that this work would proceed by validating these phase-space source files for use in MERT applications.

8.2 Phase-space source files for the TrueBeam

The release of Varian's TrueBeam electron phase-space source files was followed, promptly, by the publication of the Rodrigues et al. [88] paper which validated the phase-spaces for use in Monte Carlo simulations of conventional electron fields shaped with applicators. In Chapter 6, the phase-space source files were further validated for use in simulating electron fields shaped with the photon MLC and delivered at short SSD.

Using the phase-space source files, Monte Carlo simulated dose distributions agreed with measured depth and profile curves within 2%/2 mm and 3%/3 mm, respectively. Simulation of relative outputs agreed with measurement within 2.7% for the most part, however, at 6 MeV, measured and simulated outputs differed by as much as 4.0% when the MLC was used to define the electron aperture. Because the MLC model used in this work was originally commissioned and optimized for photon field simulations, an avenue of future work may be the optimization of MLC model parameters for electron field simulations.

Investigations into output dependencies on jaw position for a fixed MLC field established a means by which to make informed selections of jaw position for a given MLC aperture in Section 6.2.2, a subject on which there is no clear consensus. At 6 MeV, jaws positioned 5 to 10 cm beyond the MLC-field periphery both maximize the output of the field while avoiding steep gradients. At 12 and 20 MeV, a setting between 2 and 5 cm strikes the same balance. If output stability is the most important feature of the delivery, jaw settings greater than 10 cm beyond the MLC-field periphery achieve this at all energies.

Additionally, in Section 6.2.3, the high sensitivity of simulated electron fields to jaw model was demonstrated. The default VIMC jaw model, currently used for accurate simulations of TrueBeam photon fields within the VIMC infrastructure, uses jaw positions that differ from the Monte Carlo data package specifications by 1.5 mm laterally and 6 mm vertically. This had a dramatic effect on the shape of the electron output curve as a function of jaw position for a fixed MLC-aperture at all energies, resulting in discrepancies with measured output of up to 22%.

Because Varian's phase-space source files are scored below the monitor ionization chamber, backscatter factors were simulated by determining the forward dose component in a virtual monitor chamber based on measured values of backscatter as described by Zavgorodni et al. [116]. Two techniques for measuring backscatter factors for electron fields without specialized electronics were presented in Chapter 7, and backscatter into the monitor ionization chamber was shown to be as great as 2.6% for a 1×1 cm^2 jaw-shaped field at 6 MeV. For a 1×1 cm^2 MLC-shaped field, backscatter was predicted by Monte Carlo to be on the order of 0.3%. Neither measurement technique was sensitive enough to show this effect definitively.

Using measured values of the backscatter, forward dose components in the virtual monitor chamber were computed and enabled simulation-based determination of backscatter within 0.17% of measurement. These simulations of backscatter were then used to correct simulations of output as a function of jaw setting, improving overall agreement with measurement by as much as 3%. This represents a successful extension of the work by Zavgorodni et al. [116] and further confirmation of the assertion by Popescu et al. [85] that the exact model of the monitor chamber is unimportant in determination of backscatter.

8.3 Conclusion

This work establishes a foundation for further research into the clinical utility of complex modulated electron fields generated by the TrueBeam. Implementation of the virtual monitor chamber for backscatter corrections allows for absolute dose calculations of MLC-shaped electron fields without the use of look-up tables. In a computational landscape in which Monte Carlo simulations are achievable in a clinically appropriate way, this tool may eventually aid in the reduction of low dose to normal tissue, resulting in the reduction of side effects and secondary cancers resulting from radiation therapy.

Bibliography

[1] S Agostinelli, J Allison, K Amako, J Apostolakis, H Araujo, P Arce, M Asai, D Axen, S Banerjee, G Barrand, F Behner, L Bellagamba, J Boudreau, L Broglia, A Brunengo, H Burkhardt, S Chauvie, J Chuma, R Chytracek, G Cooperman, G Cosmo, P Degtyarenko, A Dell'Acqua, G Depaola, D Dietrich, R Enami, A Feliciello, C Ferguson, H Fesefeldt, G Folger, F Foppiano, A Forti, S Garelli, S Giani, R Giannitrapani, D Gibin, J J Gómez Cadenas, I González, G Gracia Abril, G Greeniaus, W Greiner, V Grichine, A Grossheim, S Guatelli, P Gumplinger, R Hamatsu, K Hashimoto, H Hasui, A Heikkinen, A Howard, V Ivanchenko, A Johnson, F W Jones, J Kallenbach, N Kanaya, M Kawabata, Y Kawabata, M Kawaguti, S Kelner, P Kent, A Kimura, T Kodama, R Kokoulin, M Kossov, H Kurashige, E Lamanna, T Lampén, V Lara, V Lefebure, F Lei, M Liendl, W Lockman, F Longo, S Magni, M Maire, E Medernach, K Minamimoto, P Mora de Freitas, Y Morita, K Murakami, M Nagamatu, R Nartallo, P Nieminen, T Nishimura, K Ohtsubo, M Okamura, S O'Neale, Y Oohata, K Paech, J Perl, A Pfeiffer, M G Pia, F Ranjard, A Rybin, S Sadilov, E Di Salvo, G Santin, T Sasaki, N Savvas, Y Sawada, S Scherer, S Sei, V Sirotenko, D Smith, N Starkov, H Stoecker, J Sulkimo, M Takahata, S Tanaka, E Tcherniaev, E Safai Tehrani, M Tropeano, P Truscott, H Uno, L Urban, P Urban, M Verderi, A Walkden, W Wander, H Weber, J P Wellisch, T Wenaus, D C Williams, D Wright, T Yamada, H Yoshida, and D Zschiesche. Geant4—a simulation toolkit. *Nuclear Instruments and Methods in Physics Research Section A: Accelerators, Spectrometers, Detectors and Associated Equipment*, 506(3):250–303, 2003.

[2] Khalid Al-Yahya, Matthew Schwartz, George Shenouda, Frank Verhaegen, Carolyn Freeman, and Jan Seuntjens. Energy modulated electron therapy using a few leaf electron collimator in combination with IMRT and 3D-CRT: Monte

Carlo-based planning and dosimetric evaluation. *Medical Physics*, 32(9):2976, 2005.

[3] Andrew Alexander, François DeBlois, and Jan Seuntjens. Toward automatic field selection and planning using Monte Carlo-based direct aperture optimization in modulated electron radiotherapy. *Physics in Medicine and Biology*, 55(16):4563–4576, 2010.

[4] Andrew Alexander, Emilie Soisson, Tarek Hijal, Arman Sarfehnia, and Jan Seuntjens. Comparison of modulated electron radiotherapy to conventional electron boost irradiation and volumetric modulated photon arc therapy for treatment of tumour bed boost in breast cancer. *Radiotherapy and Oncology*, 100(2):253–258, 2011.

[5] E. S. M. Ali, M. R. McEwen, and D. W. O. Rogers. Detailed high-accuracy megavoltage transmission measurements: A sensitive experimental benchmark of egsnrc. *Medical Physics*, 39(10):5990, 2012.

[6] E S M Ali and D W O Rogers. Energy spectra and angular distributions of charged particles backscattered from solid targets. *Journal of Physics D: Applied Physics*, 41(5):055505, 2008.

[7] Peter R Almond, Peter J Biggs, Bert M Coursey, B M Hanson, M Saiful Huq, Ravinder Nath, and D W O Rogers. AAPM's TG-51 protocol for clinical reference dosimetry of high-energy photon and electron beams. *Medical Physics*, 26(9):1–24, 1999.

[8] John Paul Archambault and Ernesto Mainegra-Hing. Comparison between EGSnrc, Geant4, MCNP5 and Penelope for mono-energetic electron beams. *Physics in Medicine and Biology*, 60:4951–4962, 2015.

[9] Bijan Arjomandy, Ramesh Tailor, Aman Anand, Narayan Sahoo, Michael Gillin, Karl Prado, and Milos Vicic. Energy dependence and dose response of Gafchromic EBT2 film over a wide range of photon, electron, and proton beam energies. *Medical Physics*, 37(5):1942, 2010.

[10] Frank Herbert Attix. *Introduction to Radiological Physics and Radiation Dosimetry*. Wiley-VCH Verlag GmbH & Co., Weinheim, Germany, 2004.

[11] J Baro, J Sempau, and J M Fernández-Varea. PENELOPE: an algorithm for Monte Carlo simulation of the penetration and energy loss of electrons and positrons in matter. *Nuclear Instruments and and Methods in Physics Research B*, 100:31–46, 1995.

[12] M.J. Berger, J.H. Hubbell, S.M. Seltzer, J. Chang, J.S. Coursey, R. Sukumar, D.S. Zucker, and K. Olsen. XCOM: Photon Cross Section Database (version 1.5). Online.

[13] Gloria P Beyer. Commissioning measurements for photon beam data on three TrueBeam linear accelerators, and comparison with Trilogy and Clinac 2100 linear accelerators. *Journal of Applied Clinical Medical Physics*, 14(1), 2013.

[14] M Beyzadeoglu, K Oysul, B Dirican, and F Arpaci. Effect of dose-rate and lung dose in total body irradiation on interstitial pneumonitis after bone marrow transplantation. *The Tohoku Journal of Experimental Medicine*, 202(4):255–263, 2004.

[15] T Bortfeld. IMRT: a review and preview. *Physics in Medicine and Biology*, 51:R363–R379, 2006.

[16] Karl Bush, I M Gagne, Sergei F Zavgorodni, W Ansbacher, and W Beckham. Dosimetric validation of Acuros® XB with Monte Carlo methods for photon dose calculations. *Medical Physics*, 38(4):2208, 2011.

[17] Jerrold T Bushberg, J Anthony Seibert, Edwin M Leidholdt, and John M Boone. *The Essential Physics of Medical Imaging*. Lippincott Williams & Wilkins, Philadelphia, PA, 2nd edition, 2002.

[18] EuJin Chan, Jenny Lydon, and Tomas Kron. On the use of Gafchromic EBT3 films for validating a commercial electron Monte Carlo dose calculation algorithm. *Physics in Medicine and Biology*, pages 2091–2102, 2015.

[19] Zheng Chang, Qiuwen Wu, Justus Adamson, Lei Ren, James Bowsher, Hui Yan, Andrew Thomas, and Fang-Fang Yin. Commissioning and dosimetric characteristics of TrueBeam system: Composite data of three TrueBeam machines. *Medical Physics*, 39(11):6981, 2012.

[20] Indrin J Chetty, Bruce Curran, Joanna E Cygler, John J DeMarco, Gary Ezzell, Bruce A Faddegon, Iwan Kawrakow, Paul J Keall, Helen Liu, C M Charlie Ma, D W O Rogers, Jan Seuntjens, Daryoush Sheikh-Bagheri, and Jeffrey V Siebers. Report of the AAPM Task Group No. 105: Issues associated with clinical implementation of Monte Carlo-based photon and electron external beam treatment planning. *Medical Physics*, 34(12):4818, 2007.

[21] Pai-Chun M Chi, Kenneth R Hogstrom, George Starkschall, Robert A Boyd, Susan L Tucker, and John A Antolak. Application of the electron pencil beam redefinition algorithm to electron arc therapy. *Medical Physics*, 33(7):2369, 2006.

[22] T Connell, A Alexander, P Papaconstadopoulos, M Serban, S Devic, and J Seuntjens. Delivery validation of an automated modulated electron radiotherapy plan. *Medical Physics*, 41(6):061715, 2014.

[23] Magdalena Constantin, Joseph Perl, Tom LoSasso, Arthur Salop, David Whittum, Anisha Narula, Michelle Svatos, and Paul J Keall. Modeling the TrueBeam linac using a CAD to Geant4 geometry implementation: Dose and IAEA-compliant phase space calculations. *Medical Physics*, 38(7):4018, 2011.

[24] Chris Constantinou, F H Attix, and Bhudatt R Paliwal. A solid water phantom material for radiotherapy x-ray and γ-ray beam calibrations. *Medical Physics*, 9(3):436, 1982.

[25] H Davies, H A Bethe, and L C Maximon. Theory of bremsstrahlung and pair production. II. Integral cross section for pair production. *Physical Review*, 93(4):788–795, 1954.

[26] Ralf Dreindl, Dietmar Georg, and Markus Stock. Radiochromic film dosimetry: Considerations on precision and accuracy for EBT2 and EBT3 type films. *Zeitschrift fßr Medizinische Physik*, 24(2):153–163, 2014.

[27] F C P du Plessis, A Leal, S Stathakis, W Xiong, and Chang-Ming Ma. Characterization of megavoltage electron beams delivered through a photon multi-leaf collimator (pMLC). *Physics in Medicine and Biology*, 51(8):2113–2129, 2006.

[28] C Duzenli. Backscatter into the beam monitor chamber: Implications for dosimetry of asymmetric collimators. *Medical Physics*, 20(2):363, 1993.

[29] Konrad Engel and Tobias Gauer. A dose optimization method for electron radiotherapy using randomized aperture beams. *Physics in Medicine and Biology*, 54(17):5253–5270, 2009.

[30] Bruce A Faddegon, Iwan Kawrakow, Yuri Kubyshin, Joseph Perl, Josep Semapu, and Laszlo Urban. The accuracy of EGSnrc, Geant4 and PENELOPE Monte Carlo systems for the simulation of electron scatter in external beam radiotherapy. *Physics in Medicine and Biology*, 54(6151–6163), 2009.

[31] R L Ford and W R Nelson. The EGS code system: Computer programs for the Monte Carlo simulation of electromagnetic cascade showers. Technical Report SLAC-210, Department of Energy, Stanford, CA, 1978.

[32] Benedick Fraass, Karen Doppke, Margie Hunt, Gerald Kutcher, George Starkschall, Robin Stern, and Jake Van Dyk. AAPM Radiation Therapy Committee Task Group 53: quality assurance for clinical radiotherapy treatment planning. *Medical Physics*, 25(10):1773–1829, 1998.

[33] Margarida Fragoso, Sushakumari Pillai, Timothy D Solberg, and Indrin J Chetty. Experimental verification and clinical implementation of a commercial Monte Carlo electron beam dose calculation algorithm. *Medical Physics*, 35(3):1028, 2008.

[34] David K Gaffney, Dennis D Leavitt, Alexander Tsodikov, Lynn Smith, Gordon Watson, Gregory Patton, Fred A Gibbs, and Robert Stewart. Electron arc irradiation of the postmastectomy chest wall with CT treatment planning: 20-year experience. *International Journal of Radiation Oncology Biology Physics*, 51(4):994–1001, 2001.

[35] Isabelle M Gagne and Sergei F Zavgorodni. Evaluation of the analytical anisotropic algorithm (AAA) in an extreme water-lung interface phantom using Monte Carlo dose calculations. *Journal of Applied Clinical Medical Physics*, 8(33–46), 2007.

[36] Luis Isaac Ramos Garcia and José Fernando Pérez Azorin. Improving the calibration of radiochromic films by the use of uncertainties in optical density and dose. *Medical Physics*, 40(7):071726, 2013.

[37] Tobias Gauer, Konrad Engel, Antje Kiesel, Dirk Albers, and Dirk Rades. Comparison of electron IMRT to helical photon IMRT and conventional photon irradiation for treatment of breast and chest wall tumours. *Radiotherapy and Oncology*, 94(3):313–318, 2010.

[38] Yuanyuan Ge and Bruce A Faddegon. Study of intensity-modulated photon–electron radiation therapy using digital phantoms. *Physics in Medicine and Biology*, 56(20):6693–6708, 2011.

[39] Dietmar Georg, Tommy Knöös, and Brendan McClean. Current status and future perspective of flattening filter free photon beams. *Medical Physics*, 38(3):1280, 2011.

[40] John P Gibbons, John A Antolak, David S Followill, M Saiful Huq, Eric E Klein, Kwok L Lam, Jatinder R Palta, Donald M Roback, Mark Reid, and Faiz M Khan. Monitor unit calculations for external photon and electron beams: Report of the AAPM Therapy Physics Committee Task Group No. 71. *Medical Physics*, 41(3):031501, 2014.

[41] C Glide-Hurst, M Bellon, R Foster, C Altunbas, M Speiser, M Altman, D Westerly, N Wen, B Zhao, M Miften, I J Chetty, and T Solberg. Commissioning of the Varian TrueBeam linear accelerator: A multi-institutional study. *Medical Physics*, 40(3):031719, 2013.

[42] Emily Heath and Jan Seuntjens. Development and validation of a BEAMnrc component module for accurate Monte Carlo modelling of the Varian dynamic Millennium multileaf collimator. *Physics in Medicine and Biology*, 48(24):4045, 2003.

[43] D Henzen, P Manser, D Frei, W Volken, H Neuenschwander, E J Born, A Joosten, K Lössl, D M Aebersold, C Chatelain, M F M Stampanoni, and M K Fix. Beamlet based direct aperture optimization for MERT using a photon MLC. *Medical Physics*, 41(12):121711, 2014.

[44] D Henzen, P Manser, D Frei, W Volken, H Neuenschwander, E J Born, K Lössl, D M Aebersold, M F M Stampanoni, and M K Fix. Forward treatment planning for modulated electron radiotherapy (MERT) employing Monte Carlo methods. *Medical Physics*, 41(3):031712, 2014.

[45] D Henzen, P Manser, D Frei, W Volken, H Neuenschwander, E J Born, D Vetterli, C Chatelain, M F M Stampanoni, and M K Fix. Monte Carlo based beam model using a photon MLC for modulated electron radiotherapy. *Medical Physics*, 41(2):021714, 2014.

[46] Kenneth R Hogstrom and Peter R Almond. Review of electron beam therapy physics. *Physics in Medicine and Biology*, 51(13):R455–R489, 2006.

[47] Kenneth R Hogstrom, Robert A Boyd, John A Antolak, Michelle M Svatos, Bruce A Faddegon, and Julian G Rosenman. Dosimetry of a prototype retractable eMLC for fixed-beam electron therapy. *Medical Physics*, 31(3):443, 2004.

[48] Jan Hrbacek, Tom Depuydt, An Nulens, Ans Swinnen, and Frank Van den Heuvel. Quantitative evaluation of a beam-matching procedure using one-dimensional gamma analysis. *Medical Physics*, 34(7):2917, 2007.

[49] Vicky W Huang, Jan Seuntjens, Slobodan Devic, and Frank Verhaegen. Experimental determination of electron source parameters for accurate Monte Carlo calculation of large field electron therapy. *Physics in Medicine and Biology*, 50(5):779–786, February 2005.

[50] J H Hubbell. Photon Mass Attenuation and Energy Absorption Coefficients from 1 keV to 20 MeV. *International Journal of Applied Radiation and Isotopes*, 33:1269–1290, 1982.

[51] Steve B Jiang, Ajay Kapur, and Chang-Ming Ma. Electron beam modeling and commissioning for Monte Carlo treatment planning. *Medical Physics*, 27(1):180, 2000.

[52] L Jin, C Ma, M Hossain, R Price, N Nicolaou, Ahmed Abdel Rahman Eldib, J Fan, Z Chi, Q Xu, and Jinsheng S Li. Extensive Scalp Irradiation Technique using Modulated Electron Radiotherapy Delivered by Photon Multileaf Collimator. In *Proceedings of the 50th Annual ASTRO Meeting*, page S643, 2008.

[53] Harold Elford Johns and John Robert Cunningham. *The Physics of Radiology*. Thomas, Springfield, Illinois, 4th edition, 1983.

[54] Michael Joiner and Albert van der Kogel, editors. *Basic Clinical Radiobiology*. Hodder Arnold, London, 4th edition, 2009.

[55] C J Karzmark, Craig S Nunan, and Eiji Tanabe. *Medical Electron Accelerators*. McGraw-Hill, University of Michigan, 1993.

[56] I Kawrakow, DWO Rogers, F Tessier, and BRB Walters. The EGSnrc code system: Monte Carlo simulation of electron and photon transport. Technical Report PIRS-701, National Research Council of Canada, Ottawa, Canada, 2011.

[57] Iwan Kawrakow. 3D electron dose calculation using a Voxel based Monte Carlo algorithm (VMC). *Medical Physics*, 23(4):445, 1996.

[58] Iwan Kawrakow. Accurate condensed history Monte Carlo simulation of electron transport. I. EGSnrc, the new EGS4 version. *Medical Physics*, 27(3):485, 2000.

[59] Iwan Kawrakow and A F Bielajew. On the condensed history technique for electron transport. *Nuclear Instruments and Methods in Physics Research B*, 142:253–280, 1998.

[60] F M Khan, W Sewchand, and S H Levitt. Effect of air space and depth dose in electron beam therapy. *Radiology*, 126(1):249–251, 1978.

[61] Faiz M. Khan. *The Physics of Radiation Therapy*. Lippincott Williams & Wilkins, Philadelphia, PA, 3rd edition, 2003.

[62] Faiz M Khan, Karen P Doppke, Kenneth R Hogstrom, Gerald J Kutcher, Ravinder Nath, Satish C Prasad, James A Purdy, Martin Rozenfeld, and Barry L Werner. Clinical electronbeam dosimetry: Report of AAPM Radiation Therapy Committee Task Group No. 25. *Medical Physics*, 18(1):73–109, 1991.

[63] Eric E Klein, Joseph Hanley, John Bayouth, Fang-Fang Yin, William Simon, Sean Dresser, Christopher Serago, Francisco Aguirre, Lijun Ma, Bijan Arjomandy, Chihray Liu, Carlos Sandin, and Todd Holmes. Task Group 142 report: Quality assurance of medical acceleratorsa). *Medical Physics*, 36(9):4197–4212, 2009.

[64] Eric E Klein, Milos Vicic, Chang-Ming Ma, Daniel A Low, and Robert E Drzymala. Validation of calculations for electrons modulated with conventional pho-

ton multileaf collimators. *Physics in Medicine and Biology*, 53(5):1183–1208, 2008.

[65] S C Klevenhagen, G D Lambert, and Azim Arbabi. Backscattering in electron beam therapy for energies between 3 and 35 MeV. *Physics in Medicine and Biology*, 27(3):363–373, 1982.

[66] H W Koch and J W Motz. Bremsstrahlung Cross-Section Formulas and Related Data. *Reviews of Modern Physics*, 31:920–955, 1959.

[67] J S Laughlin. Development of the technology of radiation therapy. *Radiographics*, 9(6):1245–1266, 1989.

[68] J Leroux and T P Thinh. Revised tables of x-ray mass attenuation coefficients. Technical report, Corporation Scientifique Classique, 1997.

[69] Samantha A M Lloyd, Isabelle M Gagne, Magdalena Bazalova-Carter, and Sergei F Zavgorodni. Measured and Monte Carlo simulated electron backscatter to the monitor chamber for the varian TrueBeam linac. *Physics in Medicine and Biology*, 61:8779–8793, 2016.

[70] Samantha A M Lloyd, Isabelle M Gagne, Magdalena Bazalova-Carter, and Sergei F Zavgorodni. Validation of Varian TrueBeam electron phase–spaces for Monte Carlo simulation of MLC-shaped fields. *Medical Physics*, 43(6):2894–2903, 2016.

[71] Samantha A M Lloyd, Sergei Zavgorodni, and Isabelle M Gagne. Monte Carlo simulation of MLC-shaped TrueBeam electron fields benchmarked against measurement. arXiv:1406.6024.

[72] Samantha A M Lloyd, Sergei Zavgorodni, and Isabelle M Gagne. Comparison of measured Varian Clinac 21EX and TrueBeam accelerator electron field characteristics. *Journal of Applied Clinical Medical Physics*, 16(4):193–201, 2015.

[73] D A Low, W B Harms, S Mutic, and J A Purdy. A technique for the quantitative evaluation of dose distributions. *Medical Physics*, 25(5):656–61, 1998.

[74] Chang-Ming Ma, M Ding, Jinsheng S Li, Michael C Lee, T Pawlicki, and J Deng. A comparative dosimetric study on tangential photon beams, intensity-modulated radiation therapy (IMRT) and modulated electron radiotherapy

(MERT) for breast cancer treatment. *Physics in Medicine and Biology*, 48(7):909, 2003.

[75] Chang-Ming Ma, Bruce A Faddegon, D W O Rogers, and T R Mackie. Accurate characterization of Monte Carlo calculated electron beams for radiotherapy. *Medical Physics*, 24(3):401, 1997.

[76] Malcolm McEwen, Larry DeWerd, Geoffrey Ibbott, David Followill, David W O Rogers, Stephen Seltzer, and Jan Seuntjens. Addendum to the AAPM's TG-51 protocol for clinical reference dosimetry of high-energy photon beams. *Medical Physics*, 41(4):041501, 2014.

[77] J W Motz, H A Olsen, and H W Koch. Pair production by photons. *Reviews of Modern Physics*, 41:581–639, 1969.

[78] H Neuenschwander, T R Mackie, and P J Reckwerdt. MMC-a high-performance Monte Carlo code for electron beam treatment planning. *Physics in Medicine and Biology*, 40(4):543–574, 1999.

[79] A Niroomand-Rad, C.R Blackwell, B.M Coursey, K.P Gall, J.M Galvin, W.L McLaughlin, A.S Meigooni, R Nath, J.E Rodgers, and C.G Soares. Radiochromic film dosimetry: recommendations of AAPM radiation therapy committee task group 55. *Medical Physics*, 25:2093–2115, 1998.

[80] Artur Omar. *Silicon diode dose response correction in small photon fields*. PhD thesis, Stockholm University, 2010.

[81] Canadian Cancer Society's Advisory Committee on Cancer Statistics. Canadian cancer statistics 2015. Technical report, Canadian Cancer Society, Toronto, ON, 2015.

[82] Tuathan P O'Shea, Yuanyuan Ge, Mark J Foley, and Bruce A Faddegon. Characterization of an extendable multi-leaf collimator for clinical electron beams. *Physics in Medicine and Biology*, 56(23):7621–7638, 2011.

[83] Karl Otto. Volumetric modulated arc therapy: IMRT in a single gantry arc. *Medical Physics*, 35(1):310, 2008.

[84] Pavlos Papaconstadopoulos and Jan Seuntjens. A source model for modulated electron radiation therapy using dynamic jaw movements. *Medical Physics*, 40(5):051707, 2013.

[85] I Antoniu Popescu, C P Shaw, Sergei F Zavgorodni, and Wayne A Beckham. Absolute dose calculations for Monte Carlo simulations of radiotherapy beams. *Physics in Medicine and Biology*, 50(14):3375–3392, 2005.

[86] S Reinhardt, M Hillbrand, J J Wilkens, and W Assmann. Comparison of Gafchromic EBT2 and EBT3 films for clinical photon and proton beams. *Medical Physics*, 39(8):5257, 2012.

[87] John D Richert, Kenneth R Hogstrom, Robert S Fields, Kenneth L Matthews II, and Robert A Boyd. Improvement of field matching in segmented-field electron conformal therapy using a variable-SCD applicator. *Physics in Medicine and Biology*, 52:2459–2481, 2007.

[88] Anna Rodrigues, Daren L Sawkey, Fang-Fang Yin, and Qiuwen Wu. A Monte Carlo simulation framework for electron beam dose calculations using Varian phase space files for TrueBeam Linacs. *Medical Physics*, 42(5):2389–2403, 2015.

[89] Anna Rodrigues, Fang-Fang Yin, and Qiuwen Wu. Dynamic electron arc radiotherapy (DEAR): a feasibility study. *Physics in Medicine and Biology*, 59(2):327–345, 2013.

[90] M Rodriguez, J Sempau, and L Brualla. PRIMO: A graphical environment for the Monte Carlo simulation of Varian and Elekta linacs. *Strahlentherapie und Onkologie*, 189(10):881–886, 2013.

[91] Miguel Rodriguez, Josep Sempau, Antonella Fogliata, Luca Cozzi, Wolfgang Sauerwein, and Lorenzo Brualla. A geometrical model for the Monte Carlo simulation of the TrueBeam linac. *Physics in Medicine and Biology*, 60(11):N219–N229, 2015.

[92] D W O Rogers and A F Bielajew. Monte Carlo techniques of electron and photon transport for radiation dosimetry. In *The Dosimetry of Ionizing Radiation*, volume III. Academic, New York, 1990.

[93] DWO Rogers. Fifty years of Monte Carlo simulations for medical physics. *Physics in Medicine and Biology*, 51(13):R287–R301, 2006.

[94] DWO Rogers, B Walters, and Iwan Kawrakow. BEAMnrc users manual. Technical Report PIRS-0509(A)revK, National Research Council of Canada, Ottawa, 2009.

[95] Francisco Javier Salguero, Rafael Arráns, Bianey Atriana Palma, and Antonio Leal. Intensity- and energy-modulated electron radiotherapy by means of an xMLC for head and neck shallow tumors. *Physics in Medicine and Biology*, 55(5):1413–1427, 2010.

[96] Francisco Javier Salguero, Bianey Palma, Rafael Arrans, Joan Rosello, and Antonio Leal. Modulated electron radiotherapy treatment planning using a photon multileaf collimator for post-mastectomized chest walls. *Radiotherapy and Oncology*, 93(3):625–632, 2009.

[97] P Schiapparelli, D Zefiro, and G Taccini. Dosimetric verification of a commercial Monte Carlo treatment planning system (VMC++) for a 9 MeV electron beam. *Medical Physics*, 36(5):1759, 2009.

[98] J H Scofield. Theoretical photoionization cross sections from 1 to 1500 keV. Technical Report Rep UCRL-51326, Lawrence Livermore National Laboratory, 1973.

[99] Joao Seco and Frank Verhaegen, editors. *Monte Carlo Techniques in Radiation Therapy*. Imaging in medical diagnosis and therapy. CRC Press, Boca Raton, FL, 2016.

[100] Josep Sempau, Scott J Wilderman, and Alex F Bielajew. DPM, a fast, accurate Monte Carlo code optimized for photon and electron radiotherapy treatment planning dose calculations. *Physics in Medicine and Biology*, 45:2263–2291, 2000.

[101] G Starkschall, A S Shiu, S W Bujnowski, L L Wang, D A Low, and K R Hogstrom. Effect of dimensionality of heterogeneity corrections on the implementation of a three-dimensional electron pencil-beam algorithm. *Physics in Medicine and Biology*, 36(2):207–227, 1991.

[102] AAPM TG-21. A protocol for the determination of absorbed dose from high-energy photon and electron beams. *Medical Physics*, 10(6):741–771, 1983.

[103] Bruce Thomadsen, Chris Constantinou, and Anthony Ho. Evaluation of water-equivalent plastics as phantom material for electron-beam dosimetry. *Medical Physics*, 22(3):291, 1995.

[104] D.I Thwaites and J.B Tuohy. Back to the future: the history and development of the clinical linear accelerator. *Physics in Medicine and Biology*, 51:R343, 2006.

[105] R W Townson. *Enhancing the speed of radiotherapy Monte Carlo dose calculation with applications in dose verification*. PhD thesis, University of Victoria, 2015.

[106] Mustafa Çağatay Tufan, Tuba Namdar, and Hasan Gümüş. Stopping power and CSDA range calculations for incident electrons and positrons in breast and brain tissues. *Radiation and Environmental Biophysics*, 52(2):245–253, January 2013.

[107] Oleg N Vassiliev, Todd A Wareing, John McGhee, Gregory Failla, Mohammad R Salehpour, and Firas Mourtada. Validation of a new grid-based Boltzmann equation solver for dose calculation in radiotherapy with photon beams. *Phys Med Biol*, 55(3):581–98, 2010.

[108] T Vatanen, E Traneus, and T Lahtinen. Dosimetric verification of a Monte Carlo electron beam model for an add-on eMLC. *Physics in Medicine and Biology*, 53(2):391–404, 2007.

[109] Luis A Vazquez-Quino, Brian Massingill, Chengyu Shi, Alonso Gutierrez, Carlos Esquivel, Tony Eng, Nikos Papanikolaou, and Sotirios Stathakis. Monte Carlo modeling of a Novalis Tx Varian 6 MV with HD-120 multileaf collimator. *Journal of Applied Clinical Medical Physics*, 13(5):300–313, 2012.

[110] F Verhaegen, R Symonds-Tayler, H H Liu, and A E Nahum. Backscatter towards the monitor ion chamber in high-energy photon and electron beams: charge integration versus Monte Carlo simulation. *Physics in Medicine and Biology*, 45(11):3159, 2000.

[111] B Walters, Iwan Kawrakow, and DWO Rogers. DOSXYZnrc users manual. Technical Report PIRS-794revB, National Research Council of Canada, Ottawa, 2011.

[112] Rebecca Weinberg, John A Antolak, George Starkschall, Rajat J Kudchadker, R Allen White, and Kenneth R Hogstrom. Influence of source parameters on large-field electron beam profiles calculated using Monte Carlo methods. *Physics in Medicine and Biology*, 54(1):105–116, 2008.

[113] W Xiong, Jinsheng S Li, L Chen, R A Price, G Freedman, M Ding, L Qin, J Yang, and Chang-Ming Ma. Optimization of combined electron and photon beams for breast cancer. *Physics in Medicine and Biology*, 49(10):1973–1989, 2004.

[114] Zhigang Xu, Sarah E Walsh, Tejas P Telivala, Allen G Meek, and Guozhen Yang. Evaluation of the eclipse electron Monte Carlo dose calculation for small fields. *Journal of Applied Clinical Medical Physics*, 10(3):75–85, 2009.

[115] Sergei Zavgorodni, Karl Bush, C Locke, and Wayne Beckham. Vancouver Island Monte Carlo (VIMC) system for radiotherapy treatment planning dosimetry and research. *Radiotherapy and Oncology*, 84(Supplement 1):S49, 2007.

[116] Sergei F Zavgorodni, Eyad Alhakeem, and Reid Townson. Monitor backscatter factors for the Varian 21EX and TrueBeam linear accelerators: measurements and Monte Carlo modelling. *Physics in Medicine and Biology*, 59(4):911–924, 2014.

[117] Aizhen Zhang, Ning Wen, Teamour Nurushev, Jay Burmeister, and Indrin J Chetty. Comprehensive evaluation and clinical implementation of commercially available Monte Carlo dose calculation algorithm. *Journal of Applied Clinical Medical Physics*, 14(2):127–145, 2013.

[118] Timothy C Zhu, Anders Ahnesjö, Kwok Leung Lam, X Allen Li, Chang-Ming Charlie Ma, Jatinder R Palta, Michael B Sharpe, Bruce Thomadsen, and Ramesh C Tailor. Report of AAPM Therapy Physics Committee Task Group 74: In-air output ratio, Sc, for megavoltage photon beams. *Medical Physics*, 36(11):5261–5291, 2009.

[119] P Zygmanski, F Rosca, D Kadam, and F Lrenz. Determination of depth and field size dependence of MLC transmission. *Journal of Applied Clinical Medical Physics*, 8(4), 2007.